Investigation of the Electronic Structure and Photolability of Copper-, Manganese-, and Ruthenium-Nitrosyl Complexes

by

Anna C. Merkle

A dissertation submitted in partial fulfillment
of the requirements for the degree of
Doctor of Philosophy
(Chemistry)
in The University of Michigan
2012

Doctoral Committee:

Assistant Professor Nicolai Lehnert, Chair
Professor Dimitri N. Coucouvanis
Professor Stephen W. Ragsdale
Assistant Professor Anne J. McNeil

Dedication

To the Merkle/Maisel Family

Acknowledgements

I would like to thank my advisor, Professor Nicolai Lehnert for his support and guidance through the years. Working with Nicolai and his group has taught me many things pertaining to Chemistry and other subjects. I would also like to thank the members of my committee for their guidance through my PhD career. I could also not have completed this thesis without the help from a number of collaborators including, Dr. Elizabeth Papish, Dr. Pradip Mascharak, and Dr. Jeff Kampf.

I would also like to thank the people, post-docs, graduate and undergraduate students that I have had the opportunity to work with in the lab and contribute to the valuable discussions and exchanges of ideas.

Finally, an acknowledgement page would not be complete without thanking my family and friends who have been my rock throughout my PhD.

Table of Contents

List of Figures

List of Schemes

List of Tables

Chapter 1

Introduction

1.1 Nitric Oxide

There are a number of diatomic molecules that have captured researchers interest for centuries. The neutral, gaseous, diatomic molecule, nitric oxide (NO), is highly reactive due to its unpaired electron localized in the π^* molecular orbital. For example, two molecules of NO can react with dioxygen (O_2) form nitrogen dioxide (NO_2), an air pollutant. NO itself is a toxic gas and reacts with ozone to form O_2 and NO_2 and is one of the leading causes of ozone depletion within the stratosphere.[1] In addition to being harmful to the environment, the high toxicity of NO had the scientific community believing this molecule had no positive effects on biological systems. It was believed to have similar harmful effects on the respiratory system analogous carbon monoxide (CO) and cyanide (CN^-). It was not until the 1980's when the importance of NO within physiology was discovered.

1.2 NO in Biology

1.2.1 Nitrogen Cycle and Denitrificiation

One of the most important biological cycles is the nitrogen cycle where nitrogen is converted amoung its various forms. Nitrogen atoms are incorporated into the biomass through nitrogen fixation and nitrate (NO_3^-) assimilation, as seen in Figure 1.1. A separate portion of the nitrogen cycle is the stepwise reduction of NO_3^- to N_2 *via* denitrification. Bacteria use the denitrification process as a source of energy by reducing NO_3^- to N_2 through first the reduction of NO_3^- to nitrite (NO_2^-) by nitrate reductase (NAR), *NO_2^- to NO by nitrite reductase* (NIR) followed by NO reduction to nitrous oxide

(N_2O) mediated by nitric oxide reductase (NOR), and finally, N_2O is further reduced to N_2 catalyzed by nitrous oxide reductase (N2OR).

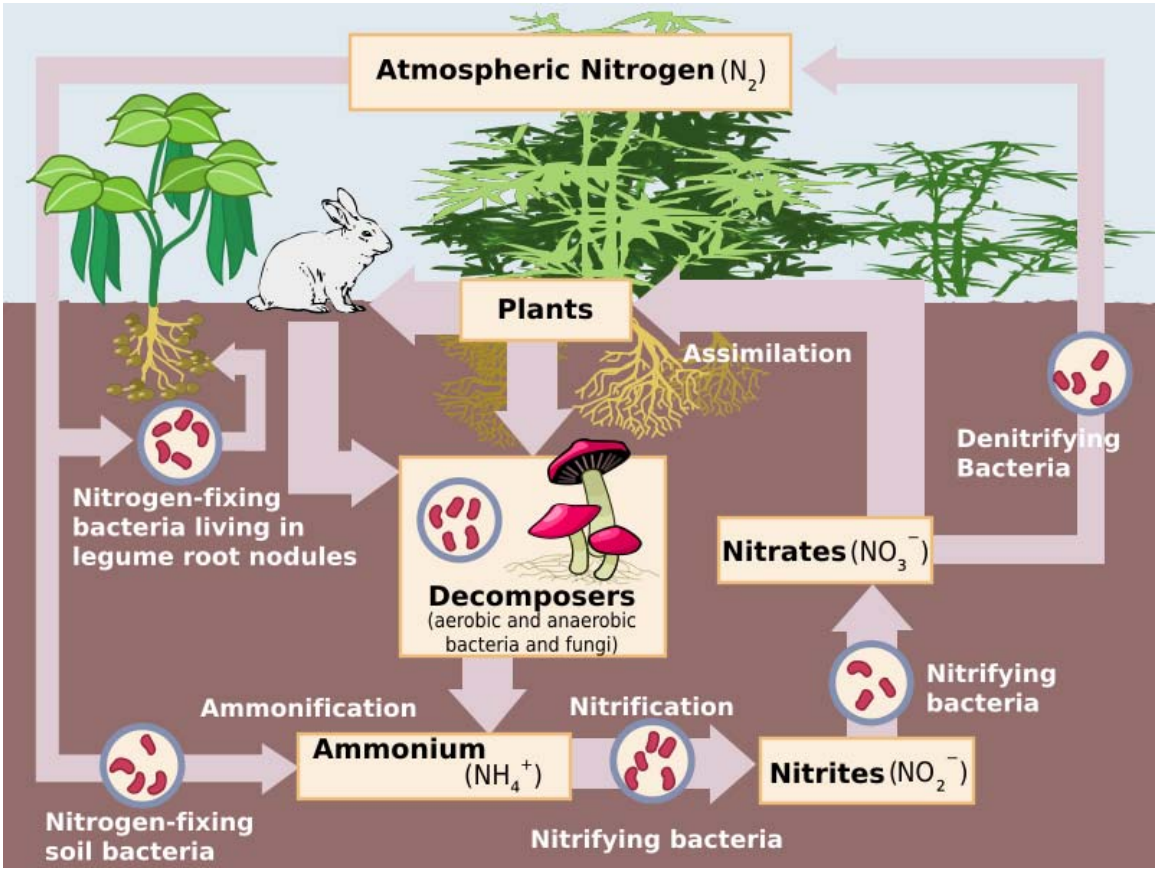

Figure 1.1 Pictorial representation of the nitrogen cycle. [2]

In particular, NIRs reduce NO_2^- to NO *via* two widely different classes of NIRs, a heme iron (cytochrome cd_1-NIR) and copper (CuNIR) NIRs. Chapter 2 of this thesis will analyze CuNIR Cu(I)-NO model complexes.

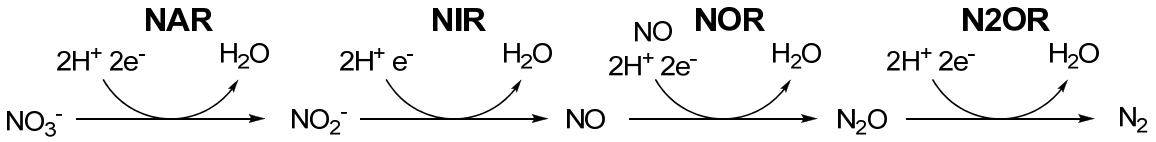

Scheme 1.1 Reaction scheme for the reduction of nitrate to dinitrogen in dissimilatory denitrification.

1.2.2 Generation of NO within Mammals

At high (μM) concentrations, NO is toxic to the body, but at smaller (nM) concentration NO is a vital molecule for many biological functions. Robert F. Furchgott, Louis J. Ignarrio and Ferid Murad were awarded the 1998 Nobel Prize in Medicine for their discovery of NO as a signaling molecule.[3-5] NO was found to be important in neurotransmission and regulation of blood pressure. The low concentrations of NO (nM) are produced by the transformation of L-arginine to citrulline by nitric oxide synthase (NOS) and are essential for biological functions.

There are three different NOS enzymes that are responsible for the formation of NO. Endothelial NOS (eNOS) produces NO for blood pressure control and is found in the endothelium cells. Neuronal NOS (nNOS) produces NO and is found in the nerve cells in the brain. Inducible NOS (iNOS) produces NO for the use in the immune response to outside pathogens. Although the body strictly regulates the production and use of the NO molecules, it is the organism's own immune system that is responsible for septic shock by the overproduction of NO. The immune system releases NO at invading bacteria, *via* iNOS. When this increase in NO does not destroy the bacteria, the immune system again increases the release of NO. As the concentration of NO increases to μM levels, the body responds negatively with a sharp decrease in the blood pressure and organ failure which often leads to death. This response is caused by the body trying to get rid of an invasive pathogen but inadvertently produces too much toxic NO which becomes poisonous.[6]

1.3 M-NO Photolabilization

As noted previously, the body is able to utilize the reactivity of NO to kill invasive pathogens by inducing apoptosis. Following this example, the release of NO in particular cells, such as cancer cells, has been a major research area in nitrosyl chemistry.[7-8] Metal-nitrosyl complexes are being designed to deliver NO molecules to targeted cancerous cells similarly to the immune systems ability to deliver NO to destroy pathogens. The most used method for site-specific release of NO from metal-nitrosyl complexes is by exposing the complex to light, which is an avenue being researched for Photodynamic Therapy (PDT).[9-14] Traditionally, PDT is a process where a non-reactive species, a

photosensitizer, is irradiated with light and activated, which then reacts with O_2 to form singlet dioxygen. This highly reactive species then react with molecules within the system to create reactive oxygen species (ROS).[10] The ROS then react with biological molecules forming a cascade of reactions eventually causing programmed cell death. Since NO is a radical, the photorelease of NO from metal-nitrosyl complexes can be included in the definition of photodynamic therapy when delivered by similar means.

Most research in the area of the photolabilization of metal-nitrosyl complexes, labeled $\{MNO\}^6$ in the Enemark-Feltham notation, [15] has focused on iron-,[11] ruthenium-[16] and manganese-[17-18] nitrosyl complexes. Previous work has shown that iron- and ruthenium-nitrosyl complexes are best described as M(II)-NO^+ complexes, where the bound NO^+ ligand forms two strong π-backbonds with the M(II)-d^6 metal center.[15-16,19-29] Correspondingly, NO adducts of specific Mn(II) complexes will be shown to have Mn(I)-NO^+ type electronic structures, as discussed in Chapter 3.[30]

Although some iron-nitrosyl $\{FeNO\}^6$ complexes (i.e. sodium nitroprusside and Roussin's salts) have been shown to release large amounts of NO when irradiated with low energy light, the lack of stability and toxicity of these complexes under physiological conditions has led to a search for suitable alternatives, in particular manganese- and ruthenium-nitrosyl $\{MNO\}^6$ complexes.[11] This will be further discussed in Chapters 3 and 4.

1.4 Scope of the Thesis

In this thesis, the electronic structure and photolability of metal-nitrosyl complexes are presented. In Chapter 2 copper-nitrosyl complexes are discussed in two parts. Part 1 is a computational analysis of Cu(I)-NO in the CuNIR active site employing two different models. First, simplified models of CuNIR with end-on and side-on bound Cu(I)-NO are utilized to understand the binding of NO to Cu(I) in the CuNIR active site. The results are further analyzed by increasing the complexity of the model with the addition of secondary sphere amino acids. The results presented here are important for understanding the two binding modes of NO to Cu(I) observed computationally and experimentally for the CuNIR active site. Part 1, Chapter 2 is based on the following papers: Adapted with permission from Fujisawa, K.; Tateda, A.; Miyashita, Y.; Okamoto, K; Paulat, F.;

Praneeth, V. K. K.; Merkle, A.; Lehnert, N. *J. Am. Chem. Soc.* **2008**, *130*, 1205-1213. Copyright 2008 American Chemical Society.[31] Adapted with permission from Merkle, A. C.; Lehnert, N. *Inorg. Chem.* **2009**, *48*, 11504-11506. Copyright 2009 American Chemical Society.[32] Merkle, A. C.; Lehnert, N. *Dalton Trans.*, **2012**, DOI: 10.1039/C1DT11049G. Reproduced by permission of The Royal Society of Chemistry.[33]

Part 2 of Chapter 2 is a spectroscopic and computational study of Cu-NO_x model complexes using hydrotris(triazolyl)borate (Ttz^-) type ligands. The initial results presented here are important for the comparison of Ttz copper complexes to the well understood hydrotris(pyrazolyl)borate (Tp^-) copper complexes in terms of the electronic structure and potential reactivity of these systems. Part 2, Chapter 2 is based on a paper that is in the process of being prepared and will be submitted in the next few months.

In Chapter 3, detailed spectroscopic and theoretical studies of two photolabile Mn(II)-nitrosyl complexes are presented. These studies provide key insight into the electronic structure in addition to insight into the mechanism of NO photolability at Vis-NIR wavelengths of light of two Mn(I)-NO^+ complexes. Chapter 3 is based on the following paper: Reprinted with permission from Merkle, A. C.; Fry, N. L.; Mascharak, P. K.; Lehnert, N. *Inorg. Chem*. **2011**, *50*, 12192-12203. Copyright 2011 American Chemical Society.[30]

In Chapter 4, the synthesis, characterization and photolabilization of water soluble and water insoluble ruthenium-nitrosyl complexes is presented. The results of this chapter are important to help understand how different solvents affect the photolabilization of Ru-NO complexes and how these results compare to other published results.

1.5 References

(1) Solomon, S.; Intergovernmental Panel on Climate Change.; Intergovernmental Panel on Climate Change. Working Group I. *Climate change 2007 : the physical science basis : contribution of Working Group I to the Fourth Assessment Report of the Intergovernmental Panel on Climate Change*; Cambridge University Press: Cambridge ; New York, 2007.

(2) EPA http://commons.wikimedia.org/wiki/File:Nitrogen_Cycle.jpg.

(3) Furchgott, R. F. *Angew. Chem., Int. Ed. Engl.* **1999**, *38*, 1870-1880.

(4) Ignarro, L. J. *Angew. Chem., Int. Ed. Engl.* **1999**, *38*, 1882-1892.

(5) Murad, F. *Angew. Chem., Int. Ed. Engl.* **1999**, *38*, 1857-1868.

(6) Ignarro, L. J. *Nitric Oxide : Biology and Pathobiology*; 1st ed.; Academic Press: San Diego, 2000.

(7) Kanwar, J. R.; Kanwar, R. K.; Burrow, H.; Baratchi, S. *Curr. Med. Chem.* **2009**, *16*, 2373-2394.
(8) Hirst, D.; Robson, T. *J. Pharm. Pharmacol.* **2007**, *59*, 3-13.
(9) Rose, M. J.; Mascharak, P. K. *Curr. Opin. Chem. Biol.* **2008**, *12*, 238-244.
(10) Chen, J.; Keltner, L.; Christopherson, J.; Zheng, F.; Krouse, M.; Singhal, A.; Wang, S. S. *Cancer J.* **2002**, *8*, 154-163.
(11) Ford, P. C.; Bourassa, J.; Miranda, K.; Lee, B.; Lorkovic, I.; Boggs, S.; Kudo, S.; Laverman, L. *Coord. Chem. Rev.* **1998**, *171*, 185-202.
(12) Mascharak, P. K.; Eroy-Reveles, A. A. *Future Med. Chem.* **2009**, *1*, 1497-1507.
(13) Hamblin, M. R.; Castano, A. P.; Mroz, P. *Nat. Rev. Cancer* **2006**, *6*, 535-545.
(14) Detty, M. R.; Gibson, S. L.; Wagner, S. J. *J. Med. Chem.* **2004**, *47*, 3897-3915.
(15) Enemark, J. H.; Feltham, R. D. *Coord. Chem. Rev.* **1974**, *13*, 339-406.
(16) Rose, M. J.; Mascharak, P. K. *Coord. Chem. Rev.* **2008**, *252*, 2093-2114.
(17) Ghosh, K.; Eroy-Reveles, A. A.; Avila, B.; Holman, T. R.; Olmstead, M. M.; Mascharak, P. K. *Inorg. Chem.* **2004**, *43*, 2988-2997.
(18) Hoffman-Luca, C. G.; Eroy-Reveles, A. A.; Alvarenga, J.; Mascharak, P. K. *Inorg. Chem.* **2009**, *48*, 9104-9111.
(19) Paulat, F.; Kuschel, T.; Nather, C.; Praneeth, V. K. K.; Sander, O.; Lehnert, N. *Inorg. Chem.* **2004**, *43*, 6979-6994.
(20) Praneeth, V. K. K.; Paulat, F.; Berto, T. C.; George, S. D.; Nather, C.; Sulok, C. D.; Lehnert, N. *J. Am. Chem. Soc.* **2008**, *130*, 15288-15303.
(21) Bottomley, F. *Coord. Chem. Rev.* **1978**, *26*, 7-32.
(22) Bottomley, F. *Acc. Chem. Res.* **1978**, *11*, 158-163.
(23) Averill, B. A. *Chem. Rev.* **1996**, *96*, 2951-2964.
(24) Linder, D. P.; Rodgers, K. R.; Banister, J.; Wyllie, G. R. A.; Ellison, M. K.; Scheidt, W. R. *J. Am. Chem. Soc.* **2004**, *126*, 14136-14148.
(25) Roncaroli, F.; Videla, M.; Slep, L. D.; Olabe, J. A. *Coord. Chem. Rev.* **2007**, *251*, 1903-1930.
(26) Goodrich, L. E.; Paulat, F.; Praneeth, V. K. K.; Lehnert, N. *Inorg. Chem.* **2010**, *49*, 6293-6316.
(27) Soldatova, A. V.; Ibrahim, M.; Olson, J. S.; Czernuszewicz, R. S.; Spiro, T. G. *J. Am. Chem. Soc.* **2010**, *132*, 4614-4625.
(28) Tfouni, E.; Krieger, M.; McGarvey, B. R.; Franco, D. W. *Coord. Chem. Rev.* **2003**, *236*, 57-69.
(29) Lehnert, N.; Berto, T. C.; Galinato, M. G. I.; Goodrich, L. E. *The Role of Heme-Nitrosyls in the Biosynthesis, Transport, Sensing, and Detoxificcation of Nitric Oxide (NO) in Biological Systems: Enzymes and Model Complexes; in "The Handbook of Porphyrin Science"*; World Scientific: Singapore, 2011; Vol. 14, Page 1-247 (Chapter 63).
(30) Merkle, A. C.; Fry, N. L.; Mascharak, P. K.; Lehnert, N. *Inorg. Chem.* **2011**, *50*, 11504-11506.
(31) Fujisawa, K.; Tateda, A.; Miyashita, Y.; Okamoto, K.; Paulat, F.; Praneeth, V. K. K.; Merkle, A.; Lehnert, N. *J. Am. Chem. Soc.* **2008**, *130*, 1205-1213.

(32) Merkle, A. C.; Lehnert, N. *Inorg. Chem.* **2009**, *48*, 11504-11506.
(33) Merkle, A. C.; Lehnert, N. *Dalton T.* **2012**, ASAP.

Chapter 2

Computational Analysis of Cu-NO_x in Copper Nitrite Reductase

2.1 Copper Nitrite Reductase Introduction

The nitrogen cycle is one of the most significant biogeochemical cycles on Earth, as nitrogen is an essential nutrient for all forms of life.[1-5] The largest contributors of nitrogen within the nitrogen cycle are gaseous dinitrogen (N_2), which cannot be utilized by plants directly, and nitrate (NO_3^-) in the form of inorganic minerals and fertilizers. The major reductive nitrogen pathways utilized by organisms are nitrogen fixation, assimilation and denitrification (*cf.* Table 2.1). Nitrogen fixation is the process where N_2 is reduced to form ammonia (NH_3) which is then integrated into biomass in the form of amino acids, nucleic acids, vitamins, hormones and many other natural products. The six-electron reduction of N_2 to NH_3 is accomplished by nitrogenase enzymes, which are usually found in free-living or symbiotic bacteria. In order for NO_3^- to be incorporated into the biomass, reduction to NH_3 by nitrogen assimilating enzymes is necessary. These enzymes facilitate the reduction of NO_3^- to NH_3 *via* an assimilatory process which involves the intermediate production of nitrite (NO_2^-) as shown in Figure 2.1. Although nitrogen assimilation is a central pathway within the biogeochemical nitrogen cycle, it is a relatively facile process involving only a few enzymes. Dissimilatory denitrification, on

Table 2.1 Archaea and bacterial genera containing denitrifying enzymes.

Achromobacter	*Hyphomicrobium*
Alcaligens	*Kingella*
Bacillus	*Neisseria*
Chromobacterium	*Paracoccus*
Corynebacterium	*Pseudomonas*
Enterobacter	*Rhizobium* (*Sinorhizobium*)
Escherichia	*Rhodopseudomonas*
Flavobacterium	*Thiobacillus*

the other hand, is a complex process which requires a large number of enzymes in order to facilitate the stepwise reduction of NO_3^- to N_2 (Scheme 1). As shown in Table 2.1, a wide range of bacteria and archaea participate in denitrification.

Dissimilatory denitrification is the anaerobic analogue of aerobic respiration, where protons are transferred from the cytoplasm to the periplasm of a cell in which ATP synthase utilizes the generated proton gradient to synthesize ATP.[6-7] However, anaerobic respiration is far less efficient as compared to aerobic respiration, requiring three electrons per transferred proton as compared to one electron per proton in aerobic respiration. Hence, aerobic respiration is energetically preferred. Overall, denitrification of NO_3^- to N_2 utilizes nitrate reductase (NAR), nitrite reductase (NIR), nitric oxide reductase (NOR), and nitrous oxide reductase (N2OR), see Scheme 2.1.

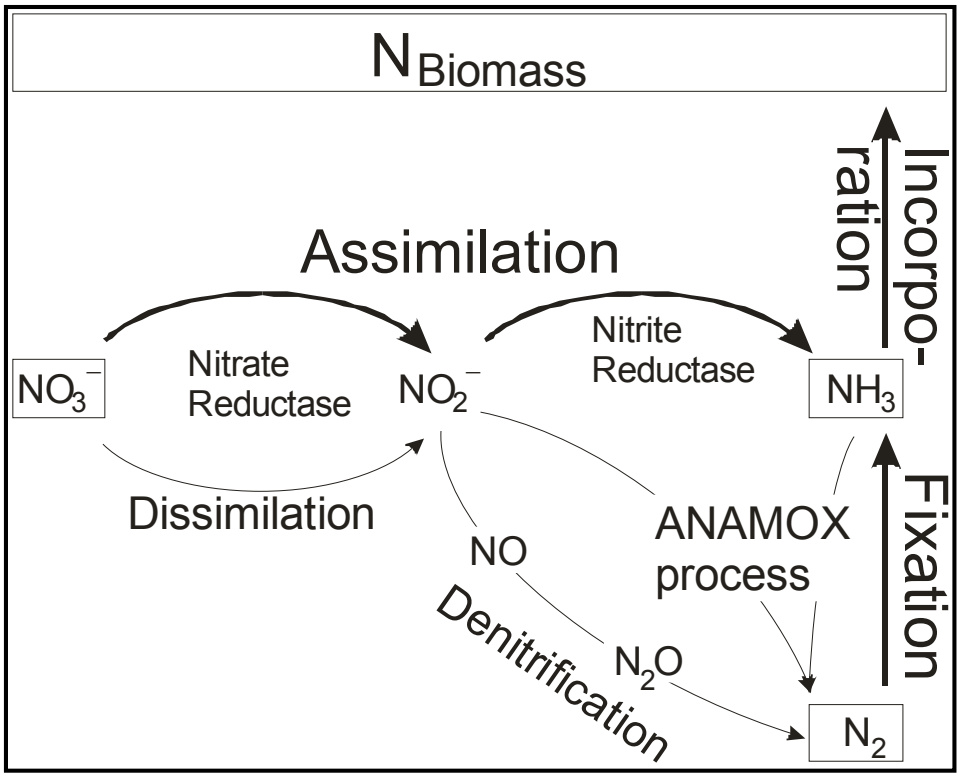

Figure 2.1 The biogeochemical nitrogen cycle, simplified by omitting oxidation steps not discussed here.

All enzymes within the denitrification cycle are equally important, however, the focus of this chapter is the one-electron reduction of NO_2^- to nitric oxide (NO) by NIRs. Two widely different classes of enzymes catalyze this reaction, a heme iron (cytochrome

cd_1-NIR) and copper (CuNIR) NIRs. Organisms that contain NIRs are found to have either one of these enzymes, but never both. Although cd_1-NIR is more abundant than CuNIR (about three-quarters of all NIRs are cd_1-NIR), CuNIR is found in a wider range of ecological niches including geothermally heated environments.[3,8] Additionally, the mechanism for the reduction of NO_2^- to NO by CuNIR is less well understood than that of cd_1-NIR, and CuNIR is thus the focus of many ongoing investigations.[9-17]

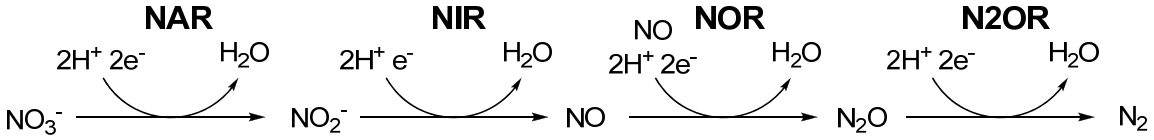

Scheme 2.1 Reaction scheme for the reduction of nitrate to dinitrogen in dissimilatory denitrification.

2.1.1 Copper Nitrite Reductase (CuNIR)

A number of CuNIR enzymes have been characterized, which has allowed for the identification of three different types of CuNIRs, known as classes I, II, and III. These classes are differentiated by (a) the number of subunits contained within the enzymes, three (I and II) or six (III), and (b) by the properties of the type 1 copper site (T1Cu). The class III hexamer was only recently crystallized.[18] Comparison with classes I and II shows that the homotrimer and hexamer are structurally similar but differ in the number of T1Cu sites, with the hexamer containing two T1Cu sites per subunit while the trimers contain only one.

2.1.1.1 Structure

The structures of the three different classes of CuNIR enzymes have been elucidated through the determination of a number of crystal structures (Table 2.2 shows a small selection). The most common class I and II enzymes show three identical subunits around a central channel forming a 3-fold axis of rotation as shown in Figure 2.2. The less common class III enzymes have very similar subunits, but in a hexameric arrangement with three 2-fold axes perpendicular to the central 3-fold axis. In classes I and II each subunit has two copper sites, a type 1 site (T1Cu, see below), which is incorporated within each subunit, and a type 2 site (T2Cu, see below), which is bound between two adjacent subunits as seen in Figure 2.2. Analyses of UV-Vis spectra and EPR hyperfine splittings in CuNIR enzymes from different organisms confirm that the two copper sites

are generally of T1Cu and T2Cu type.[3,19] Electron transfer between the T1Cu and T2Cu sites (spaced ~13Å away from each other)[6] occurs through Cys-136 and His-135, bound to T1Cu and T2Cu, respectively, as shown in the red box in Figure 2.2.[20] The T1Cu site transfers the necessary electrons from an outside electron source, often pseudoazurin, azurin or cupredoxin, to the catalytically active T2Cu as shown in Figure 2.2.[21]

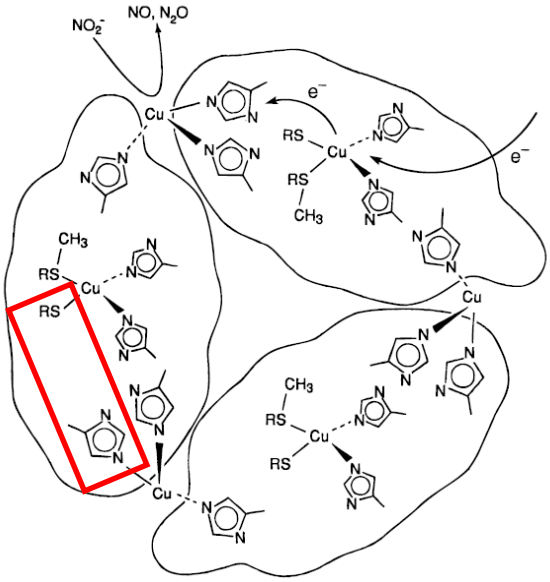

Figure 2.2 Diagram of a CuNIR homotrimer with T1Cu and T2Cu sites illustrated.[1] The red box encloses the amino acids involved in electron transfer between T1Cu and T2Cu. Reprinted with permission from ref. 1. Copyright 1996 American Chemical Society.

Table 2.2 Examples of bacteria where CuNIR crystal structures are available and selected PDB's.

	T1Cu site	PDB ID	Ref
Achromobacter cycloclastes (AcNIR)	Green	2NRD	22-23
Hyphomicrobium denitrificans (HdNIR)	Green-blue	2DV6	18
Alcaligenes xylosoxidans (AxNIR)	Blue	1OE1	24
Alcaligenes faecalis (AfNIR)	Green	2AFN	25
Rhodobacter sphaeriodes (RfNIR)	Green	1ZV2	26-27

2.1.1.2 Type 1 Copper Site (T1Cu)

Crystallographic analysis of the T1Cu site reveals a common coordination environment between all known CuNIR enzymes. All T1Cu sites are ligated to a methionine, a cysteine and two histidines in either a distorted or flattened tetrahedral geometry. Class I and II CuNIR enzymes are distinguished as either blue or green CuNIR enzymes, respectively, as derived from the colors of the oxidized enzymes. Major absorption bands

of the T1Cu centers are located at 460 nm and 580 nm for green CuNIR proteins and 590 nm for blue CuNIR enzymes (Table 2.2). These features have been assigned as S(Cys)-to-copper(II) charge transfer transitions by a combination of resonance Raman, UV-Vis, and MCD spectroscopy coupled to DFT-calculations.[28] The differences in the absorption bands are due to changes in the orbital overlap between the cysteine sulfur donor orbitals and the singly-occupied d-orbital of copper(II).[28-30] The class III CuNIR contains two different T1Cu sites per subunit, one of class I and one of class II type, and thus appears greenish-blue in the oxidized form (Table 2.2). The T1Cu site is generally responsible for the transportation of electrons from an external source, usually a pseudoazurin, azurin or cupredoxin, to the catalytic site. Initially, the T1Cu site was believed to be the active site of substrate reduction; however, further analysis of CuNIR proteins suggested that the T2Cu site was the active site, since depletion of the T2Cu caused the enzyme to be catalytically inactive.[31]

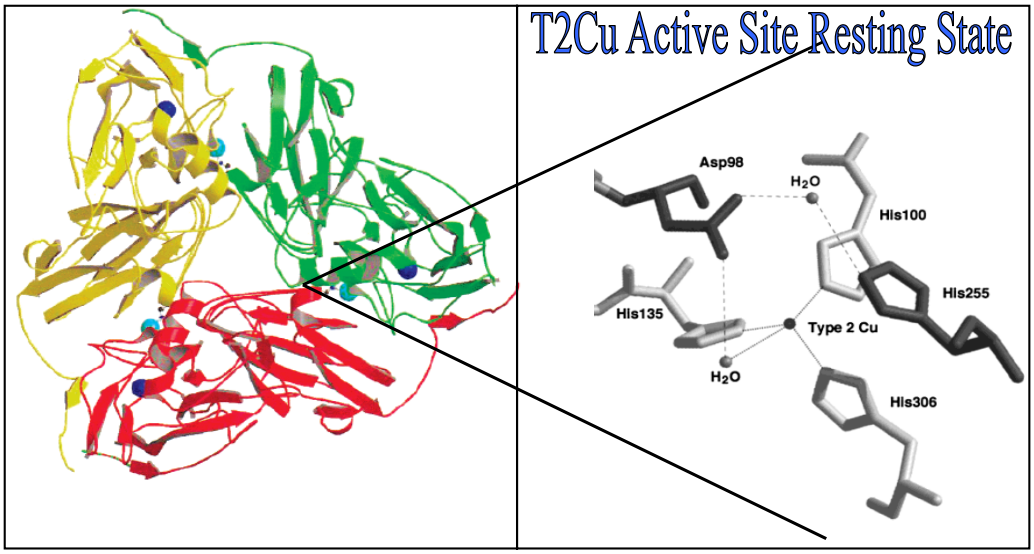

Figure 2.3 Left: ribbon diagram of *Alcaligenes xylosoxidans* GIFU 1051 CuNIR. Right: enlarged picture of the T2Cu active site of this enzyme, but using the established AfNIR/AcNIR numbering system.[4] Reprinted with permission from ref. 4. Copyright 2000 American Chemical Society.

2.1.1.3 Type 2 Copper Site (T2Cu)

In CuNIR the reduction of NO_2^- occurs at the T2Cu site.[32] Removal of the T2Cu site substantially decreases the activity of CuNIR; however, the stability of the protein is not affected.[33] The oxidized (resting) active site has a pseudotetrahedral geometry at the copper(II) with three bound histidines (His-100, His-135 and His-306 in AfNIR) and a

water molecule in the apical position, as shown in Figure 2.3.[4] A similar coordination geometry is observed in both the zinc site of carbonic anhydrase and the copper center of ascorbate oxidase.[33] In CuNIR, the T2Cu site is bound at the interface between two subunits, Figure 2.3, generating a 12 Å channel connecting the protein surface to the active site. Of the histidine ligands present at the T2Cu site, His-100 and His-135 are both bound to one subunit while His-306 is contained in the adjacent subunit. Here, the numbering scheme of the amino acids in AfNIR and AcNIR is used. Within the active site pocket a number of other amino acid residues are believed to be important for catalysis, in particular, Asp-98, His-255 (Figure 2.3) and Ile-257 (not shown in Figure 2.3). A hydrogen bonding network between Asp-98, His-255, a water molecule, and the substrate, NO_2^-, is proposed to play an important role in catalysis, while Ile-257 is proposed to help position NO_2^- within the active site.[34]

2.1.1.4 Substrate Bound Protein Crystal Structures

Crystal structures of potential reaction intermediates were obtained in order to understand the mechanism by which CuNIR reduces NO_2^- to NO. To do this, CuNIR enzymes from a range of bacteria were oxidized, reduced, and soaked with NO_2^- or NO saturated solutions to obtain the crystal structures described in the following section. The crystallographic studies on CuNIR show particularly surprising results for the Cu(I)-NO_2^- and Cu(I)-NO structures; however, since these structures were frequently obtained by soaking nitrite or NO into reduced crystals of CuNIR enzymes, there is an uncertainty whether the structures of the proteins in solution are exactly the same as those observed in these crystallographic studies (see below).

2.1.1.5 Cu(II)-NO_2^- Crystal Structures

A large number of CuNIR crystal structures with the stable Cu(II)-NO_2^- complex have been reported.[9,34-41] The large variety of orientations and positions of the bound nitrite found within these crystal structures is likely due to different stages of binding/activation of nitrite at the T2Cu(II) site. These differing structures may, for example, represent different stages of nitrite uptake into the active site. Typically, the nitrite ion is bound asymmetrically with Cu-$O1_{nitrite}$ longer than Cu-$O2_{nitrite}$ distances, where $O1_{nitrite}$ is the oxygen atom closest to Asp-98 as listed in Table 2.3 and shown in Figure 2.4. Most

Cu(II)-NO_2^- structures have long Cu-N distances; however, the crystal structure by Hasnain and coworkers (Table 2.3, AcNIR) exhibits an unusual Cu-$N_{nitrite}$ "bond" distance almost equivalent to the longer Cu-$O1_{nitrite}$ bond length, 2.15 Å and 2.19 Å, respectively. This structure of AcNIR as mentioned in Table 2.3 was obtained by soaking the crystals in a nitrite saturated solution.[34] Typically, the Cu-$O2_{nitrite}$ distance is shorter than the Cu-$O1_{nitrite}$ distance, where ranges of 1.98 to 2.2 Å (Cu-O2) and 2.19 to 2.4 Å (Cu-O1) are observed. A wide range of angles (ϕ), where ϕ is the angle between the ONO and the OCuO plane, is observed within the crystal structures, as listed in Table 2.3. In general, ϕ values range from 60^o to 84^o; however, the smallest observed angle for ϕ is 6^o. Note that when ϕ approaches 90^o, an unusual "facial" binding mode of nitrite to copper results (*cf.* Figure 2.4). This distortion is particular for CuNIR enzymes and has not been observed to any significant degree in model complexes. Most of the crystal structures show strongly varying degrees in ϕ between the different subunits of the protein.[9,35] Furthermore, within Cu(II)-NO_2^- crystal structures a hydrogen bond between the $O1_{nitrite}$ and the proton of the Asp-98 side-chain is believed to be important for catalysis. The corresponding $O1_{nitrite}$-$O\delta1_{Asp-98}$ distances reported in the crystal structures vary between 3.4 Å and 2.6 Å.[9,34-35] Finally, important amino acid residues within the active site, His-255 and Ile-257, do not change conformation upon nitrite binding and are postulated to position the nitrite within the active site.

Table 2.3 Geometric parameters for selected nitrite-bound copper(II) CuNIR crystal structures.[a]

	AfNIR[9]	AfNIR[35]	AcNIR[34]	D98N AfNIR[36]	H255N AfNIR[36]
Cu-$O2_{nitrite}$	2.04 – 2.08 Å	2.1 – 2.2 Å	1.98 Å	2.21 Å	2.16 Å
Cu-$N_{nitrite}$	2.31 – 2.36 Å	2.4 – 2.5 Å	2.15 Å	2.32 Å	3.21 Å
Cu-$O1_{nitrite}$	2.29 – 2.38 Å	2.3 – 2.4 Å	2.19 Å	2.42 Å	3.60 Å
$O1_{nitrite}$-$O\delta1_{Asp98}$	2.57 Å	3.0 Å	3.4 Å	n/a	2.79 Å
ϕ[b]	59^o – 75^o	6^o – 71^o	68^o	55^o – 84^o	2^o – 13^o
Resolution	1.4 Å	1.8 Å	1.1 Å	1.65 Å	1.90 Å
PDB ID	1SJM	1AS6	2BWI	1J9Q	1J9S

[a]The range in geometric parameters is due to three nonequivalent T2Cu sites in many of the crystal structures. [b]The angle between the two planes created by the atoms ONO and OCuO.

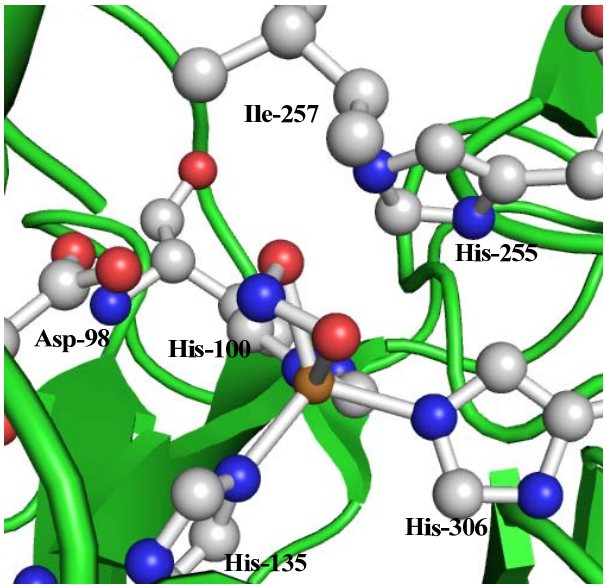

Figure 2.4 Cu(II)-NO_2^- crystal structure of AfNIR where $\phi = 69^o$. PDB: 1SJM.[9]

2.1.1.6 Cu(I)-NO_2^- Crystal Structures

One crystal structure of a Cu(I)-NO_2^- complex in a wild-type CuNIR (Figure 2.5) was determined by Adman and coworkers.[35] Here, wild-type AfNIR was reduced with ascorbate before soaking the crystals in a nitrite solution. It is believed that this structure is in fact Cu(I)-NO_2^-. Interestingly, the nitrite was again found to bind through its oxygen atoms to produce an asymmetrically oxygen-bound nitrito complex with Cu-$O1_{nitrite}$ and Cu-$O2_{nitrite}$ bond distances ranging from 2.4 Å - 2.7 Å and 2.2 Å - 2.3 Å, respectively (Table 2.4, AfNIR). This was a surprise, since in Cu(I) model complexes nitrite always binds through its N-atom (see below).

Table 2.4 Geometric parameters for selected nitrite-bound copper(I) CuNIR crystal structures.

	AfNIR[35]	D98N AfNIR[36]	H255N AfNIR[36]
Cu-$O2_{nitrite}$	2.2 – 2.3 Å	2.21 Å	2.57 Å
Cu-$N_{nitrite}$	2.5 – 2.6 Å	2.27 Å	3.70 Å
Cu-$O1_{nitrite}$	2.4 – 2.7 Å	2.89 Å	4.02 Å
$O1_{nitrite}$-$O\delta1_{Asp98}$	2.7 – 2.9 Å	n/a	2.81 Å
ϕ^a	9^o – 68^o	69^o – 98^o	3^o – 6^o
Resolution	1.85 Å	2.00 Å	1.95 Å
PDB ID	1AS8	1J9R	1J9T

[a] The angle between the two planes created by the atoms ONO and OCuO.

The reduced, nitrite bound form of CuNIR also has a larger number of water molecules within the active site, five as compared with the two in the oxidized form of the enzyme. These extra water molecules may provide a reservoir of protons within the vicinity of the catalytic site.[35,42] Two crystal structures where the amino acids Asp-98 and His-255 were mutated to asparagine (D98N) and alanine (H255N) were found to have the same asymmetric binding mode of nitrite as observed for wild-type (*cf.* Table 2.4). In addition, the H255N CuNIR structure may correspond to a Cu(II)-NO_2^- complex, since the H255N mutation removes the histidine from the electron transfer pathway between the T1Cu and the T2Cu site.[36] The H255N mutated AfNIR has very long Cu-$O2_{nitrite}$ (2.57 Å), Cu-$O1_{nitrite}$ (4.02 Å), and Cu-$N_{nitrite}$ (3.70 Å) distances, indicating that nitrite is not bound to copper in this case (*cf.* Table 2.4). The ϕ values encompass a large range of values (9^o to 98^o). Within wild-type and D98N mutated protein a facial binding mode of the nitrite to copper is observed, evident from short Cu-$N_{nitrite}$ distances and angles ϕ approaching 90^o.[36]

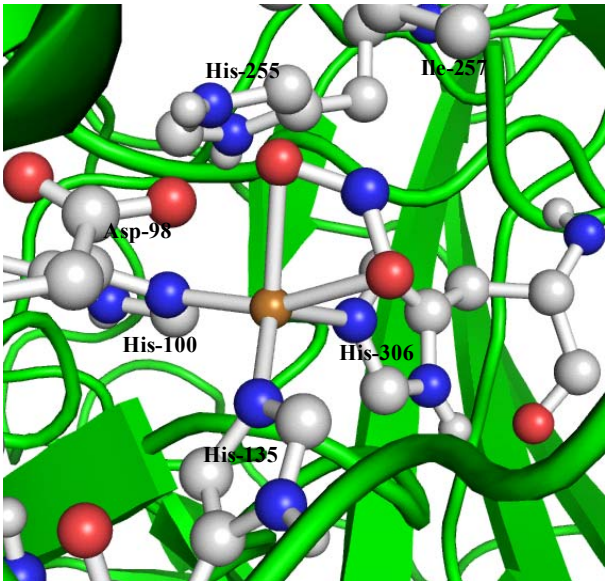

Figure 2.5 Cu(I)-NO_2^- crystal structure of AfNIR where ϕ = 68^o. PDB:1AS8.[35]

2.1.1.7 Cu(I)-NO Crystal Structures

Murphy and coworkers were the first to crystallize CuNIR (from *Alcaligenes faecalis*) with an NO bound to the T2Cu site, as shown in Figure 2.6. In this case, an unusual side-on bound Cu(I)-NO structure was observed with a Cu-N-O angle of 71^o, and almost equidistant Cu-N_{NO} and Cu-O_{NO} bond distances of 1.97 Å and 1.95 Å, respectively (*cf.*

Table 2.5). In addition to a hydrogen bond between Asp-98 and NO_2^- in Cu-NO_2^- crystal structures, the side-on bound NO in the Cu(I)-NO crystal structure is believed to also form a hydrogen bond to Asp-98, with ONO to $O\delta1_{Asp\text{-}98}$ distances ranging from 2.50 Å to 2.65 Å.[9,39]

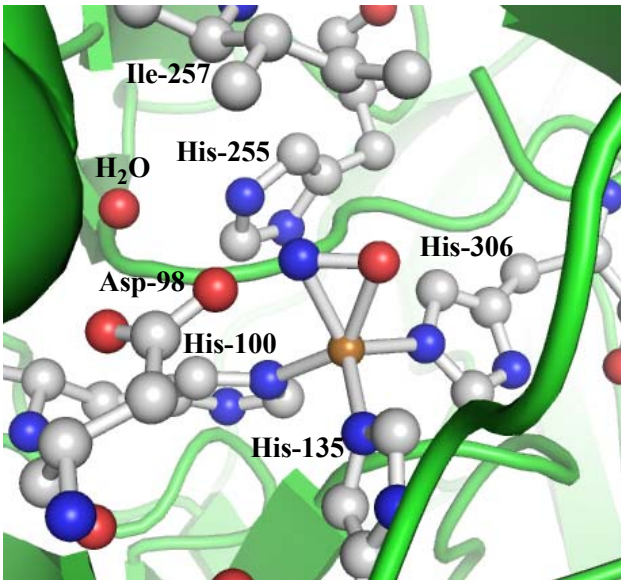

Figure 2.6. Cu(I)-NO crystal structure of AfNIR. PDB: 1SNR.[9]

Enzymes with mutations of Asp-98 to arginine (D98N) and His-145 to alanine (H145N; H145 is bound to T1Cu) show overall similar side-on bound copper nitrosyls. In D98N, the NO ligand is further away from the T2Cu by 0.15 Å (N) and 0.24 Å (O), when compared with the wild-type CuNIR crystal structure as shown in Table 2.5.[9] The increase in the Cu-N_{NO} and Cu-O_{NO} bond distances in D98N is partially due to disorder of the NO within the active site, where the different subunits within the protein show different degrees of disorder. Importantly, one of the subunits within the D98N mutant shows a particularly large disorder that is believed to correspond to two Cu-NO conformations, side-on and end-on. The mutation H145N does not change the T2Cu active site structure and therefore, the Cu(I)-NO geometry was the expected side-on bound conformation. Finally, a crystal structure by Hasnain and coworkers obtained for wild-type AcNIR with endogenously bound nitrite showed 30% of the active sites with bound NO in the side-on conformation with Cu-N and Cu-O bond distances of 2.2 Å, in overall agreement with Murphy's results.[9,34]

Table 2.5. Geometric parameters for nitric oxide bound copper(I) CuNIR crystal structures.					
	AfNIR[9]	D98N AfNIR[39]	H145N AfNIR[39]	AcNIR[34 a]	AcNIR(NO_2^-/NO)[34]
Cu-N	1.97-2.01 Å	2.16 Å	2.00 Å	2.2 Å	2.05 Å
Cu-O	1.95-2.12 Å	2.36 Å	1.95 Å	2.2 Å	1.97 Å
O_{NO}-Oδ1$_{Asp98}$	2.50-2.65 Å	n/a	2.89 Å	2.6-2.9 Å	-
<Cu-N-O	71°	79°	65°	71°	63°
Resolution	1.3 Å	1.65 Å	1.75 Å	1.12 Å	1.15 Å
PDB ID	1SNR	2PPF	2PPE	2BW5	2BWI

[a] The authors speculate that the copper center may be oxidized to copper(II) in this structure.

2.1.2 CuNIR Proposed Mechanisms

The different potential intermediates obtained from the CuNIR crystal structures along with the mechanism of *cd*$_1$-NIR and the model complex studies have allowed for a number of different mechanistic proposals for CuNIR.

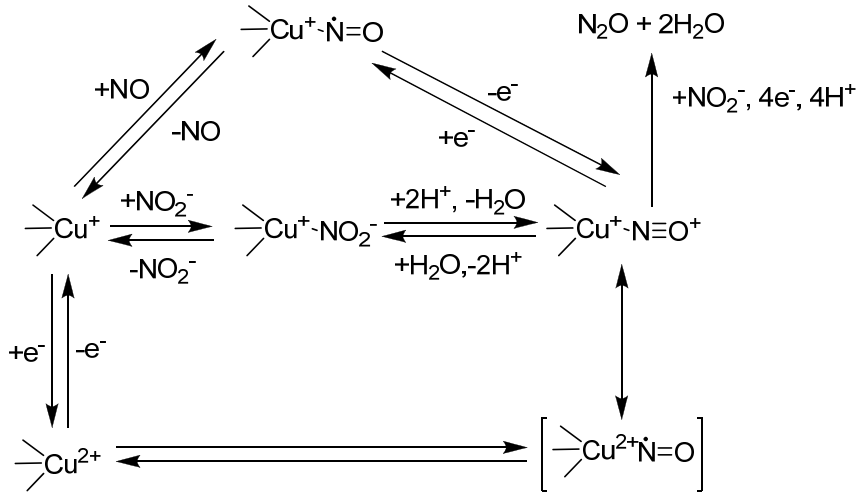

Scheme 2.2 Proposed mechanism by Averill and coworkers.[1,2]

2.1.2.1 Mechanism I

The first mechanism, proposed by Averill in 1994, is derived from the postulated mechanism of *cd*$_1$-NIR as shown in Scheme 2.2, bottom half.[43] In this mechanism, Cu(II) is first reduced to Cu(I) before NO_2^- binding occurs. Here, the structure of the proposed N-bound Cu(I)-NO_2^- intermediate was based on corresponding Cu(I) model complexes that show N-bound nitrite.[44-45] Once the substrate NO_2^- binds, two consecutive proton transfers occur from nearby protein residues to generate a Cu(I)-NO^+ complex, which is in resonance with the corresponding Cu(II)-NO(radical) form. The catalytic cycle is

completed by the loss of NO from this unstable Cu(II)-NO(radical) species. Interestingly, it was also postulated that in the presence of a large concentration of NO, the Cu(II) site can bind NO instead of NO_2^- and then react with a molecule of NO_2^- to form nitrous oxide (N_2O) *via* a potential Cu(I)-N_2O_3 intermediate that decomposes to N_2O as shown in the top half of Scheme 2.2.[10,46-47] Alternatively, Tolman suggested that NO disproportionation (*cf.* Equation **1**), as seen in Cu(I) model complexes, could be responsible for N_2O generation in CuNIR (see below).[48]

$$3NO \rightarrow NO_2 + N_2O \qquad (\mathbf{1})$$

2.1.2.2 Mechanism II

Suzuki and coworkers based their alternative mechanism on the crystal structures of the NO_2^- and NO bound forms of different CuNIR enzymes. In particular, the extended hydrogen bonding network in the active site was considered. In this mechanism, NO_2^- binds to the oxidized Cu(II) site *via* its two oxygen atoms, as shown in Scheme 2.3, **B**. Once the NO_2^- is bound, the copper site is reduced to form a Cu(I)-NO_2^- complex (Scheme 2.3, **C**). The presence of the hydrogen bonding network allows for the fast formation of an intermediate, HONO, which quickly releases NO and forms the oxidized Cu(II) with bound water, see steps **D** and **E**.[49] In this way, the N-bound Cu(I)-NO_2^- intermediate is not formed. This mechanism has been further altered by Hasnain and coworkers after the discovery of the η^2-O,O nitrite-binding mode to Cu(I) with a short Cu-$N_{nitrite}$ bond distance.[34-35] This new information is included in Scheme 2.3, **C'** and **D'**.[37] Mechanism II is further supported by DFT calculations by Blomberg and coworkers.[50]

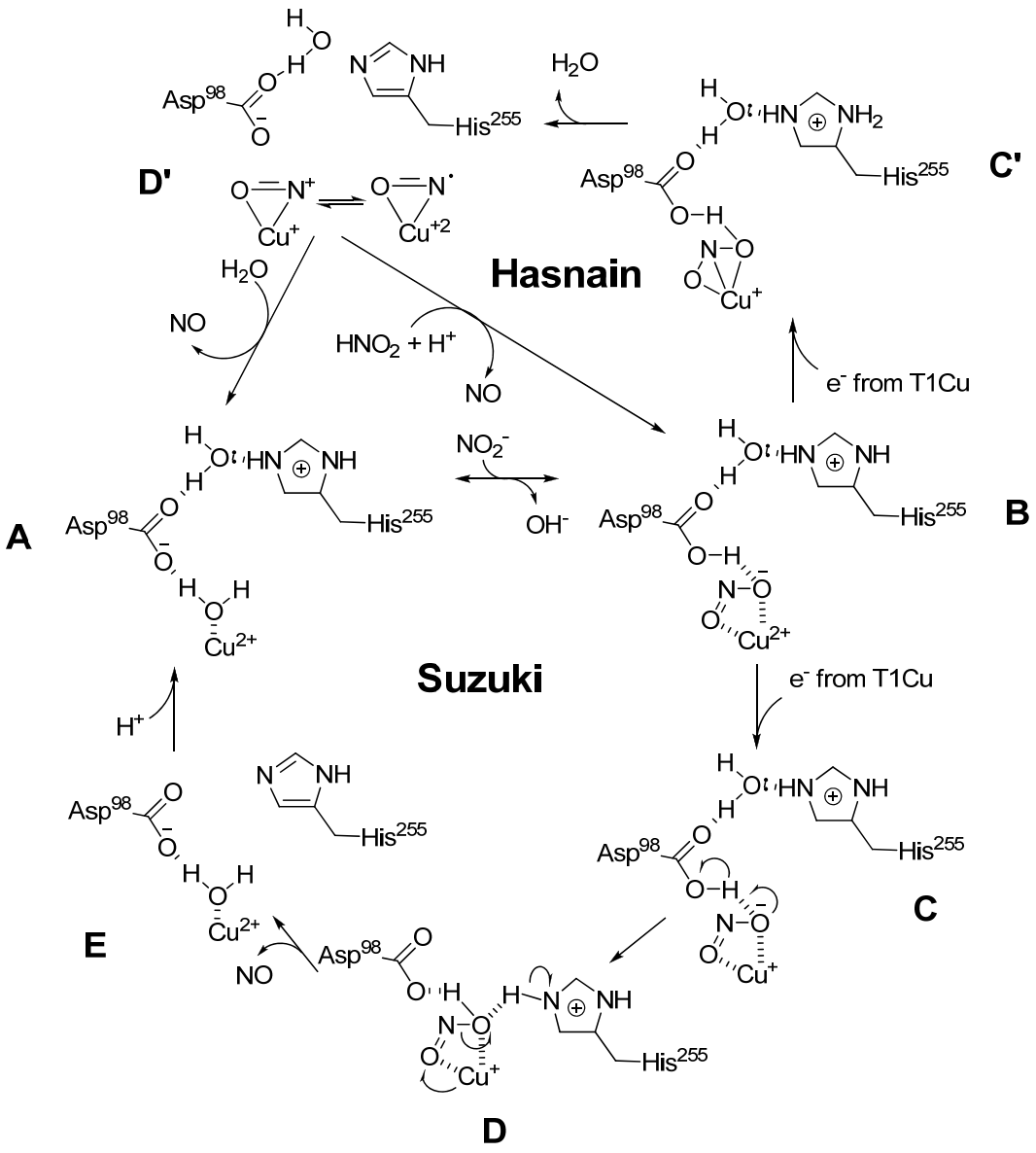

Scheme 2.3 Suzuki's proposed mechanism based on CuNIR crystal structures, **A-E**.[49] **C', D'**: addition by Hasnain.[34]

2.1.2.3 Comparison of the Proposed Mechanisms and Additional Considerations

The key difference between mechanisms I and II described above is the sequence of electron transfer and substrate (NO_2^-) binding. In mechanism I, reduction precedes NO_2^- binding, leading to the formation of the N-bound Cu(I)-NO_2^- intermediate. In contrast, in mechanism II NO_2^- binds to the oxidized Cu(II) center. This substrate binding then triggers electron transfer, forming the Cu(I)-NO_2^- intermediate in the O-bound form. The following steps are fast, such that rearrangement of NO_2^- does not occur. Interestingly, it was also observed by Murphy and coworkers and Hasnain and coworkers that, due to the

hydrogen bonding network in the CuNIR active site, NO_2^- does not show the N-bound binding mode to Cu(I) as predicted by the model complexes, which further supports Suzuki's overall reaction cycle.[9,34-35]

The mechanisms proposed by Averill and Hasnain also lead to the formation of a distinct Cu(II)-NO intermediate. The formation of such Cu(II)-NO species, better described as Cu(I)-NO^+, seems problematic, since this species is very reactive and has been shown to nitrosylate a number of organic molecules.[51] Hence, within the enzyme many amino acid side chains would be at risk of nitrosylation. In this respect, the mechanism by Suzuki and coworkers could be more reasonable, since the O-bound Cu(II)-ON species implicated in this mechanism might be more labile, and might not show this reactivity, compared to N- or side-on bound NO as in the other cases.[52] At this point it is unclear whether CuNIR forms a Cu(II)-NO adduct, and how nitrosylation chemistry is avoided in this case. New insight into this issue comes from DFT calculations as described further below. In addition, model complex studies have shed more light on the exact method of NO_2^- reduction by CuNIR.

2.1.3 Model Complexes for Catalytically Relevant Species

Model complexes of protein active sites are important to better understand the chemistry of metal centers in biology. For example, model complexes can be studied spectroscopically at very low temperatures to identify and characterize potential reaction intermediates of metalloproteins. The important intermediates within the CuNIR catalytic cycle are Cu(II)-NO_2^- , Cu(I)-NO_2^-, and Cu(II)-NO complexes, all of which have been extensively studied using model compounds.

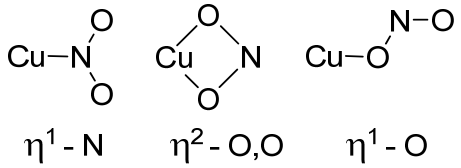

Figure 2.7 Possible binding modes of nitrite to copper.

2.1.3.1 Cu(II)-NO_2^- Model Complexes

A large number of Cu(II)-NO_2^- model complexes have been synthesized due to their relative stability and ease of preparation.[53-68] These studies have led to the identification of a number of different binding modes of NO_2^- to Cu(II), including bidentate η^2-O,O, and monodentate η^1-O and η^1-N geometries as shown in Figure 2.7. Each of the three binding modes shown in Figure 2.7 has been observed crystallographically in mononuclear Cu(II) model systems. Examples for different Cu(II)-NO_2^- geometries include: η^1-O, $[Cu(terpy)(NO_2)(OH_2)]^+$;[69] η_2-O,O, $[Cu(bpy)_2(NO_2)]^+$;[70] η^1-N, $[Cu(NO_2)_6]^{4-}$;[71] η^1-O, η^2-O,O, and η^1-N, $[Cu(NO_2)_5]^{3-}$.[72] One of the first more biomimetic Cu(II)-NO_2^- complexes synthesized and rigorously characterized was $[Cu(TEPA)(NO_2)]^+$, Figure 2.8 **A**, by Karlin and coworkers.[53] This complex shows a η^1-O binding mode in both solution and solid form with Cu-$O1_{nitrite}$ and Cu-$O2_{nitrite}$ bond distances of 2.012 Å and 2.633 Å, respectively (*cf.* Table 2.6).

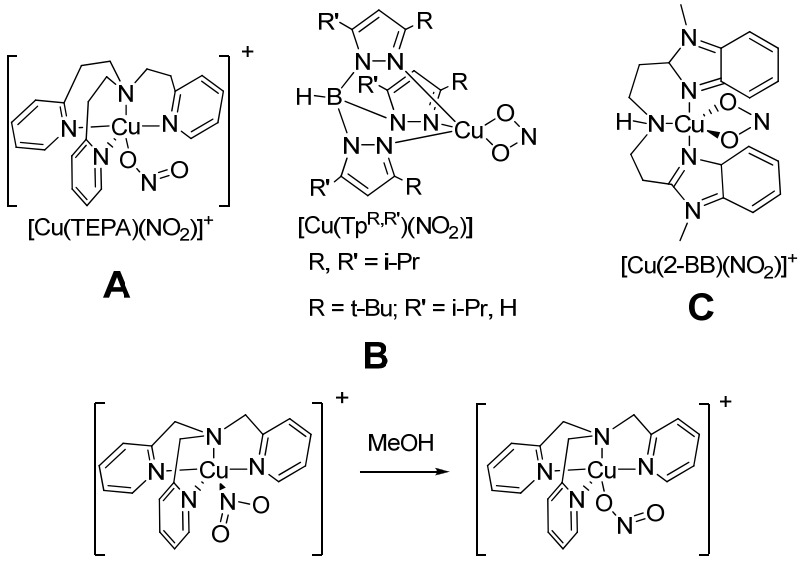

Figure 2.8 Selected Cu(II)-NO_2^- model complexes.[53-54, 57, 59-61]

In addition, many η^2-O,O Cu(II)-NO_2^- complexes were synthesized and characterized using hydrotris(pyrazolyl)borate (Tp^-, Figure 2.8 **B**) type tridentate nitrogen donor ligands[48,57,61] as well as bis[2-(1-methylbenzimidazole-2-yl)methyl]amine (2-BB, Figure 2.8 **C**) type ligands.[54-56] [Cu(Tp)(NO_2)] complexes where the Tp^- ligand carries a range of alkyl substituents in the 3, 5 positions show either symmetric or asymmetric η^2-

O,O binding modes (*cf.* Figure 2.8 **B**). Tolman first synthesized the complex [Cu($Tp^{t\text{-}Bu,H}$)(NO_2)] with asymmetric η^2-O,O binding of the NO_2^- ligand.[57] Here, one of the determining factors for the exact binding mode is the bulk of the Tp^- substitutents. For example, the sterically bulky [Cu($Tp^{t\text{-}Bu,i\text{-}Pr}$)($NO_2$)] complex has an asymmetric η^2-O,O binding mode with Cu-$O_{nitrite}$ bond distances of 1.987 Å and 2.195 Å as compared to the less sterically bulky [Cu($Tp^{i\text{-}Pr,i\text{-}Pr}$)($NO_2$)] complex, which shows a symmetric η^2-O,O nitrite coordination with Cu-$O_{nitrite}$ bond distances of 2.022 Å and 2.031 Å (*cf.* Table 2.7).

Table 2.6 Experimental geometric parameters and vibrational frequencies of selected Cu(II)-NO_2^- model complexes.

Parameters	$[Cu(TEPA)(NO_2)]^+$	$[Cu(TPA)(NO_2)]^+$			Parameters	$[Cu(2\text{-}BB)(NO_2)]^+$
		η^1-N	η^1-O			
Cu-O1$_{nitrite}$	2.012 Å	-	1.938 Å		Cu-O1$_{nitrite}$	2.008 Å
Cu-O2$_{nitrite}$	2.633 Å	-	-		Cu-O2$_{nitrite}$	2.439 Å
Cu-N$_{nitrite}$	2.746 Å	1.932 Å	-		Cu-N$_{nitrite}$	-
Cu-N$_{am}$	2.083 Å	2.023 Å	2.031 Å		Cu-N$_{am}$	2.017 Å
Cu-N$_{py}$	2.039 Å	2.095 Å	2.026 Å		Cu-N$_{im}$	1.965 Å
Cu-N$_{py}$	2.049 Å	2.047 Å	2.047 Å		Cu-N$_{im}$	1.964 Å
Cu-N$_{py}$[a]	2.253 Å	2.073 Å	2.129 Å			
<(O-N-O)	114.9°	101°	114.8°		<(O-N-O)	113.5°
ν(N=O)	1379 cm^{-1}	1390[b] cm^{-1}	1426 cm^{-1}		ν_{as}(N-O)	1334 cm^{-1}
ν(N-O)	1134 cm^{-1}	1330[c] cm^{-1}	1082 cm^{-1}		ν_s(N-O)	1265 cm^{-1}
Ref	[53]	[60]			Ref	[54]

[a] Pyridine trans to open coordination site. [b] Antisymmetric NO stretch [c] Symmetric NO stretch.

Interestingly, the symmetric and asymmetric coordination of nitrite changes the ground state of the complexes as observed by EPR spectroscopy.[48,61] The bulky [Cu($Tp^{t\text{-}Bu,i\text{-}Pr}$)($NO_2$)] complex has a d_{z2} ground state while the less bulky [Cu($Tp^{i\text{-}Pr,i\text{-}Pr}$)($NO_2$)] complex has a $d_{x2\text{-}y2}$ ground state, based on both experimental EPR data along with computational analysis.[61] The difference in ground state has a limited effect on the electronic spectra, which is evident from the similar appearances of both the UV-Vis absorption and MCD spectra of these complexes.[61] In addition, the symmetric and asymmetric binding geometries of η^2-O,O Cu(II)-NO_2^- complexes have only a small effect on the vibrational data as shown in Table 2.7.[61] In comparison, the analogous neutral tris(pyrazolyl)methane (Tpm) ligands lead to the formation of bis-nitrite

complexes. Interestingly, [Cu(Tpm$^{i\text{-Pr},i\text{-Pr}}$)(ONO)($NO_2$)] shows both an η^1-O nitrite ligand along with an η^1-N bound nitrite in the same compound.[61]

Table 2.7 Geometric parameters and vibrational frequencies of experimental and computational [Cu(Tp)(NO_2)] complexes.

Parameters	Experimental Data [Cu(Tp^{x,y})(NO_2)]			Computational Data [Cu(Tp^{H,H})(NO_2)]		
	x = *t*-Bu y = H	x = *i*-Pr y = *i*-Pr	x = *t*-Bu y = *i*-Pr	η^2-O,O	η^1-N	η^1-O
Cu-O1$_{nitrite}$ [Å]	1.976	2.022	1.987	2.050	2.486	2.057
Cu-O2$_{nitrite}$ [Å]	2.169	2.031	2.195	2.063	2.908	2.051
Cu-N$_{nitrite}$ [Å]	-	2.477	2.493	2.503	1.925	2.501
Cu-N$_{pz}$[a] [Å]	2.100	1.996/2.110	2.063/2.091	2.035	2.021	1.999
Cu-N$_{pz}$[b] [Å]	1.954	1.966	1.965	2.178	2.108	2.177
<(O-N-O)	110.1°	113.7°	109.0°	110.0°	125.7°	109.9°
ν_s(N-O) [cm^{-1}]	1167	1287	1264	1248	1231	1249
ν_{as}(N-O) [cm^{-1}]	1307	1197	1182	1098	1461	1097
δ(O-N-O) [cm^{-1}]	-	877	875	833	772	833
ν_s(Cu-O) [cm^{-1}]	-	358	-	360/316	381/296[c]	360/316
ν_{as}(Cu-O) [cm^{-1}]	-	-	-	313	-	312
Ref	57	61	61	61	61	61

[a] Equitorial pyrazole nitrogens. [b] Axial pyrazole nitrogen. [c] Here: ν(Cu-N).

Another interesting Cu(II)-NO_2^- model complex is [Cu(TPA)(NO_2)]$^+$ as shown in Figure 2.8 **D**. The initial crystal structure of this complex shows the η^1-N binding mode which is rare for Cu(II)-NO_2^-. However, this complex was found to readily interconvert from the η^1-N to the η^1-O form during recrystallization in methanol.[59-60] This facile interconversion between the two different binding modes infers that the energy difference between the η^1-N and the η^1-O binding mode is very small. DFT calculations were utilized to probe the energy differences between each of the different binding modes of Cu(II)-NO_2^-. The simplified [Cu(Tp^{H,H})(NO_2)] complex was used for these investigations (*cf.* Figure 2.8 **B** where R and R' are hydrogen). It was found that the η^2-O,O complex has the lowest total energy while the η^1- O and η^1- N binding modes were calculated to be only +0.1 kcal/mol and +5.5 kcal/mol higher in energy, respectively (Table 2.7).[61]

The electronic structure of the Cu(II)-NO_2^- adduct of CuNIR was analyzed by Solomon and coworkers. As shown in Figure 2.9, left, the main contribution to the Cu(II)-nitrite bond (besides electrostatics) stems from the σ donation of the nitrite in-

plane π orbital into the d_{x2-y2} orbital of copper. Figure 2.9, left shows the corresponding antibonding combination (the β-LUMO), which has 65% d_{x2-y2} character.[15] This MO is of key significance for electron transfer, as it serves as the acceptor orbital that receives an electron from the reduced T1Cu center during catalysis. Interestingly, this bonding description is similar to Cu(II)-NO_2^- adducts in hydrotris(pyrazolyl)borate complexes where nitrite is symmetrically bound. As shown in Figure 2.9, right, the d_{x2-y2} β-LUMO of the model complex [Cu($Tp^{H,H}$)(NO_2)] is very similar to the corresponding orbital in the protein.[61]

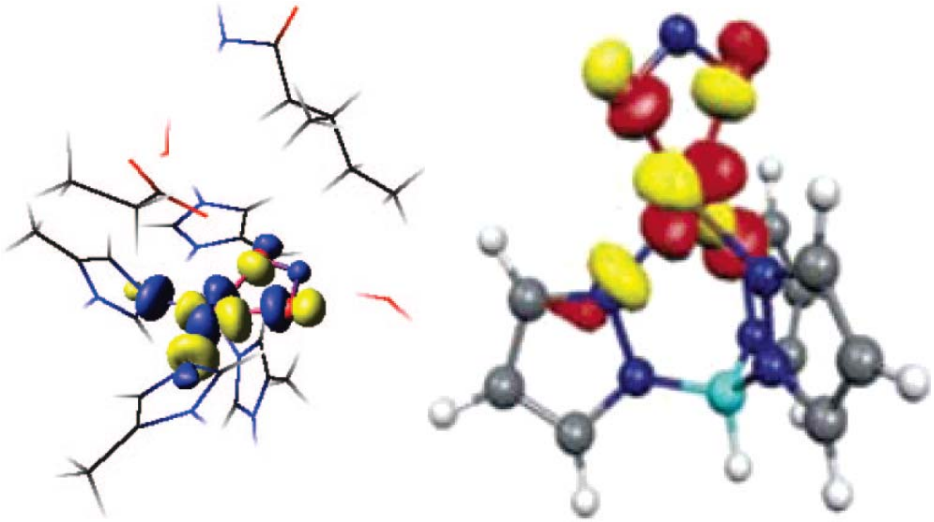

Figure 2.9 Contour plots of the β–LUMOs of the Cu(II)-NO_2^- adduct of CuNIR (left) and of the η^2-O,O model complex [Cu($Tp^{H,H}$)(NO_2)] (right).[15,61] Reprinted with permission from ref. 15. Copyright 2009 American Chemical Society. Reprinted with permission from ref. 61. Copyright 2007 American Chemical Society.

2.1.3.2 Cu(I)-NO_2^- Model Complexes

A number of Cu(I)-NO_2^- model complexes have been synthesized and characterized in the literature due to their catalytic activity in nitrite reduction.[11-12,44,52,54-56,73-74] These complexes generally show η^1-N bound nitrite with typical Cu-N distances of 1.9 Å.[44-45] The first structurally characterized η^1-N Cu(I)-NO_2^- complex was reported by Tolman and coworker, [Cu(*i*-Pr_3TACN)(NO_2)] (Figure 2.10 **A**).[45,52] When reacted with acetic acid, this complex produces one equivalent of NO as shown in Scheme 2.4.[44-45,52,73] This observation is in agreement with Averill's proposed mechanism for CuNIR (mechanism I), which includes an η^1-N Cu(I)-NO_2^- intermediate. Casella and coworkers further

synthesized a number of Cu(I)-NO_2^- complexes that were also active in nitrite reduction; however, the structures of these complexes were not reported (*cf.* Figure 2.10 **B** & **C**).[54-56] Additional Cu(I)-NO_2^- complexes that are capable of the reduction of nitrite have also been reported.[12,74]

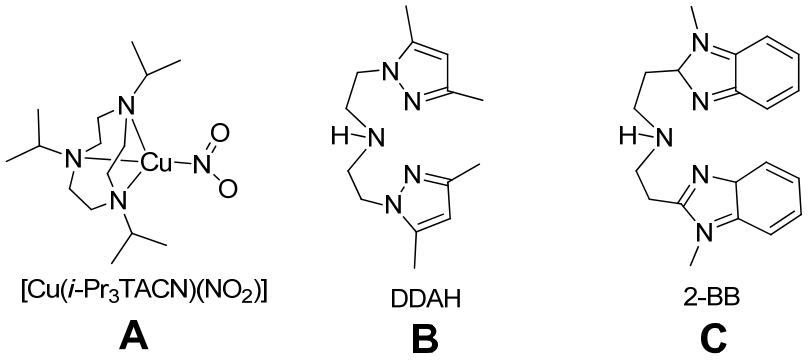

Figure 2.10 The structure of a Cu(I)-NO_2^- complex with *i*-Pr_3TACN as coligand (**A**).[44] Two ligands used by Casella and coworkers for the preparation of Cu(I)-nitrite complexes (**B**, **C**).[52, 56]

The mechanism by which NO_2^- is reduced to NO by Cu(I) model complexes has been studied by a number of research groups.[12,44-45,73] Casella and coworkers found that mechanistically the reaction is first order in Cu(I) and H^+ while NO_2^- shows saturation kinetics.[56] It was also found that the protonation of the bound nitrite has to be faster than the electron transfer from the Cu(I) center.[54] Model complexes are ideal to study this reaction, since the Cu(I)-NO_2^- complexes are stable in the absence of a proton source. In contrast, the reaction is more difficult to investigate in CuNIR since the Cu(I)-NO_2^- species is not stable in this case.

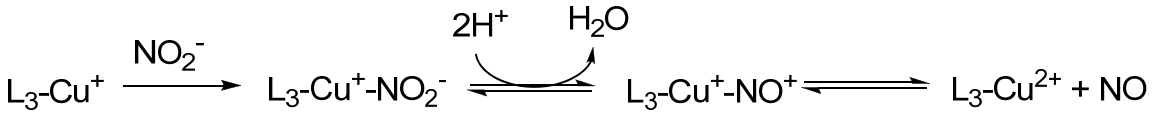

Scheme 2.4 Proposed reaction scheme for the addition of acid to Cu(I)-NO_2^- complexes.[71]

2.1.3.3 Cu(II)-NO Model Complexes

As with the binding mode of NO_2^- to copper there are a number of different binding modes that NO can adopt when binding to a metal center. For example, NO can bind end-on, either linearly or bent, or side-on to copper as shown in Figure 2.11. Very few Cu(II)-

NO complexes have been synthesized and spectroscopically characterized due to their high reactivity and instability.

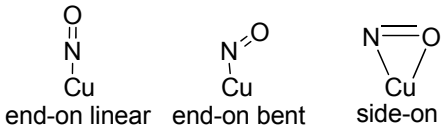

Figure 2.11 Possible binding modes of nitric oxide to copper.

The first study of Cu(II)-NO complexes occurred in the early 1900's. Here, $CuCl_2$ was reacted with NO in solution and a color change was observed indicating the formation of a Cu(II)-NO complex.[75-76] It was not until the 1960's that the formation of the Cu(II)-NO adduct was confirmed *via* UV-Vis absorption spectroscopy and by observation of nitrosylated alcohols in the reaction mixtures. However, the Cu(II)-NO complexes were never structurally characterized.[75-78] Ford and coworkers prepared the complex $[Cu(dmp)_2(H_2O)_2]^{2+}$ (dmp = 2,9-dimethyl-1,10-phenanthroline; Figure 2.12 **A**) that when reacted with excess NO in methanol underwent an intermolecular reductive nitrosylation, forming nitrosylated methanol (methyl nitrite) and a Cu(I)-$(dmp)_2$ complex, Equation **2**.[79]

$$\text{Cu(II)-NO} \leftrightarrow \text{Cu(I)-NO}^+ + \text{R-OH} \rightarrow \text{Cu(I)} + \text{RONO} + \text{H}^+ \qquad (\mathbf{2})$$

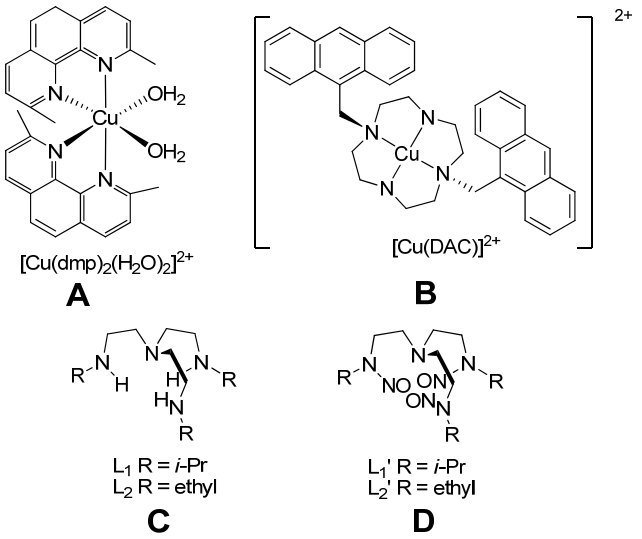

Figure 2.12 The structures of Cu(II) complexes with dmp[79] (**A**), and an anthracene substituted cyclam derivative[78] (**B**), and drawings of ligands L_1 (tris(2-isopropylaminoethyl)amine) and L_2 (tris(2-ethylaminoethyl)amine) (**C**), and their trinitrosylated versions L_1' and L_2' (**D**).[13]

In addition to this intermolecular reaction, an intramolecular nitrosylation was observed when a Cu(II)-DAC complex (DAC = anthracene substituted cyclam; Figure 2.12 **B**) was reacted with base and excess NO gas to form the nitrosylated cyclam ligand, which subsequently dissociated from the copper center.[80]

Recently, Mondal and coworkers synthesized two Cu(II) complexes with the tripodal ligands tris(2-isopropylaminoethyl)amine (L_1) and tris(2-ethylaminoethyl)amine (L_2), see Figure 2.12 **C**, that, when reacted with NO gas, formed unstable Cu(II)-NO intermediates that were characterized by UV-Vis absorption spectroscopy. These Cu(II)-NO species quickly decomposed forming a reduced Cu(I) complex and the corresponding trinitrosylated ligands. Both the Cu(I) species, in the form of the tetrakis(acetonitrile) complex, and the nitrosylated ligands were structurally characterized (*cf.* Figure 2.12 **D**).[13,81]

Finally, two Cu(II)-NO complexes with 2-aminomethylpyridine and bis-(2-aminoethyl)amine as coligands were synthesized and spectroscopically characterized using UV-Vis, IR and EPR spectroscopy.[82] In these cases, NO^+ transfer from copper leads to the formation of a diazonium intermediate, followed by transformation of a primary amine group of the coligand into a secondary amine as shown in Scheme 2.5.

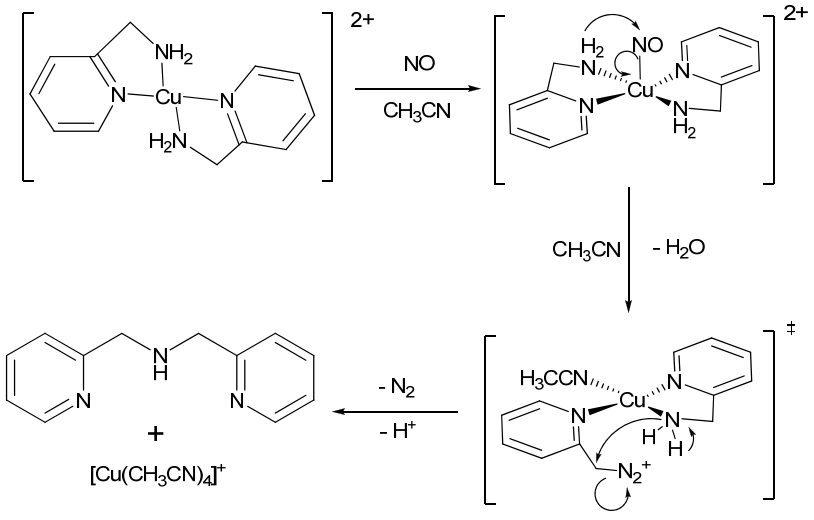

Scheme 2.5 Proposed mechanism for the diazotation of the primary amine group of aminomethylpyridine ligands by a Cu(II)-NO species.[82]

In summary, secondary amines are generally nitrosylated by Cu(II)-NO species similarly to what is observed with ligands L_1 and L_2 (*cf.* Figure 2.12 **D**). This parallels the synthesis of nitrosamines from secondary amines using nitrite salts and acid in organic synthesis. Primary amines, on the other hand, form diazonium ions by reaction with Cu(II)-NO complexes,[82] which is similar to the reaction of primary amines with nitrite salts and acid. Cu(II)-NO complexes therefore seem to be versatile NO^+ transfer catalysts that could potentially be used in organic synthesis.

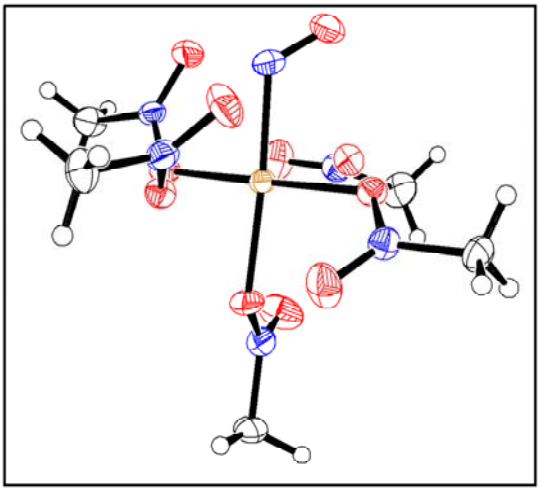

Figure 2.13 Crystal structure of $[Cu(CH_3NO_2)_5(NO)][PF_6]_2 \bullet CH_3NO_2$ showing 40% thermal ellipsoids. PF_6^- and solvent CH_3NO_2 are omitted for clarity.[14]

The only structurally characterized Cu(II)-NO complex to date was prepared by Hayton and coworkers. This complex was synthesized by reacting metallic copper with NO^+ in nitromethane to form the Cu(II)-NO complex shown in Figure 2.13.[14] The crystal structure of this complex shows that the Cu(II)-N-O unit contains bent, end-on bound NO [Cu-N-O angle: 121°] with an unusually long Cu-N_{NO} bond distance of 1.955 Å, as compared to Cu-NO bond lengths of 1.76 - 1.79 Å as observed for Cu(I)-NO model systems (*cf.* Table 2.8). The Cu-O_{NO} distance is 2.70 Å in this complex, indicating that NO is not side-on bound. In addition, Hayton's Cu(II)-NO complex shows the N-O stretching vibration at 1933 cm^{-1},[14] whereas this mode is usually observed around 1700 cm^{-1} in Cu(I)-NO model systems. This indicates that $[Cu(CH_3NO_2)_5(NO)]^{2+}$ has a Cu(I)-NO^+ type electronic structure.

Interestingly, the distinguished chemistry of Cu(II) and NO was used by Lippard and coworkers to construct chemical NO probes.[83-86] This was achieved by complexing the non-fluorescent dye FL1 with Cu(II) to form a Cu(II)-FL1 adduct (Figure 2.14). Fluorescence is not observed when NO is not present. However, upon addition of NO, fluorescence turns on due to the intermediate formation of a Cu(I)-NO^+ complex that decomposes to reduced Cu(I) and the fluorescent nitrosamine, FL1-NO (*cf.* Figure 2.14).[86-87]

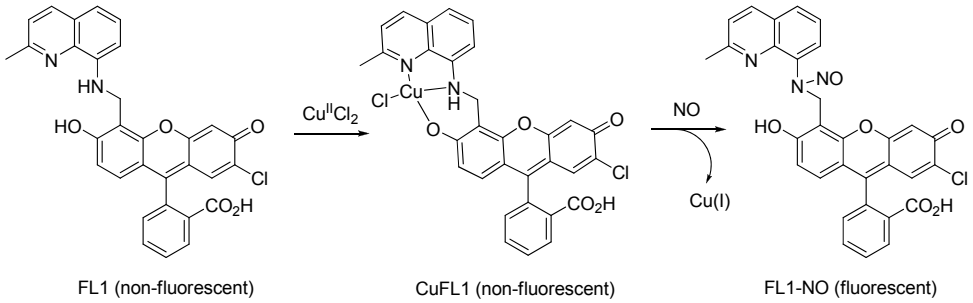

Figure 2.14 The non-fluorescent ligand FL1 produces the fluorescent, nitrosylated dye FL1-NO when reacted with Cu(II) and NO. FL1 can therefore be used for detection of NO in cells.[86-87]

2.1.4 The Mechanism of Nitrite Reduction by Copper(I): The Central Mechanistic Step of CuNIR Catalysis

Solomon and coworkers used experimental and computation results to analyze the sequence of proton and electron transfer to the nitrite bound T2Cu center of CuNIR, ultimately leading to the formation of NO.[15] Experimentally, the T1Cu and T2Cu sites of CuNIR were studied as a function of pH using EPR and MCD spectroscopy. At high pH the T1Cu center can be selectively reduced to yield the T1Cu(I)/T2Cu(II)-NO_2^- form of the enzyme. If the pH is lowered, protonation of the active site Asp-98 side chain greatly shifts the redox potential of the T2Cu(II)-NO_2^- center towards positive potentials, and triggers electron transfer to generate the catalytically active T2Cu(I)-NO_2^- intermediate. Here, bidentate coordination of nitrite to copper(I) allows for effective backdonation into the σ^* orbital of nitrite, which mediates N-O bond cleavage. The exact details of proton and electron transfer to the copper(I)-bound nitrite for NO formation were further investigated using DFT calculations.

Figure 2.15 shows a two-dimensional potential energy surface plot for the reduction and protonation of nitrite in the Cu(I)-NO_2^- intermediate of CuNIR to form

Cu(II) and NO.[15] The results show that electron transfer from Cu(I) to nitrite is energetically very unfavorable (>50 kcal/mol) in this complex. Hence, mechanistically the protonation of the NO_2^- ligand occurs first, which shifts the redox potential and, in this way, enables the electron transfer from T2Cu to the protonated nitrite (HNO_2) ligand (as mentioned above with the pH drop experiment). This induces the breaking of the ON-OH bond. In this way, protonation triggers the reduction of NO_2^- to generate NO and a Cu(II)-OH^- complex, which requires a total of less than 16 kcal/mol as shown in Figure 2.15.[15] Furthermore, the postulated formation of a Cu(II)-OH complex is intriguing, as this avoids the formation of a reactive (strongly nitrosylating) Cu(II)-NO species. This constitutes a modification of the original mechanisms of CuNIR as shown in Schemes 2.2 and 2.3.

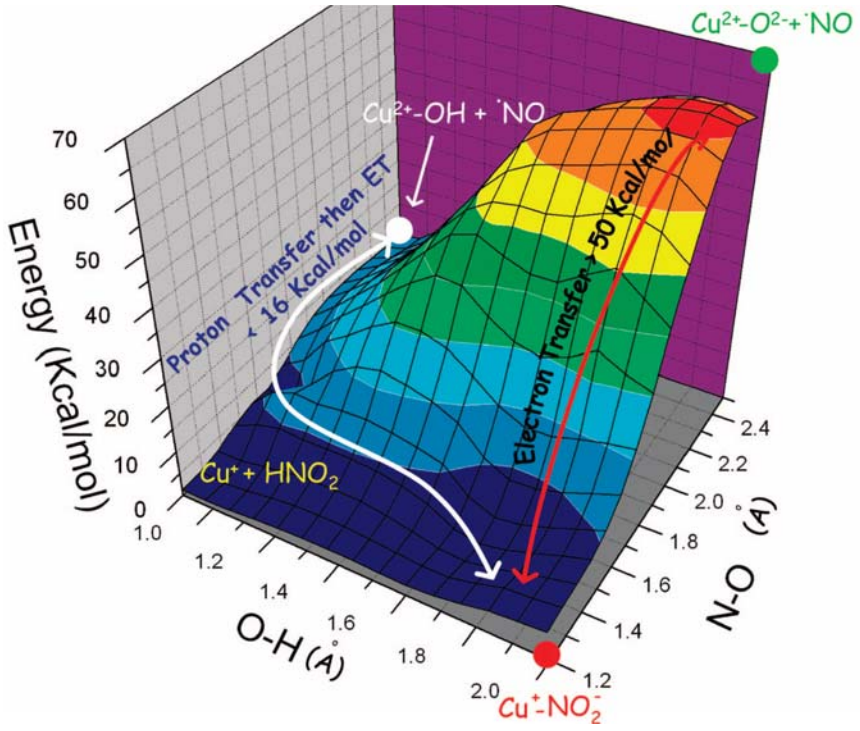

Figure 2.15 Two-dimensional potential energy surface for the N-O bond cleavage of nitrite in the key Cu(I)-NO_2^- intermediate of CuNIR.[15] Reprinted with permission from ref. 15. Copyright 2009 American Chemical Society.

2.1.5 Copper(I)-Nitrosyl Complexes

The reaction of reduced CuNIR with NO_2^- is well known to produce NO, however, NO is also known to be an inhibitior of CuNIR. Other known inhibitors of CuNIR activity include DDC (diethyl dithiocarbamate), CN^- and CO.[3] Since CO is a π-backbonding

ligand somewhat similar to NO, but unreactive, Cu(I)-CO complexes have also been studied in great detail as models for Cu(I)-NO adducts.[58,88-97] These studies have shown that CO is a very sensitive probe for the electron richness of a Cu(I) center,[58,88,91,98] and correspondingly, Cu(I)-CO complexes have gained much attention. Here, the CO adduct of CuNIR shows the C-O stretch at 2050 cm^{-1},[99] which is very similar to Tp^- complexes; for example, [Cu($Tp^{i\text{-}Pr,i\text{-}Pr}$)(CO)] shows the C-O stretch at 2056 cm^{-1}.[88]

Interestingly, whereas low concentrations of NO inhibit CuNIR, larger concentrations of NO have been shown to lead to the formation of N_2O, as discussed above.[46] In this respect, Tolman and coworkers have shown that Cu(I) model complexes like Cu(I)-Tp, Figure 2.15, facilitate the disproportionation of NO following Equation **1**.[48,58] This produces N_2O and the corresponding Cu(II)-NO_2^- complex as shown in Figure 2.17.[48,58] A similar reaction has been observed for Mn(II)-NO complexes.[100]

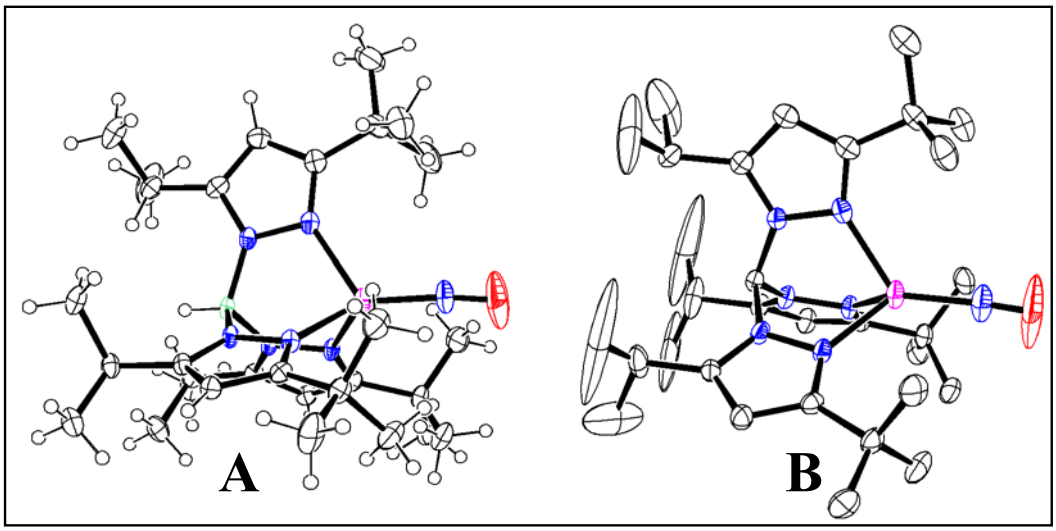

Figure 2.16 Crystal structure of [Cu($Tp^{t\text{-}Bu,i\text{-}Pr}$)(NO)] (**A**) and of the corresponding tris(pyrazolyl)methane complex [Cu($Tpm^{t\text{-}Bu,i\text{-}Pr}$)(NO)]$^+$ (**B**).[16]

Inspired by the finding that CuNIR is able to produce N_2O from NO and by these model complex studies, it has been proposed that CuNIR could protect cells from NO toxicity by shifting from NIR to NOR activity in the presence of large amounts of NO. It is unknown if there is any other biological relevance of Cu(I)-NO complexes or if other copper enzymes interact with NO under physiological conditions. However, it has been

shown that Cu(I) complexes can release NO from nitrosothiols,[101] which is another potentially important biological function of Cu(I) centers.

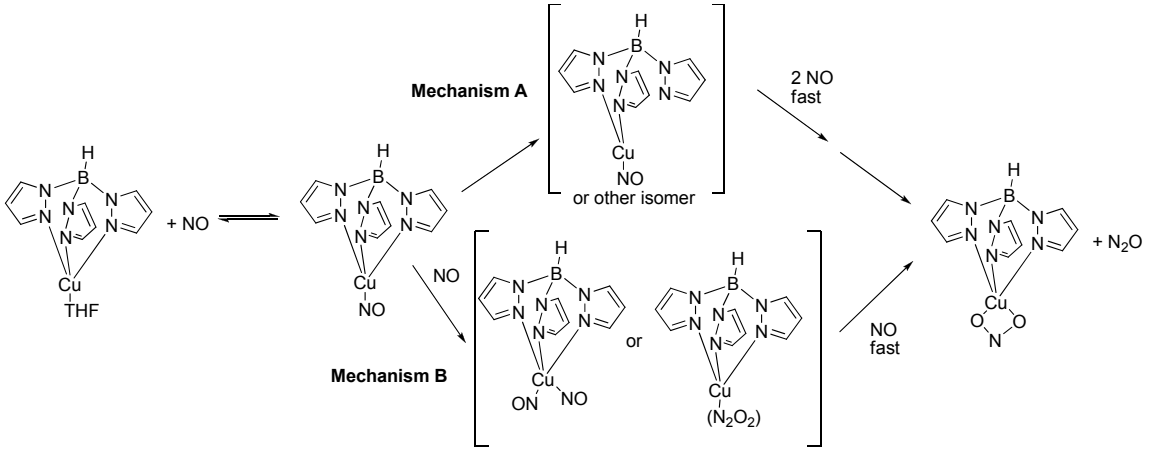

Figure 2.17 Proposed mechanism for NO disproportionation by Cu(I) complexes.[58]

Table 2.8 Geometric parameters and vibrational frequencies of [Cu(Tp)(NO)] and [Cu(Tpm)(NO)]$^+$ complexes.

Parameters	Experimental Data $[Cu(X)(NO)]^{n+}$ where X =			Computational Data $[Cu(X)(NO)]^{n+}$ where X =	
	$Tp^{t\text{-Bu,H}}$	$Tp^{t\text{-Bu},i\text{-Pr}}$	$Tpm^{t\text{-Bu},i\text{-Pr}}$	$Tp^{Me,Me}$	$Tpm^{Me,Me}$
Cu-NO	1.759 Å	1.779 Å	1.786 Å	1.812 Å	1.818 Å
Cu-N_{pz}	2.044 Å	2.051 Å	2.058 Å	2.011 Å	2.036 Å
Cu-N_{pz}	2.054 Å	2.053 Å	2.070 Å	2.040 Å	2.040 Å
Cu-N_{pz}	2.091 Å	2.064 Å	2.070 Å	2.128 Å	2.172 Å
N-O	1.108 Å	1.083 Å	1.035 Å	1.188 Å	1.178 Å
<(Cu-N-O)	163.4°	171.9°	176.4°	148°	147°
ν (N-O)	1712 cm^{-1}	1698 cm^{-1}	1742 cm^{-1}	1707 cm^{-1}	1758 cm^{-1}
ν (Cu-NO)	-	365/338 cm^{-1}	369/344 cm^{-1}	456/458 cm^{-1}	453 cm^{-1}
Ref	102-103	16	16	16	16

Only a few Cu(I)-NO model complexes have been synthesized and spectroscopically and structurally characterized to this date.[16,102-106] The most in-depth characterized compounds utilize hydrotris(pyrazolyl)borate (Tp^-) and related coligands.[16,102-103] In addition to the model complexes, crystal structures of Cu(I)-NO adducts of CuNIR have been reported by Murphy and coworkers. Interestingly, the Cu(I)-NO protein crystal structures show side-on bound NO ligands as discussed above.[9,34,39] In comparison, all Cu(I)-NO model complexes structurally characterized so far are observed

to have end-on bound Cu-N-O units with Cu-N-O angles of ranging from 163° to 176°, (*cf.* Table 2.8 and Figure 2.16). The protein and model complex data are therefore in surprising disagreement with respect to the geometry of the Cu-N-O unit.

UV-Vis absorption and MCD data of [Cu(Tp)(NO)] complexes were analyzed by Lehnert and coworkers. The MCD data do not show the presence of d-d transitions at low energy in these compounds, indicating that these complexes do in fact contain Cu(I) centers. The complexes therefore have a Cu(I)-NO(radical) electronic structure, which is supported by EPR spectroscopy and DFT calculations.[16,102,107] DFT calculations on the different Cu-N-O binding modes have further shown that the end-on bound Cu(I)-NO form is generally preferred and is about 3-10 kcal/mol lower in energy than the side-on bound structure.[10,16-17,108-110] In addition, DFT calculations indicate that the electronic structure of the Cu(I)-NO unit is of Cu(I)-NO(radical) type independent of the binding mode of NO. [10,16-17,111]

The EPR spectrum of the Cu(I)-NO adduct of CuNIR was first analyzed by Murphy and coworkers, and based on the results, it was proposed that this complex should be considered to be of Cu(II)-NO^- type.[9] However, Solomon and coworkers showed later that this EPR spectrum was identical to that of oxidized CuNIR with bound NO_2^-. This result was further confirmed by ENDOR and MCD spectroscopy.[10] Usov et al. later obtained the EPR spectrum of the Cu(I)-NO adduct of CuNIR in solution and determined the key EPR parameters of this species.[112] The Cu(I)-NO complex in the enzyme was found to have g-values of 2.046, 1.998 ($g_\perp$) and 1.926 ($g_\parallel$). Interestingly, the $g_\parallel$ value for CuNIR of 1.926 is distinctly larger than those of the [Cu(Tp)(NO)] model complexes as shown in Table 2.9. DFT calculations by Hiller and coworkers and Lehnert and coworkers have shown that this is not a random finding, but that there is a strong correlation between the Cu-N-O angle and the $g_\parallel$ values of the Cu(I)-NO complexes.[16,108-109] Here, the principal axis of $g_\parallel = g_z$ is located almost exactly along the Cu-N_{NO} axis.[16] As shown in Figure 2.18, model complexes with close to linear Cu-N-O angles show $g_\parallel \sim 1.8$ (*cf.* Table 2.9). In sharp contrast, the Cu(I)-NO adduct of CuNIR in solution exhibits a much larger $g_\parallel$ value of 1.93.[112] The correlation plot in Figure 2.15 provides strong evidence that based on this $g_\parallel$ value, the Cu(I)-NO adduct of CuNIR is in fact strongly bent (Cu-N-O angle: ~140°) in solution, but not side-on as observed in the

CuNIR crystal structures. This surprising result is further supported by DFT calculations on simplified models of the CuNIR active site.[10,16-17]

Table 2.9 Experimental and computational EPR g-values for Cu(I)-NO complexes.

Experimental	$g_\perp$	$g_\parallel$	Cu-N-O	Ref
Cu^I-NO in CuNIR	2.046, 1.998	1.926	?	112
[Cu(Tp$^{t\text{-Bu,H}}$)(NO)]	1.99	1.83	163°	102
[Cu(Tp$^{t\text{-Bu},i\text{-Pr}}$)(NO)]	1.97	1.80	172°	16
Computational				
[Cu(Tp^{Me,Me})(NO)] opt	2.019, 2.012	1.902	154°	16
[Cu(Tp^{Me,Me})(NO)] 172°	2.019, 1.999	1.783	172°	16
[Cu(Tpm^{Me,Me})(NO)]$^+$ opt	2.015, 2.012	1.907	155°	16
[Cu(Tpm^{Me,Me})(NO)]$^+$ 174°	2.016, 1.998	1.786	174°	16

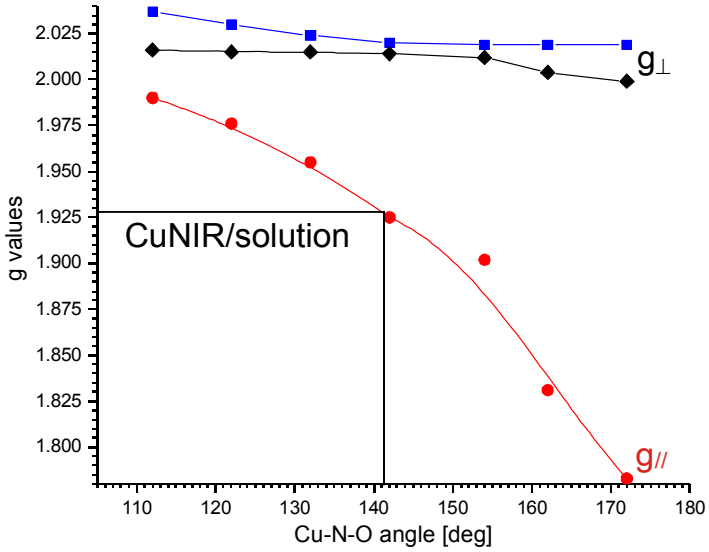

Figure 2.18 Calculated *g*-values for Cu(I)-NO complexes as a function of the Cu-N-O angle.[16]

2.2 Computational Analysis of Cu(I)-NO in the CuNIR Active Site

There are multiple theories for the cause of the unusual side-on bound Cu(I)-NO geometry in the crystal structure of reduced CuNIR (PDB: 1SNR)[9]. Recent experimental and theoretical results provide evidence that a side-on bound NO is a possible binding mode of NO due to second coordination sphere effects: particularly, the Asp-98 side chain forming a hydrogen bond to the copper-bound NO and the bulky Ile-257 residue sterically interacting with the copper-bound ligands, in this case NO.[5,9,16,109,112] DFT

calculations were used to further investigate the effect primary and secondary sphere amino acids have on the energy difference between the end-on and side-on bound Cu(I)-NO.

2.2.1 Experimental

2.2.1.1 Density Functional Calculations.

Initial coordinates for the active site models were obtained from an experimentally determined CuNIR crystal structure with bound NO by Tocheva et al. (PDB: 1SNR)[9] and were optimized using the BP86 functional[113-114] and the TZVP basis set.[115-116] Unless otherwise mentioned, all active site models contained copper, nitric oxide, three coordinated histidine residues, His-100, His-135, and His-306, all of which had the protein backbone deleted and a $-CH_3$ group used as an anchor instead of the backbone as shown in Figure 2.19. Initially, simple calculations with the inner sphere amino acids (the three histidine residues mentioned above) directly bound to the copper site were examined. Then, more complex calculations were undertaken to include two key secondary sphere amino acids, asparic acid (Asp-98) and isoleucine (Ile-257).

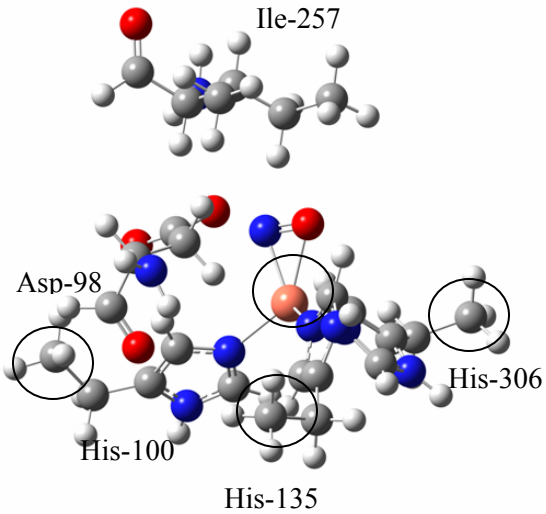

Figure 2.19 Scheme of the CuNIR active site highlighting atoms which were fixed for all calculations (circled). His-100, His-135, and His-306 were truncated and $-CH_3$ groups were used as anchors where the histidines were attached to the protein backbone and fixed in space.

In this case, the backbone amide groups of Asp-98 and Ile-257 were changed to aldehydes. Geometry optimizations were performed with the program package Gaussian

03,[117] while orbitals were plotted from single point calculations using the ORCA package using BP86/TZVP.[118]

2.2.2 Results and Discussion

In order to further investigate the side-on and end-on binding mode that Cu(I)-NO has been observed to have experimentally and spectroscopically in the CuNIR active site, two different models were computationally analyzed as mentioned previously. First, a simple model with only the first coordination sphere taken into account (**2.2.2.1**) will be discussed followed by an analysis of a more complex model system with the secondary sphere amino acids included (**2.2.2.2**).

2.2.2.1 Simple Cu(I)-NO Computational CuNIR Model

In order to investigate the end-on and side-on coordination of NO to copper, DFT geometry optimized structures of the CuNIR active site with bound NO were analyzed.[113-116] The optimization of the CuNIR active site with only the first coordination sphere amino acids taken into account produced a Cu-N-O angle of 136^{o} (*cf.* figure 2.20, bottom left), which is in between end-on (**>**160°; from the model complexes)[102] and side-on (71°; from Murphy's structure) Cu(I)-NO structures.[9] In order to generate both an end-on and side-on structure, Cu-N-O angles were fixed at 170° and 67°, respectively, and reoptimized. The resulting geometries are shown in Figure 2.20, top and bottom right.

To test whether these three structures follow the trend in g_z values as described in section 2.1.4, the *g-tensor*s for the three binding modes were calculated. Importantly, as shown in Figure 2.20, *the general trend that as the Cu-N-O unit bends the EPR g-value of g_z goes up is followed by the computational CuNIR models*. The calculated g_z value of the optimized model with a Cu-N-O angle of 137^{o} was calculated to be 1.952 while the more linear bound NO with a Cu-N-O angle of 170^{o} was calculated to have a g_z value of 1.812. Based on these results the solution EPR parameters of the Cu(I)-NO species in CuNIR, as determined by Scholes and coworkers, do in fact reflect a strongly bent Cu(I)-NO structure. Comparison of the calculated *g*-tensors with the g-values obtained by Scholes

and coworkers shows the best agreement between the fully optimized structure (Cu-N-O angle = 136°; *cf.* Figure 2.20, bottom left) and the experimental data. However, the calculated difference in g-values between this structure and the side-on bound species is relatively small, so it would be unjustified to claim that the fully optimized structure exactly reflects the Cu(I)-NO geometry present in the enzymatic species detected in solution. Nevertheless, *the results clearly indicate that the Cu(I)-N-O unit is strongly bent in the enzyme in solution and not linear like in the model complexes.*

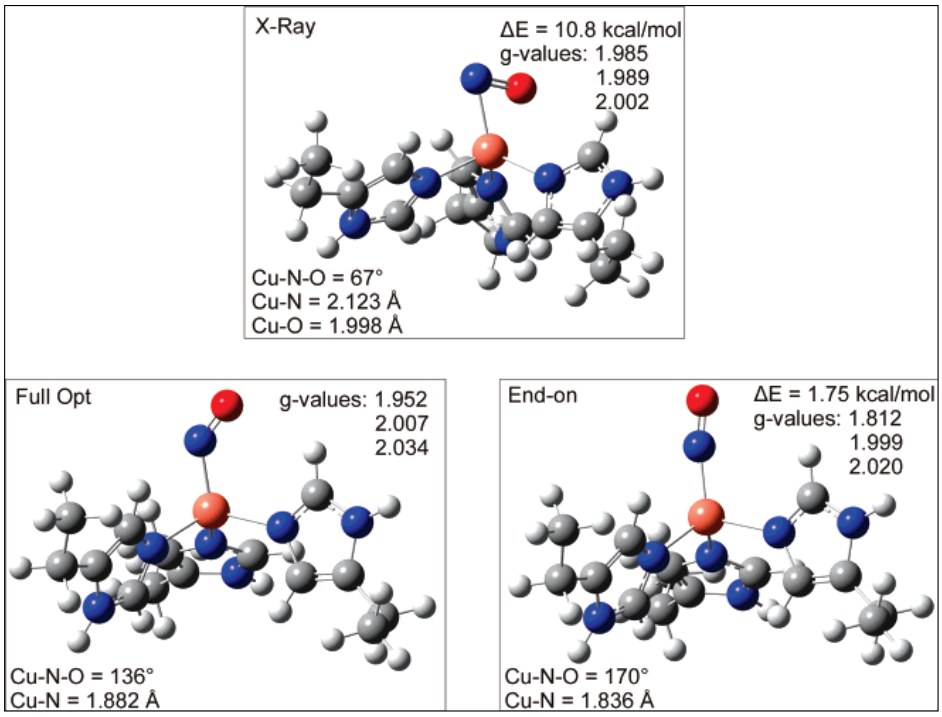

Figure 2.20 Geometry optimized (BP86/TZVP) structures of Cu(I)-NO species in CuNIR. For these calculations, the anchor atoms (C atoms of the artificial CH_3 groups) of the three histidines were frozen at their crystallographic positions. Top: optimized structure with frozen Cu-N-O angle at the crystallographically determined value.[9] Bottom, left: fully optimized structure. Bottom, right: optimized structure with frozen Cu-N-O angle at a value typical for the model complexes. Listed are relative energies with respect to the fully optimized structure and calculated g-values for the three structures (BP86/TZVP).

2.2.2.2 Extended Cu(I)-NO Computational CuNIR Model

Previous, DFT calculations indicate that Cu(I)-NO binds end-on preferentially by 3-10 kcal/mol.[10,15-16,108-110] This poses the important question of how the protein active site promotes NO side-on binding as found in the crystal structure, or whether this is instead an artifact, in particular since the structure changes to end-on bound in solution.[108-112]

Starting from the exact crystal structure of side-on bound NO in CuNIR, the NO ligand was optimized to determine whether the DFT calculations would reproduce the side-on binding observed experimentally when the secondary sphere amino acids (Asp-98 and Ile-257) were present. Surprisingly, the optimization resulted in a side-on bound NO with a CuNO angle of 76.5°. The resulting structure, **1**, corresponds to a local minimum on the potential energy surface (PES), Figures 2.21 and 2.22 respectively. This is confirmed by a PES scan (Figure 2.22) which shows an energy barrier of +1.0 kcal/mol to change the geometry from side-on to end-on. This is in agreement with DFT results by Hillier and coworkers for a model complex, where a similar barrier was calculated.[108-109] *This result shows that the side-on Cu(I)-NO structure in fact exists as a local minimum.*

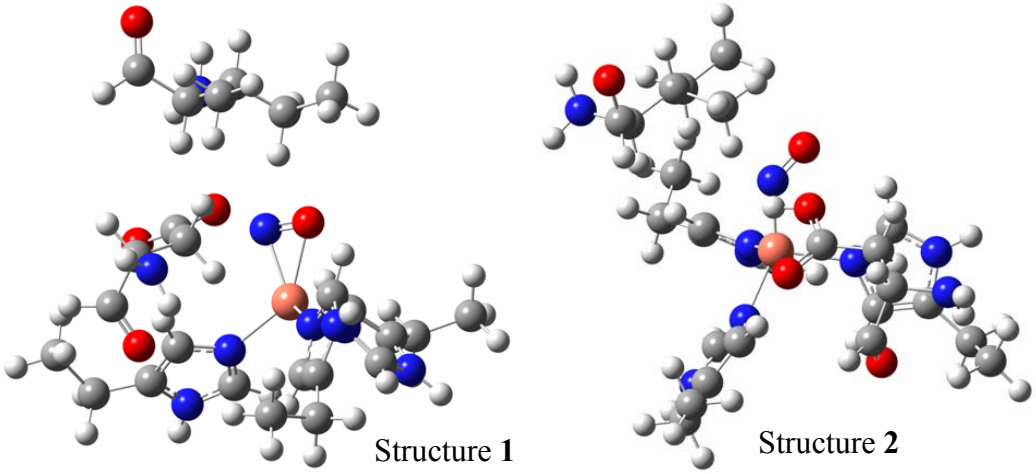

Figure 2.21 Optimized structures **1** and **2** with side-on, local minimum, and end-on, global minimum, bound NO.

Within the PES scan a global minimum was observed when the nitrosyl snaps from the side-on bound structure to the end-on bound structure **2**, 8.4 kcal/mol lower than **1** (see Table 2.10 and Figure 2.22). This number is again in agreement with previous DFT calculations.[10,15-16,108-109] Further end-on bound structures were optimized and found that other end-on bound structures were generally 6-8 kcal/mol lower in energy than **1**. The different end-on bound Cu-NO structures were found due to movement of the NO around in the active site to avoid the bulky Ile-257 as indicated in Figure 2.23, left. *This clearly shows that end-on bound NO is sterically restricted by Ile-257, which therefore is a key player in determining the CuNO geometry.* Usov et al. speculated, based on ENDOR, that NO experiences a non-covalent perturbation by the Ile bulky side chain in the end-on bound structure in solution.[112] The closeness of NO and the Ile-257 protons in the

calculated end-on structures in Figure 2.23, left, are in agreement with this idea. In contrast, the steric interaction in the side-on geometry is minimal: removing Ile-257 from model **1** and reoptimization of NO leads to a slightly increased CuNO angle of 84^{o}.

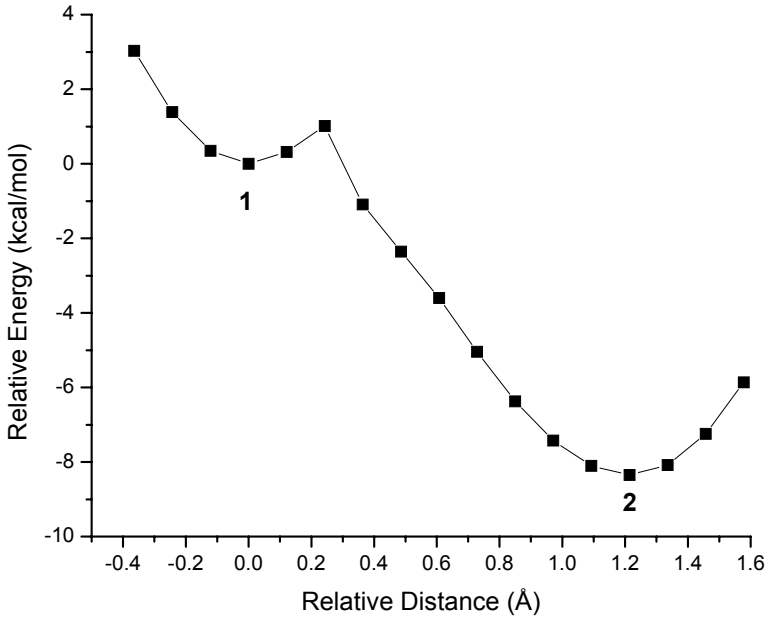

Figure 2.22 In order to obtain the potential energy surface (PES) scan, the coordinates of the NO of structure **1** and **2** were superimposed, and a linear path connecting the N atoms in these structures was calculated. The differences in the x, y and z coordinates were each divided by ten in order to obtain 10 incremental steps to move the N from the position in **1** to that of **2**.

Removal of Ile-257 and Asp-98 from the active site model **1** in Figure 2.21 and reoptimization of NO resulted in the end-on structure, **3**, 10.8 kcal/mol lower in energy than **1** (Figure 2.23, right). *Overall, end-on binding of NO is therefore intrinsically more favorable than side-on coordination, even in the Cu(His)$_3$ motif in the CuNIR active site*. If the obtained NO orientation in **3** is incorporated into the complete active site model **1**, the energy increases to +14 kcal/mol relative to **1** due to severe steric interactions with Ile-257, again emphasizing the directing role of Ile-257 for the NO orientation. In structure **1** and the related structures in Figure 2.23, left, the energy gain for end-on binding is reduced from 10.8 to 6-8 kcal/mol (Figure 2.23, right), in part reflecting the steric congestion of the CuNIR active site due to Ile-257.

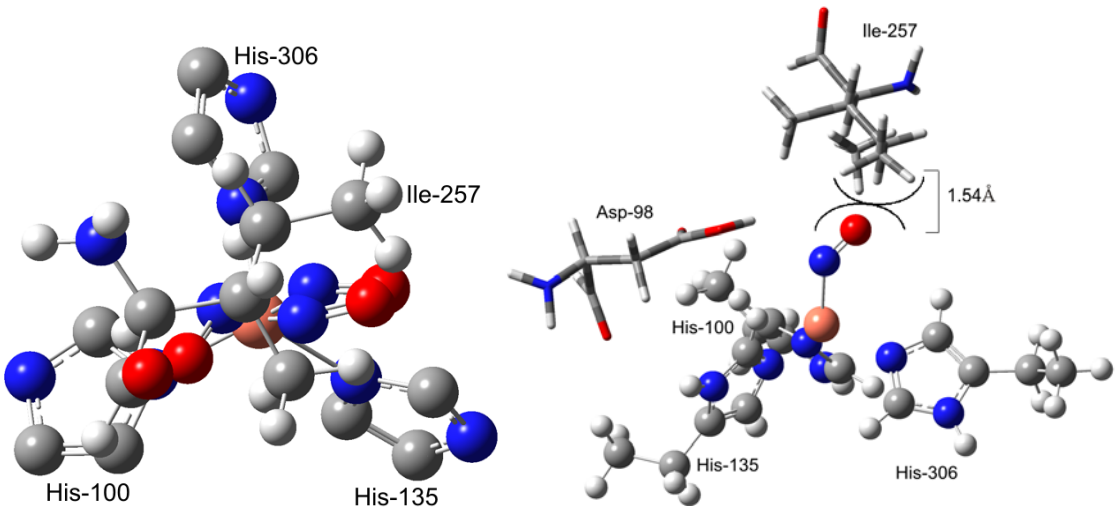

Figure 2.23 Left: Different energy minima with end-on bound NO in the active site of CuNIR. Right: Structure **3**, optimization of NO without Ile-257 and Asp-98. Ile and Asp are shown in tube form in their crystallographic positions. The presence of Ile prevents this intrinsically preferred end-on orientation because of an unfavorable steric interaction.

Table 2.10 Geometric parameters of the optimized structures.

Structure	Energy [kcal/mol]	Cu-N-O [degrees]	H-bond [Å]
1(X-ray)	+25.2	67.4	1.77
1	0	76.5	2.13
2	-8.4	133.9	2.79
3	-10.8	137.3	-
4	-16.1	131.6	2.42

Tocheva et al. speculated that Asp-98 stabilizes the side-on geometry *via* a hydrogen bond.[9] In addition, Periyasamy et al. also state that the Asp-98 is crucial in the formation of the side-on bound complex.[109] To explore the possible role of this hydrogen bond, we calculated its total energy using structure **1** and formic acid as a model, *resulting in a total hydrogen bond energy of only 3.3 kcal/mol.* This energy is too small to counteract the ~8 kcal/mol energy gain for the side-on to end-on transition and hence, the hydrogen bond cannot be the main reason for the experimentally observed side-on Cu-NO structure. In addition, since the hydrogen bond length increases only by ~0.7 Å from side-on to end-on, the total change in hydrogen bond energy is only 1-2 kcal/mol. The hydrogen bond is therefore *not* the deciding factor for side-on binding. However, this hydrogen bond is key for the generation of the local energy minimum for the side-on structure; removal of Asp-98 in **1** and reoptimization of NO in fact generates an end-on

structure. In this way, *Asp-98 assists in but does not cause the side-on coordination of NO*. Tocheva et al. also proposed that the hydrogen bond with Asp-98 determines the orientation of NO such that its N-atom points towards Asp-98.[9] However, we found that inverting the orientation of NO gave an energy change of -0.80 kcal/mol relative to **1**, with the lowest energy geometry actually being opposite to Tocheva's proposed structure. The small energy difference suggests that both orientations could be present in the crystal (see also ref. 8). *In summary, the hydrogen bond will not orient the NO in the CuNIR active site nor cause the observed side-on binding*.

Having ruled out the hydrogen bond causing the side-on binding, we investigated the effect of the histidine orientation on the binding mode. Starting from structure **3** and using the initial side-on (from **1**, **1-His**) or the optimized end-on orientation of NO (**3-His**), we optimized the histidines with the CuNO units frozen, leading to an energy gain of 9.6 and 9.3 kcal/mol, respectively, for the side-on and end-on orientation. Interestingly, both cases produce the same histidine movement. *This demonstrates that the histidine orientation in CuNIR does not discriminate between side-on and end-on binding*.

Finally, optimizing the NO and histidines in structure **1** while keeping the other atoms fixed causes an energy gain of 16.1 kcal/mol; giving the end-on structure **4**. This energy difference can be incrementally calculated from the previous results, using i) the energy difference between end-on and side-on binding of NO (-8.4 kcal/mol), ii) the energy gain from the histidine movement (-9.3 kcal/mol), and iii) the loss of hydrogen bonding (about +1 kcal/mol). Adding up these numbers, we predict an energy of -16.7 kcal/mol for structure **4** relative to **1**, close to the calculated energy difference. Hence, the values (i-iii) represent incremental energy changes in the CuNIR active site.

The DFT results also allow us to analyze the electronic structures in different NO binding modes. The side-on structure exhibits a spin density profile similar to those presented in refs. 109, 111. The singly occupied molecular orbital (SOMO) of the complex shown in Figure 2.24, left has 91% π^* character with 7% metal d-admixture, forming a δ-type bond. The lowest unoccupied molecular orbital (LUMO) represents a classic π-backbond between Cu and NO. In the end-on structure, the SOMO has 77% π* and 14% Cu-d character (*cf.* Figure 2.24, right), forming a π bond. The LUMO corre-

sponds to a somewhat unusual π-backbond mediated by d_{z2}, which differs from the model complexes.[16] This interesting difference may cause the discrepancy in CuNO angles, where the predicted end-on CuNO angle in CuNIR of 134° is distinctly smaller than observed in the model complexes (160°-175°).[16,102] In both the side-on and end-on case, the electronic structure is clearly of Cu^{I}-NO(radical) type, rather than a spin-coupled Cu^{II}-NO^{-} system, in agreement with refs. 109, 111. The weaker Cu-NO bond in the side-on case is due to a reduction in backbonding, caused by the weak orbital overlap of the δ bond. In this way, the side-on structure mediates an overall weaker Cu-to-NO backbond, and hence, a lower binding energy of NO.

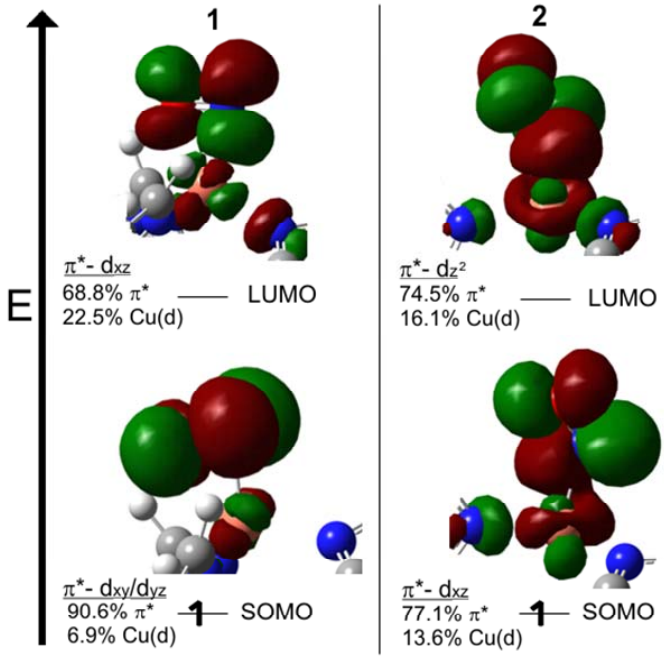

Figure 2.24 Visualization of the SOMO and LUMO of **1** and **2**.

In summary, using DFT calculations we were able to determine i) that the Cu-NO side-on structure observed in CuNIR corresponds to a local minimum while ii) the end-on structure is 6-8 kcal/mol more stable; iii) that Ile-257 determines the orientation of NO in the CuNIR active site; iv) that the hydrogen bond is only worth about 3 kcal/mol, which assists in stabilizing the side-on form, and finally, v) that the first coordination sphere histidine movement is similar for the side-on and end-on geometry. Therefore, our results point toward Ile-257 being the predominate amino acid to affect the side-on binding rather than Asp-98 as the major contributor, as the literature suggests.[9,108-109]

2.2.3 Conclusions

The geometry of the Cu(I)-NO subunit in proteins and model complexes has a much larger flexibility in terms of the coordination mode of NO and the Cu-N-O angle than previously anticipated from model complex studies. These results are also in agreement with the crystal structure of NO bound amine oxidase, which shows a Cu(I)-N-O angle of 117° (assuming that this species corresponds to a Cu(I)-NO complex, which, however, is somewhat unclear in this case).[119]

The side-on structure found in the protein seems to be largely due to steric interactions with Ile-257. This destabilizes the end-on relative to the side-on structure. In addition, Figure 2.23 left, only shows a static picture with a "frozen" Ile-257; however, in the protein, the dynamics of Ile motion and internal vibrations must be considered. Under these conditions, the effective space demand of Ile-257 will further increase. This likely causes the observed side-on geometry in the crystal structure, where the overall orientation of the protein side chains must therefore be strongly restricted. Correspondingly, a small change in conformation in solution that slightly reorients Ile-257 would then allow the NO to bind end-on as observed in solution for CuNIR and the known model complexes.[16,108-109] This is due to the fact that intrinsically, the end-on structure is always energetically favored. More insight into the dynamics of the CuNIR active site will require molecular dynamics simulations of crystalline CuNIR.

2.3 Spectroscopic and Computational Studies of Cu-NO_x Model Complexes With Hydrotris(triazolyl)borate Type Ligands

As mentioned earlier in 2.1.3 and 2.1.4 a number of model complexes with nitric oxide and nitrite have been synthesized and analyzed in great detail. Hydrotris(pyrazolyl)borate ligands (Tp^-) have been used to model the binding of both nitrite and nitrosyls to Cu(II) and Cu(I) in order to model the active species in the mechanism of CuNIR.[16,103,107] A similar ligand system with hydrotris(triazolyl)borate ligands (Ttz^-) was used here to probe the differences in geometry and electronic structure Ttz-Cu(II) complexes have when compared with similar Tp-Cu(II) complexes (*cf.* Scheme 2.6). Within Part 2 of Chapter 2 EPR spectroscopy and computational models were use to probe the geometry and electronic structure of a series of Ttz-Cu(II) complexes.

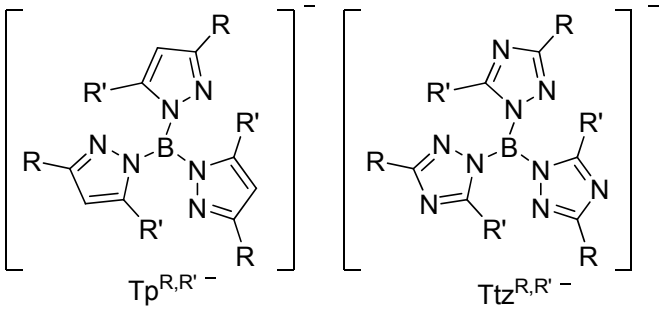

Scheme 2.6 Molecular structures of $Tp^{R,R'-}$ and $Ttz^{R,R'-}$, where R and R' are on the 3, 5 positions respectively.

2.3.1 Experimental

2.3.1.1 Density Functional Calculations

Structures were optimized using the BP86 functional[113-114] and the TZVP basis set.[115-116] The EPR parameters were calculated using both BP86/TZVP and B3LYP/TZVP.[120-122] Geometry optimizations were performed with the program package Gaussian 03.[117] EPR parameters were calculated and orbitals were plotted from single point calculations using the ORCA package.[118] Crystal structure coordinates of trigonal-bipyramidal $Ttz^{t\text{-}Bu,Me}Cu(\eta^2\text{-}NO_3)$ and $Tp^{t\text{-}Bu,Me}Cu(\eta^2\text{-}NO_3)$ were used for the EPR and optimization calculations in addition to calculating the SOMO percent contributions.[123] The EPR parameters and SOMO percent contributions were calculated using square-pyramidal geometries of $Ttz^{i\text{-}Pr,i\text{-}Pr}Cu(\eta^2\text{-}NO_3)$ and $Tp^{i\text{-}Pr,i\text{-}Pr}Cu(\eta^2\text{-}NO_3)$, which were obtained by changing the pyrazole to triazole and nitrite to nitrate with the coordinates of the crystal structure, $Ttz^{i\text{-}Pr,i\text{-}Pr}Cu(\eta^2\text{-}NO_2)$.[61,98,124] The hydrotris(triazolyl)borate (Ttz^-) ligated copper complexes were calculated using crystal structure data provided by Dr. Elizabeth Papish's Lab from Drexel University, Philadelphia.[125]

2.3.1.2 Electron Paramagnetic Resonance (EPR)

A Bruker X-band EMX spectrometer equipped with an Oxford Instruments liquid nitrogen cryostat was used for EPR measurements. EPR spectra were typically obtained on frozen solutions (~77K) or solid samples using ~ 20 mW microwave power and 100 kHz field modulation with the amplitude set to 1 G. Sample concentrations employed

were ~ 5 mM in dichloromethane. Samples were prepared by Dr. Mukesh Kumar at Drexel University.

2.3.2 Results and Discussion

2.3.2.1 EPR Spectroscopy

The electronic structure of TtzCu(II) complexes were analyzed *via* EPR spectroscopy. The experimental and simulated EPR spectra of Ttz$^{t\text{-Bu,Me}}$Cu(η^2-NO_3) are shown in Figure 2.25, left. In the EPR spectrum of Ttz$^{t\text{-Bu,Me}}$Cu(η^2-NO_3) there is nitrogen superhyperfine splitting from three of the triazole nitrogens. In order to obtain a satisfactory fit of the EPR spectrum of Ttz$^{t\text{-Bu,Me}}$Cu(η^2-NO_3) nitrogen superhyperfine splittings for three triazole nitrogens had to be included in the fit as observed in the inset of Figure 2.25, left, where the blue is the poor fit obtained without the nitrogens coupling. This is remarkable, since, nitrogen superhyperfine splitting is not observed in the analogous pyrazole complex, Tp$^{t\text{-Bu,Me}}$Cu(η^2-NO_3).[123] The green simulated spectrum has the fit parameters: $g_z = 2.3$, $g_y = 2.0855$, $g_x = 2.0444$; copper hyperfine: $^{Cu}A_z = 343$ MHz, $^{Cu}A_y = 80$ MHz, $^{Cu}A_x = 116$ MHz; nitrogen hyperfine: $^{N}A_z = 25$ MHz, $^{N}A_y = 37$ MHz, $^{N}A_x = 46$ MHz (*cf.* Table 2.11).

The nitrogen hyperfine coupling constants of about 20-50 MHz show that there is some radical character transferred from the copper to the triazole ligands. This is also observed in the spectrum of the Ttz$^{t\text{-Bu,Me}}$Cu(η^2-NO_2) complex, Figure 2.26, left. The superhyperfine splitting is not observed in the solid sample EPR of Ttz$^{t\text{-Bu,Me}}$Cu(η^2-NO_3) or Ttz$^{t\text{-Bu,Me}}$Cu(η^2-NO_2), Figure 2.25 and Figure 2.26, (right) respectively. In addition the superhyperfine splitting is not observed in the solution EPR spectrum of the pyrazole bound copper complex, Tp$^{t\text{-Bu,Me}}$Cu(η^2-NO_2), Figure 2.27. The superhyperfine splitting from the triazole nitrogens are resolved in the Ttz$^{t\text{-Bu,Me}}$Cu(II) species and not the Tp-Cu(II) complexes which is indicative of spin density being transferred to the triazole nitrogens in the Ttz$^{t\text{-Bu,Me}}$Cu(II) species but not the Tp-Cu(II) species.

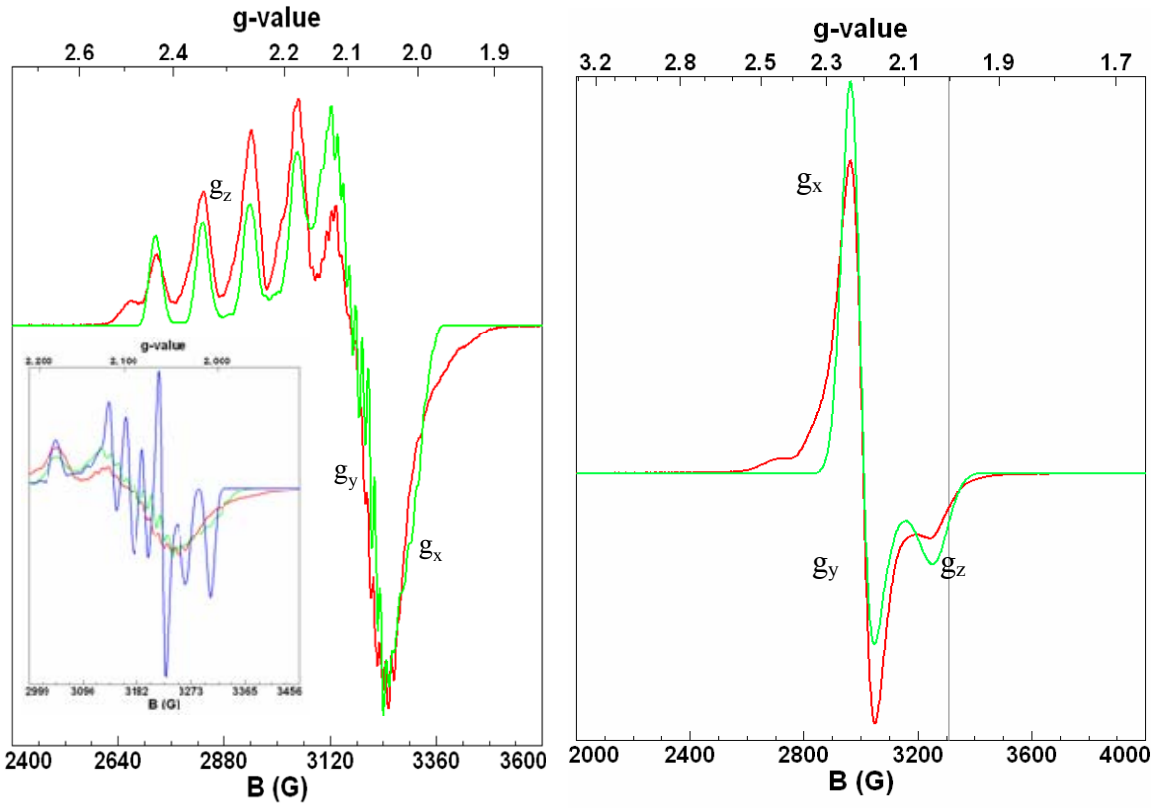

Figure 2.25 Left: EPR spectrum of Ttz$^{t\text{-Bu,Me}}$Cu(η^2-NO_3) recorded at 77 K in frozen dichloromethane (red) and fit to the spectrum using the program SpinCount (green). Fit parameters: g_z = 2.3, g_y = 2.0855, g_x = 2.0444; Hyperfine: $^{Cu}A_z$ = 343 MHz, $^{Cu}A_y$ = 80 MHz, $^{Cu}A_x$ = 116 MHz. The fit requires the presence of three equivalent nitrogen atoms each with I=1. Coupling constants: $^{N}A_z$ = 25 MHz, $^{N}A_y$ = 37 MHz, $^{N}A_x$ = 46 MHz. Presumably each triazole ring contributes one nitrogen in the approximate 3-fold symmetry of the complex. Right: EPR spectrum of Ttz$^{t\text{-Bu,Me}}$Cu(η^2-NO_3) recorded at 77 K in solid form (red) and fit to the spectrum using the program SpinCount (green). Fit parameters: g_z = 2.03, g_y = 2.2, g_x = 2.24 with no observable hyperfine splitting.

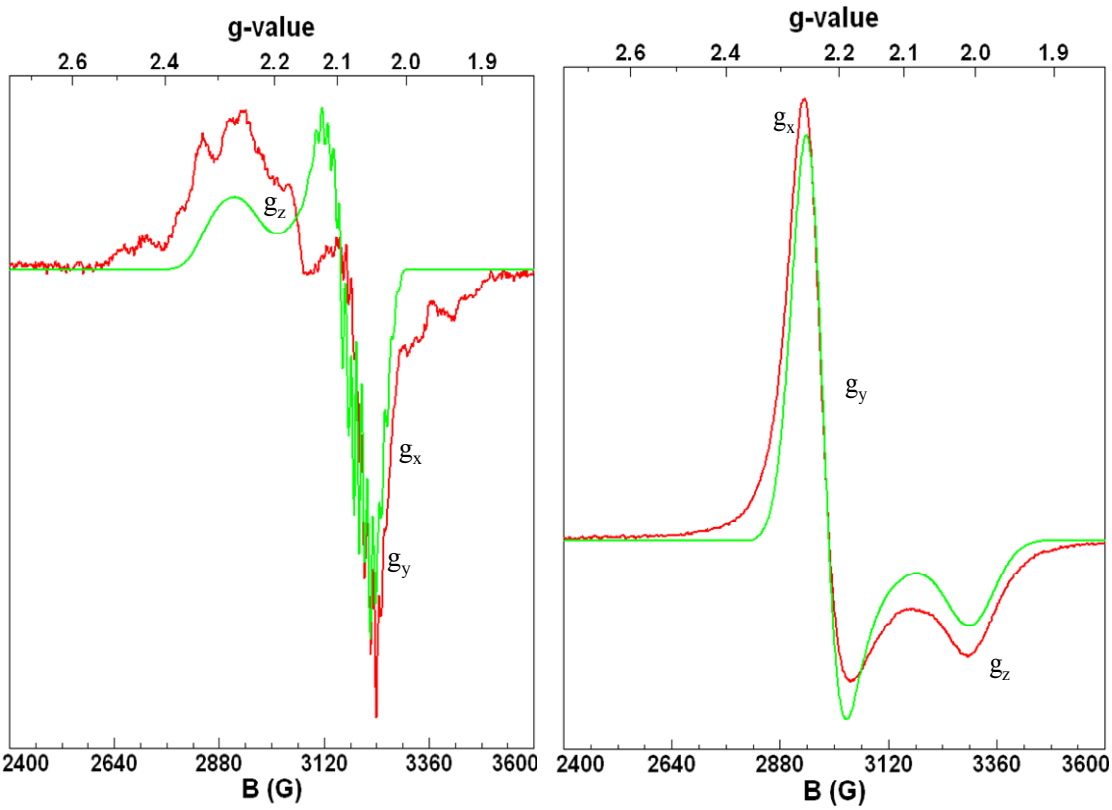

Figure 2.26 Left: EPR spectrum of Ttz$^{t\text{-Bu,Me}}$Cu(η^2-NO_2) recorded at 77 K in frozen dichloromethane(red) and fit to the spectrum using the program SpinCount (green). Fit parameters: g_z = 2.28, g_y = 2.072, g_x = 2.069; Hyperfine: $^{Cu}A_z$ = 100 MHz, $^{Cu}A_y$ = 116 MHz, $^{Cu}A_x$ = 52 MHz. The fit requires the presence of three equivalent nitrogen atoms. Coupling constants: $^{N}A_z$ = 25 MHz, $^{N}A_y$ = 38 MHz, $^{N}A_x$ = 25 MHz. Right: EPR spectrum of Ttz$^{t\text{-Bu,Me}}$Cu(η^2-NO_2) recorded at 77 K in solid form (red) and fit to the spectrum using the program SpinCount (green). Fit parameters: g_z = 2.0, g_y = 2.22, g_x = 2.26 with no observable hyperfine splitting.

Copper(II) complexes in general are known to have g-values where $g_z > g_x, g_y$ as seen in Ttz$^{t\text{-Bu,Me}}$Cu(η^2-NO_3) and Ttz$^{t\text{-Bu,Me}}$Cu(η^2-NO_2), Figure 2.25 and 2.26, (left) respectively. This characteristic g-value order, where $g_z > g_x, g_y$ corresponds to a d_{x2-y2} ground state.[124,126] When $g_z < g_x, g_y$ as observed in the solid state EPR spectra Ttz$^{t\text{-Bu,Me}}$Cu(η^2-NO_3) and Ttz$^{t\text{-Bu,Me}}$Cu(η^2-NO_2) in Figure 2.25 and 2.26, (right) the ground state is instead d_{z2}. This difference in ground states in the solid and solution EPR spectra of Ttz$^{t\text{-Bu,Me}}$Cu(η^2-NO_3) and Ttz$^{t\text{-Bu,Me}}$Cu(η^2-NO_2), is most likely due to a change in geometry from the solid state to the solution state. The solid state EPR spectra (Figure 2.25 and Figure 2.26, right) show line broadening as usually observed for pure paramagnetic solids. This geometry change was further analyzed using DFT calculations

to predict the calculated A-values and percent contribution of the singly occupied molecular orbitals (SOMOs). This is further discussed below. The simulation (green) of the EPR spectrum of Ttz$^{t\text{-Bu,Me}}$Cu(η^2-NO_3) fits well with the experimental data (red), (Figure 2.25, left) while the fit for the NO_2^- fits less well. This fit is indicative of contaminants within the sample as shown in Figure 2.25, left, with undefined hyperfine splitting in the g_z region.

Table 2.11 Simulated EPR parameter for the structure of Ttz$^{t\text{-Bu,Me}}$Cu(η^2-NO_3) and Ttz$^{t\text{-Bu,Me}}$Cu(η^2-NO_2).

	Ttz$^{t\text{-Bu,Me}}$Cu(η^2-NO_3)		Ttz$^{t\text{-Bu,Me}}$Cu(η^2-NO_2)	
	Solid	Solution	Solid	Solution
g_x	2.24	2.0441	2.26	2.069
g_y	2.20	2.0855	2.22	2.072
g_z	2.03	2.3	2.00	2.28
CuA_x	-	116 MHz	-	52 MHz
CuA_y	-	80 MHz	-	116 MHz
CuA_z	-	343 MHz	-	100 MHz
NA_x	-	25 MHz	-	25 MHz
NA_y	-	37 MHz	-	38 MHz
NA_z	-	46 MHz	-	25 MHz

Changes in geometry have been observed when coordinating solvents are added to tetrahedral complexes as observed in Figure 2.28. A rhombic EPR spectrum of the tetrahedral Ttz$^{t\text{-Bu,Me}}$Cu-Cl complexes (Figure 2.28, left) transforms into an axial EPR spectrum with the addition of DMF (Figure 2.28, right). The Ttz$^{t\text{-Bu,Me}}$Cu-Cl complexes changes geometry from tetrahedral to a five-coordinate complex that has a d_{x2-y2} ground state, a square-pyramidal Ttz$^{t\text{-Bu,Me}}$Cu(DMF)Cl complex as seen in Figure 2.28, right.[124] Interestingly hyperfine splitting is observed in the square-pyramidal Ttz$^{t\text{-Bu,Me}}$Cu(DMF)Cl while the tetrahedral Ttz$^{t\text{-Bu,Me}}$Cu-Cl has no hyperfine splitting from the triazole nitrogens, Figure 2.28.

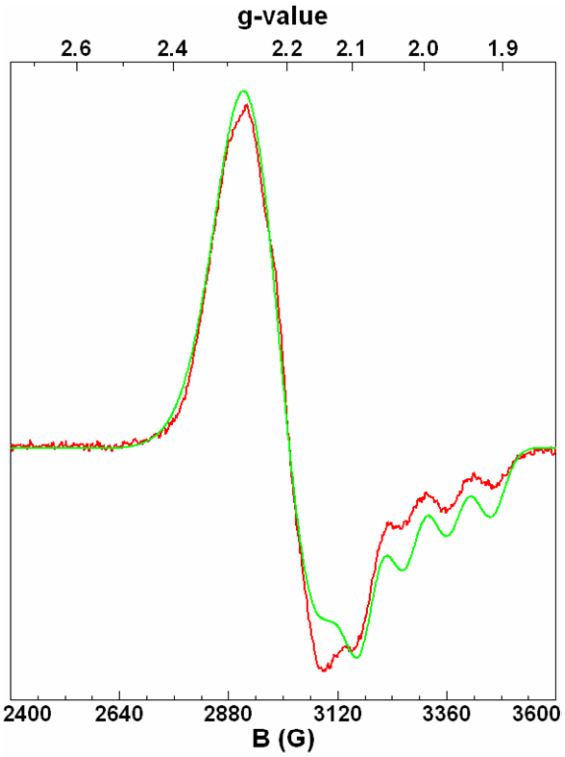

Figure 2.27 EPR spectrum of Tp $^{t\text{-Bu,Me}}$ Cu(η^2-NO_2) recorded at 77 K in frozen dichloromethane (red) and fit to the spectrum using the program SpinCount (green). Fit parameters: $g_z = 1.995$, $g_y = 2.217$, $g_x = 2.268$; Hyperfine: $^{Cu}A_z = 263$ MHz, $^{Cu}A_y = 105$ MHz, $^{Cu}A_x = 90$ MHz.

Table 2.12 Geometric parameters of Ttz$^{t\text{-Bu,Me}}$Cu(NO_3), Tp$^{t\text{-Bu,Me}}$Cu(NO_3) and Tp$^{i\text{-Pr,}i\text{-Pr}}$Cu($NO_2$) as taken from the crystal structures along with the optimized structure.

	Ttz $^{t\text{-Bu,Me}}$ Cu(η^2-NO_3)		Tp $^{t\text{-Bu,Me}}$ Cu(η^2-NO_3)		Tp$^{i\text{-Pr,}i\text{-Pr}}$Cu($\eta^2$-$NO_2$)[61]
	Crystal	Opt	Crystal	Opt	Crystal Structure
Cu-O(1)	2.10 Å	2.16 Å	2.12 Å	2.19 Å	2.02 Å
Cu-O(2)	1.98 Å	2.05 Å	2.01 Å	2.05 Å	2.03 Å
Cu-N1	1.96 Å	2.01 Å	1.96 Å	2.01 Å	1.97 Å
Cu-N2	2.07 Å	2.12 Å	2.03 Å	2.08 Å	2.00 Å
Cu-N3	2.09 Å	2.12 Å	2.16 Å	2.17 Å	2.11 Å
N1-Cu-O1	108°	107°	107°	107°	103°
N2-Cu-O1	128°	128°	138°	135°	151°
N3-Cu-O1	128°	129°	117°	120°	113°
N1-Cu-O2	170°	169°	167°	168°	161°
N2-Cu-O2	96°	97°	95°	96°	101°
N3-Cu-O2	96°	97°	98°	97°	104°
τ^a	0.72	0.68	0.48	0.53	0.17

[a] $\tau = (\alpha - \beta)/60^\circ$, where α and β are the largest angles ($\alpha > \beta$) around a 5-coordinate metal center. The parameter τ is equal to 0 for an ideal square-pyramidal geometry while t is equal to 1 for a perfect trigonal-bipyramidal geometry.[127]

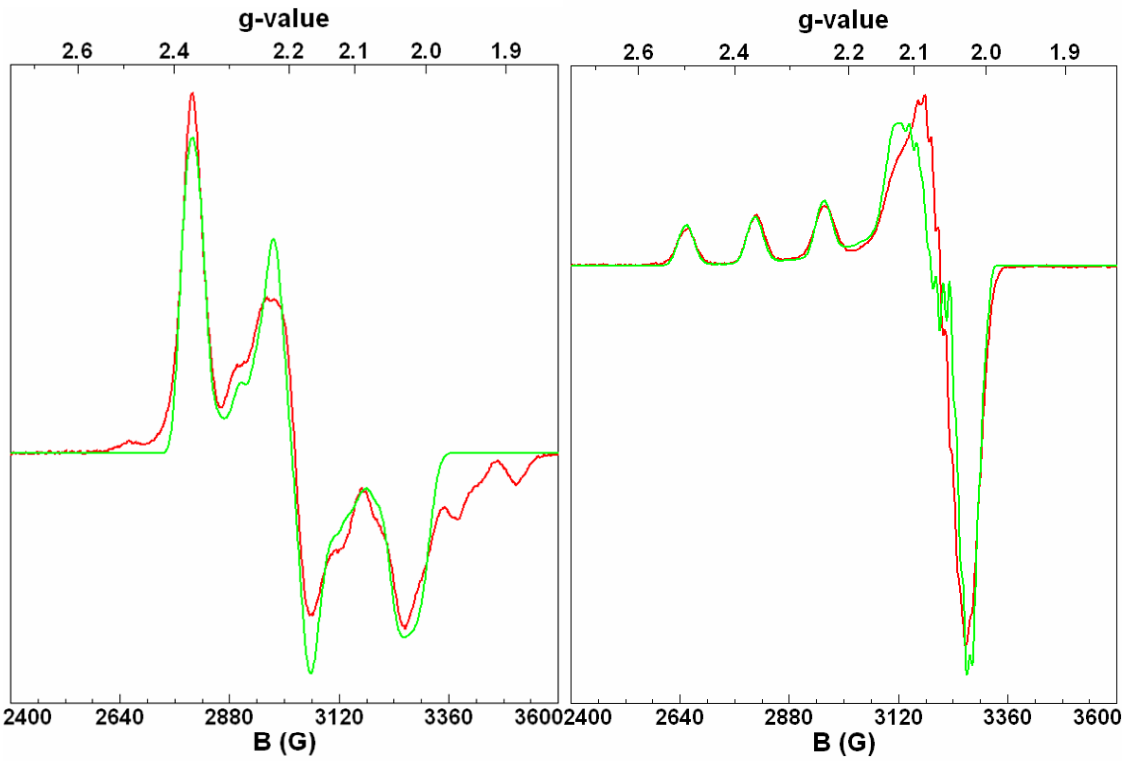

Figure 2.28 Left: EPR spectrum of Ttz$^{t\text{-Bu,Me}}$Cu-Cl recorded at 77 K in frozen dichloromethane (red) and fit of the spectrum using the program SpinCount (green). Fit parameters: $g_z = 2.367$, $g_y = 2.194$, $g_x = 2.022$; Hyperfine: $^{Cu}A_z = 46$ MHz, $^{Cu}A_y = 57$ MHz, $^{Cu}A_x = 63$ MHz. For the simulated spectrum hyperfine splitting was included for g_x, g_y, and g_z in order to obtain as many of the observed features as possible. Right: EPR spectrum of Ttz$^{t\text{-Bu,Me}}$Cu-Cl with a drop of DMF (presumable now Ttz$^{t\text{-Bu,Me}}$Cu(DMF)Cl) added to the solution at 77 K in frozen dichloromethane (red) and fit of the spectrum using the program SpinCount (green). Fit parameters: $g_z = 2.3$, $g_y = 2.0659$, $g_x = 2.063$; Hyperfine: $^{Cu}A_z = 487$ MHz, $^{Cu}A_y = 49$ MHz, $^{Cu}A_x = 85$ MHz. The fit requires the presence of three equivalent nitrogen atoms each with I = 1. Coupling constants: $^{N}A_z = 25$ MHz, $^{N}A_y = 39$ MHz, $^{N}A_x = 46$ MHz.

Experimentally, we were able to probe the differences in electronic structure and geometry of Ttz-Cu(II) complexes as compared with Tp-Cu(II) complexes. It was found that Ttz-Cu(II) complexes show nitrogen superhyperfine splitting while Tp-Cu(II) complexes do not. In addition an unusual change in geometry was observed experimentally when the EPR spectra of solid Ttz-Cu(II) complexes were taken in solution. These differences in electronic structure and geometry were further analyzed using DFT calculations.

2.3.2.2 Computational Results

2.3.2.2.1 Computational Analysis of Copper Nitrate Complexes

The current investigation of experimental EPR spectra of Ttz$^{t\text{-Bu,Me}}$Cu(η^2-NO_3) and Tp$^{t\text{-Bu,Me}}$Cu(η^2-NO_3) show a change in geometry from the solid state to the solutions state. Computational analyses of the solid state structures were used to investigate the change in geometry observed in the EPR spectra. The structure of the solid state complexes are know due to crystal structures while the solution state geometries can only be inferred. The crystal structure of Ttz$^{t\text{-Bu,Me}}$Cu(η^2-NO_3) shows a slightly distorted trigonal-bipyramidal geometry, with a τ-value of 0.72 (Table 2.12). A τ-value of 1 is indicative of a trigonal-bipyramidal complex while a τ-value of 0 is square-pyramidal. The experimental EPR spectrum in solution of Ttz$^{t\text{-Bu,Me}}$Cu(η^2-NO_3) has a d_{x2-y2} ground state that is closer to square-pyramidal in solution. For this reason we sought to computationally analyze the electronic structure and geometry change observed in the experimental EPR spectra with DFT calculations. DFT-optimizations of the crystal structures of Ttz$^{t\text{-Bu,Me}}$Cu(η^2-NO_3) and Tp$^{t\text{-Bu,Me}}$Cu(η^2-NO_3) reproduced the crystal structures quite accurately with τ-values of 0.68 and 0.72 for the optimized and crystal structures for Ttz$^{t\text{-Bu,Me}}$Cu(η^2-NO_3) respectively and 0.53 and 0.48 for the optimized and crystal structures for Tp$^{t\text{-Bu,Me}}$Cu(η^2-NO_3) respectively (see Table 2.12). For example, the bond distances between the crystal structures and the optimized structures only differ by 0.07 Å, while the angles differ by only 3^o (*cf.* Table 2.12). The optimized structures are almost identical to the crystal structures of the complexes. It is possible that the optimized crystal structures do not reflect the solution geometries well. In order to take into account a change in geometry from the solid state to the solution state, square-pyramidal complexes were used to calculate hyperfine coupling constants for the solution spectra. Calculating the nitrogen hyperfine coupling constants for a d_{x2-y2} ground state structure (square-pyramidal) does not reveal a significant difference in the nitrogen hyperfine coupling constants between the Ttz$^-$ and Tp$^-$ complexes. For example, the square-pyramidal Ttz$^{i\text{-Pr},i\text{-Pr}}$Cu($\eta^2$-$NO_3$) complex has calculated A-values of 38, 31 and 2 MHz while the square-pyramidal Tp$^{i\text{-Pr},i\text{-Pr}}$Cu($\eta^2$-$NO_3$) has calculated A-values of 46, 38, and 2 MHz using BP86/TZVP as shown in Table 2.13. This slight difference between the

Ttz^- and Tp^- square-pyramidal complexes shows that the pyrazole should be a slightly stronger donor than the triazole. These results are counter to the experimental results, where the Ttz^- complexes have superhyperfine splitting while the analogous Tp^- complexes do not. This small difference in A-values between the two complexes may be within computational error and thus not completely accurate.

Table 2.13 EPR parameter calculated for the structure of $Ttz^{t\text{-}Bu,Me}Cu(\eta^2\text{-}NO_3)$ and $Tp^{t\text{-}Bu,Me}Cu(\eta^2\text{-}NO_3)$. BP86/TZVP and B3LYP/TZVP were used to compare the results between the two functionals.

A_{iso} values	Trigonal-bipyramidal Geometry				Square-pyramidal Geometry			
	Cu-Ttz crystal		Cu-Tp crystal		Ttz		Tp	
	BP86	B3LYP	BP86	B3LYP	BP86	B3LYP	BP86	B3LYP
N1 [MHz]	40.8414	44.5072	44.4354	45.7642	38.1813	43.1228	46.3257	47.3828
N2 [MHz]	21.3147	21.5119	35.5515	35.8542	30.9167	35.0703	38.0308	38.6905
N3 [MHz]	20.9369	22.3098	10.4305	9.6639	1.6630	1.2107	1.9981	1.3635
g-values	2.0058	2.0054	2.0131	2.0172	2.0276	2.0437	2.0276	2.0447
	2.0937	2.1518	2.0796	2.1258	2.0517	2.0829	2.0517	2.0858
	2.1059	2.1628	2.1239	2.1901	2.1202	2.1893	2.1202	2.1938
iso	2.0685	2.1067	2.0722	2.1110	2.0665	2.1053	2.0665	2.1081

Table 2.14 Percent contribution of the α and β SOMO for the different geometries of copper(II) nitrate complexes.

		Cu(d)	NO_3	N (triazole/pyrazole)
$Ttz^{t\text{-}Bu,Me}Cu(\eta^2\text{-}NO_3)$ trigonal-bipyramidal	α	34.0%	31.5%	28.9%
	β	52.3%	24.4%	18.3%
$Tp^{t\text{-}Bu,Me}Cu(\eta^2\text{-}NO_3)$ trigonal-bipyramidal	α	36.9%	34.3%	20.7%
	β	52.8%	24.9%	9.6%
$Ttz^{i\text{-}Pr,i\text{-}Pr}Cu(\eta^2\text{-}NO_3)$ square-pyramidal	α	33.1%	30.9%	30.0%
	β	51.3%	25.8%	18.1%
$Tp^{i\text{-}Pr,i\text{-}Pr}Cu(\eta^2\text{-}NO_3)$ square-pyramidal	α	35.9%	34.0%	20.2%
	β	53.3%	25.7%	14.8%

Finally, the differences between the SOMOs of $Ttz^{t\text{-}Bu,Me}Cu(\eta^2\text{-}NO_3)$ and $Tp^{t\text{-}Bu,Me}Cu(\eta^2\text{-}NO_3)$ complexes were analyzed to further understand the differences in hyperfine splitting observed experimentally. A DFT calculation of the electronic structure of $Ttz^{t\text{-}Bu,Me}Cu(\eta^2\text{-}NO_3)$ (using the trigonal-bipyramidal crystal structure geometry) shows that the SOMO of the complex has large contributions of Cu (34% d), nitrate (32%) and triazole nitrogens (29%), as shown in Table 2.14. A similar calculation was

performed on $Ttz^{i\text{-}Pr,i\text{-}Pr}Cu(\eta^2\text{-}NO_3)$, using the hypothetical square-pyramidal geometry, and in this case an overall similar SOMO is obtained (Cu: 33% d; nitrate: 31%; pyrazoles: 30%). The SOMOs of the two $Tp^{t\text{-}Bu,Me}Cu(\eta^2\text{-}NO_3)$ geometries also have essentially the same magnitude of percent contribution; therefore, the two different geometries should have similar hyperfine coupling constants (as determined in the calculated nitrogen A-values, above). However, there is one key difference: in the case of the triazole complex, the contribution of the triazole ligand to the SOMO is distinctively larger compared to the analogous pyrazole ligand, indicating that Ttz^- is a somewhat stronger σ donor to copper(II) compared to the analogous Tp^- ligand (Table 2.14).

2.3.2.2.2 Computational Analysis of Copper-Nitrosyl Complexes

The unexpected difference between hydrotris(pyrazolyl)borate and hydrotris(triazolyl)borate ligands (difference in σ donation) was further investigated through the computational analysis of $Tp^{Me,Me}Cu(NO)$ and $Ttz^{Me,Me}Cu(NO)$. The slightly stronger electron accepting Ttz^- ligand when bound to Cu(I)-NO could decrease π-backbonding between the Cu(I) and NO and cause a weaker Cu-N_{NO} bond. This weaker Cu-N_{NO} bond would make an overall less stable Cu(I)-NO complex and thus increase the reactivity of the system. The change in the electronic structure for $Tp^{Me,Me}Cu(NO)$ and $Ttz^{Me.Me}Cu(NO)$ was analyzed by optimizing the complexes and calculating the SOMO percent contribution of the NO, Cu(I) and Ttz^-/Tp^- using BP86/TZVP. The optimized structures were shown to have nearly identical bent Cu(I)-NO structures with Cu-N-O angles of 148° (*cf.* Table 2.15). The percent contributions of the SOMOs were also calculated to be very similar (*cf.* Table 2.16).

In summary, computational results were unable to attain any electronic differences between the Ttz^- and Tp^- ligand when bound to Cu(I)-NO and thus no significant difference in the reactivity of these two Cu(I)-NO complexes are expected.

Table 2.15 Geometric parameters of $Ttz^{Me,Me}Cu(NO)$ and $Tp^{Me,Me}Cu(NO)$ (in brackets) using BP86/TZVP.[16]					
Bond	Bond Distance [Å]	Angle	Bond Angle [deg]	Angle	Bond Angle [deg]
Cu-NO	1.82 [1.81]	Cu-N-O	148 [148]	N1-Cu-N2	92
N-O	1.18 [1.19]	N1-Cu-N_{NO}	113	N1-Cu-N3	91
N1-Cu	2.21	N2-Cu-N_{NO}	129	N2-Cu-N3	95
N2-Cu	2.02	N3-Cu-N_{NO}	127		
N3-Cu	2.04				

Table 2.16 Percent character of Cu(I)-NO SOMOs.		
	$Ttz^{Me,Me}Cu(NO)$	$Tp^{Me,Me}Cu(NO)$[16]
π^*_h	76.7 %	71 %
Cu(d)	15.8 %	19 %
Cu(s,p)	3.2 %	3 %
Ligand	4.3 %	7 %

2.3.3 Conclusions

Spectroscopic and computational data were used to analyze the electronic differences between $Ttz^{t\text{-}Bu,Me}$ and the analogous $Tp^{t\text{-}Bu,Me}$ ligand when bound to copper. Based on the EPR and computational results, we propose that Ttz^- is a slightly stronger σ-donor than Tp^- when bound to copper. Experimentally $Ttz^{t\text{-}Bu,Me}Cu(II)$ complexes show nitrogen superhyperfine coupling while $Tp^{t\text{-}Bu,Me}Cu(II)$ has no spectral resolution of any superhyperfine splitting. DFT calculated nitrogen hyperfine coupling constants support the idea that the coordinating nitrogen atoms are responsible for the observed superhyperfine splitting in the experimental EPR spectra. However, the calculations also predict overall similar nitrogen superhyperfine coupling constants in the analogous Ttz^- and Tp^- complexes, which disagrees with our experimental findings (Table 2.13). This indicates that the differences between Ttz^- and Tp^- might be more subtle than one would expect based on the EPR results.

Finally, spectroscopy and computational data were used to analyze the change in geometry observed for the Ttz^- complexes in solid and solution. It was concluded that the solution structures are most likely square-pyramidal, but computationally the EPR parameters using a square-pyramidal geometry do not accurately reflect the experimental

EPR parameters and a better model is needed in order to further analyze the spectra computationally.

2.4 References

(1) Averill, B. A. *Chem. Rev.* **1996**, *96*, 2951-2964.

(2) Bertini, I. *Biological Inorganic Chemistry: Structure and Reactivity*; University Science Books: Sausalito, Calif., 2007.

(3) Zumft, W. G. *Microbiol. Mol. Biol. Rev.* **1997**, *61*, 533-616.

(4) Suzuki, S.; Kataoka, K.; Yamaguchi, K. *Acc. Chem. Res.* **2000**, *33*, 728-735.

(5) Suzuki, S.; Kataoka, K.; Yamaguchi, K.; Inoue, T.; Kai, Y. *Coord. Chem. Rev.* **1999**, *192*, 245-265.

(6) Wasser, I. M.; de Vries, S.; Moenne-Loccoz, P.; Schroder, I.; Karlin, K. D. *Chem. Rev.* **2002**, *102*, 1201-1234.

(7) Inatomi, K.; Hochstein, L. I. *Curr. Microbiol.* **1996**, *32*, 72-76.

(8) Coyne, M. S.; Arunakumari, A.; Averill, B. A.; Tiedje, J. M. *Appl. Environ. Microb.* **1989**, *55*, 2924-2931.

(9) Tocheva, E. I.; Rosell, F. I.; Mauk, A. G.; Murphy, M. E. *Science* **2004**, *304*, 867-870.

(10) Ghosh, S.; Dey, A.; Usov, O. M.; Sun, Y.; Grigoryants, V. M.; Scholes, C. P.; Solomon, E. I. *J. Am. Chem. Soc.* **2007**, *129*, 10310-10311.

(11) Chen, C. S.; Yeh, W. Y. *Chem. Comm.* **2010**, *46*, 3098-3100.

(12) Kujime, M.; Izumi, C.; Tomura, M.; Hada, M.; Fujii, H. *J. Am. Chem. Soc.* **2008**, *130*, 6088-6098.

(13) Sarma, M.; Kalita, A.; Kumar, P.; Singh, A.; Mondal, B. *J. Am. Chem. Soc.* **2010**, *132*, 7846-7847.

(14) Wright, A. M.; Wu, G. A.; Hayton, T. W. *J. Am. Chem. Soc.* **2010**, *132*, 14336-14337.

(15) Ghosh, S.; Dey, A.; Sun, Y.; Scholes, C. P.; Solomon, E. I. *J. Am. Chem. Soc.* **2009**, *131*, 277-288.

(16) Fujisawa, K.; Tateda, A.; Miyashita, Y.; Okamoto, K.; Paulat, F.; Praneeth, V. K. K.; Merkle, A.; Lehnert, N. *J. Am. Chem. Soc.* **2008**, *130*, 1205-1213.

(17) Merkle, A. C.; Lehnert, N. *Inorg. Chem.* **2009**, *48*, 11504-11506.

(18) Nojiri, M.; Xie, Y.; Inoue, T.; Yamamoto, T.; Matsumura, H.; Kataoka, K.; Deligeer; Yamaguchi, K.; Kai, Y.; Suzuki, S. *Proc. Natl. Acad. Sci. U. S. A.* **2007**, *104*, 4315-4320.

(19) Kukimoto, M.; Nishiyama, M.; Murphy, M. E. P.; Turley, S.; Adman, E. T.; Horinouchi, S.; Beppu, T. *Biochemistry* **1994**, *33*, 5246-5252.

(20) Ellis, M. J.; Antonyuk, S. V.; Strange, R. W.; Sawers, G.; Eady, R. R.; Hasnain, S. S. *Inorg. Chem.* **2004**, *43*, 7591-7593.

(21) Karlin, K. D.; Tyeklár, Z. *Bioinorganic Chemistry of Copper*; Chapman & Hall: New York, 1993.

(22) Godden, J. W.; Turley, S.; Teller, D. C.; Adman, E. T.; Liu, M. Y.; Payne, W. J.; LeGall, J. *Science* **1991**, *253*, 438-442.

(23) Adman, E. T.; Godden, J. W.; Turley, S. *J. Biol. Chem.* **1995**, *270*, 27458-27474.

(24) Ellis, M. J.; Dodd, F. E.; Sawers, G.; Eady, R. R.; Hasnain, S. S. *J. Mol. Biol.* **2003**, *328*, 429-438.

(25) Murphy, M. E. P.; Turley, S.; Kukimoto, M.; Nishiyama, M.; Horinouchi, S.; Sasaki, H.; Tanokura, M.; Adman, E. T. *Biochemistry* **1995**, *34*, 12107-12117.

(26) Jacobson, F.; Guo, H.; Olesen, K.; Okvist, M.; Neutze, R.; Sjolin, L. *Acta Crystallogr., Sect. D.* **2005**, *61*, 1190-1198.

(27) Jacobson, F.; Pistorius, A.; Farkas, D.; De Grip, W.; Hansson, O.; Sjolin, L.; Neutze, R. *J. Biol. Chem.* **2007**, *282*, 6347-6355.

(28) Solomon, E. I. *Inorg. Chem.* **2006**, *45*, 8012-8025.

(29) Veselov, A.; Olesen, K.; Sienkiewicz, A.; Shapleigh, J. P.; Scholes, C. P. *Biochemistry* **1998**, *37*, 6095-6105.

(30) Olesen, K.; Veselov, A.; Zhao, Y. W.; Wang, Y. S.; Danner, B.; Scholes, C. P.; Shapleigh, J. P. *Biochemistry* **1998**, *37*, 6086-6094.

(31) Suzuki, S.; Yoshimura, T.; Kohzuma, T.; Shidara, S.; Masuko, M.; Sakurai, T.; Iwasaki, H. *Biochem. Biophys. Res. Comm.* **1989**, *164*, 1366-1372.

(32) Libby, E.; Averill, B. A. *Biochem. Biophys. Res. Comm.* **1992**, *187*, 1529-1535.

(33) Strange, R. W.; Dodd, F. E.; Abraham, Z. H.; Grossmann, J. G.; Bruser, T.; Eady, R. R.; Smith, B. E.; Hasnain, S. S. *Nat. Struct. Biol.* **1995**, *2*, 287-292.

(34) Antonyuk, S. V.; Strange, R. W.; Sawers, G.; Eady, R. R.; Hasnain, S. S. *Proc. Natl. Acad. Sci. U. S. A.* **2005**, *102*, 12041-12046.

(35) Murphy, M. E.; Turley, S.; Adman, E. T. *J. Biol. Chem.* **1997**, *272*, 28455-28460.

(36) Boulanger, M. J.; Murphy, M. E. *Biochemistry* **2001**, *40*, 9132-9141.

(37) Barrett, M. L.; Harris, R. L.; Antonyuk, S.; Hough, M. A.; Ellis, M. J.; Sawers, G.; Eady, R. R.; Hasnain, S. S. *Biochemistry* **2004**, *43*, 16311-16319.

(38) Leferink, N. G. H.; Han, C.; Antonyuk, S. V.; Heyes, D. J.; Rigby, S. E. J.; Hough, M. A.; Eady, R. R.; Scrutton, N. S.; Hasnain, S. S. *Biochemistry* **2011**, *50*, 4121-4131.

(39) Tocheva, E. I.; Rosell, F. I.; Mauk, A. G.; Murphy, M. E. P. *Biochemistry* **2007**, *46*, 12366-12374.

(40) Boulanger, M. J.; Murphy, M. E. P. *Protein Sci.* **2003**, *12*, 248-256.

(41) Dodd, F. E.; Hasnain, S. S.; Abraham, Z. H. L.; Eady, R. R.; Smith, B. E. *Acta Crystallogr. D* **1997**, *53*, 406-418.

(42) Dodd, F. E.; Van Beeumen, J.; Eady, R. R.; Hasnain, S. S. *J. Mol. Biol.* **1998**, *282*, 369-382.

(43) Averill, B. A. *Angew. Chem. Int. Ed.* **1994**, *33*, 2057-2058.

(44) Halfen, J. A.; Mahapatra, S.; Wilkinson, E. C.; Gengenbach, A. J.; Young, V. G.; Que, L.; Tolman, W. B. *J. Am. Chem. Soc.* **1996**, *118*, 763-776.

(45) Halfen, J. A.; Tolman, W. B. *J. Am. Chem. Soc.* **1994**, *116*, 5475-5476.

(46) Jackson, M. A.; Tiedje, J. M.; Averill, B. A. *FEBS Letters* **1991**, *291*, 41-44.

(47) Ye, R. W.; Torosuarez, I.; Tiedje, J. M.; Averill, B. A. *J. Biol. Chem.* **1991**, *266*, 12848-12851.

(48) Ruggiero, C. E.; Carrier, S. M.; Tolman, W. B. *Angew. Chem. Int. Ed.* **1994**, *33*, 895-897.

(49) Kataoka, K.; Furusawa, H.; Takagi, K.; Yamaguchi, K.; Suzuki, S. *J. Biochem.* **2000**, *127*, 345-350.

(50) De Marothy, S. A.; Blomberg, M. R. A.; Siegbahn, P. E. M. *J. Comput. Chem.* **2007**, *28*, 528-539.

(51) Hulse, C. L.; Averill, B. A.; Tiedje, J. M. *J. Am. Chem. Soc.* **1989**, *111*, 2322-2323.

(52) Halfen, J. A.; Mahapatra, S.; Olmstead, M. M.; Tolman, W. B. *J. Am. Chem. Soc.* **1994**, *116*, 2173-2174.

(53) Jiang, F.; Conry, R. R.; Bubacco, L.; Tyeklar, Z.; Jacobson, R. R.; Karlin, K. D.; Peisach, J. *J. Am. Chem. Soc.* **1993**, *115*, 2093-2102.

(54) Casella, L.; Carugo, O.; Gullotti, M.; Doldi, S.; Frassoni, M. *Inorg. Chem.* **1996**, *35*, 1101-1113.

(55) Beretta, M.; Bouwman, E.; Casella, L.; Douziech, B.; Driessen, W. L.; Gutierrez-Soto, L.; Monzani, E.; Reedijk, J. *Inorg. Chim. Acta* **2000**, *310*, 41-50.

(56) Monzani, E.; Anthony, G. J.; Koolhaas, A.; Spandre, A.; Leggieri, E.; Casella, L.; Gullotti, M.; Nardin, G.; Randaccio, L.; Fontani, M.; Zanello, P.; Reedijk, J. *J. Biol. Inorg. Chem.* **2000**, *5*, 251-261.

(57) Tolman, W. B. *Inorg. Chem.* **1991**, *30*, 4877-4880.

(58) Schneider, J. L.; Carrier, S. M.; Ruggiero, C. E.; Young, J., V. G.; Tolman, W. B. *J. Am. Chem. Soc.* **1998**, *120*, 11408-11418.

(59) Komeda, N.; Nagao, H.; Adachi, G. Y.; Suzuki, M.; Uehara, A.; Tanaka, K. *Chem. Lett.* **1993**, 1521-1524.

(60) Komeda, N.; Nagao, H.; Kushi, Y.; Adachi, G.; Suzuki, M.; Uehara, A.; Tanaka, K. *Bull. Chem. Soc. Jpn.* **1995**, *68*, 581-589.

(61) Lehnert, N.; Cornelissen, U.; Neese, F.; Ono, T.; Noguchi, Y.; Okamoto, K.; Fujisawa, K. *Inorg. Chem.* **2007**, *46*, 3916-3933.

(62) Arnold, P. J.; Davies, S. C.; Durrant, M. C.; Griffiths, D. V.; Hughes, D. L.; Sharpe, P. C. *Inorg. Chim. Acta* **2003**, *348*, 143-149.

(63) Scarpellini, M.; Neves, A.; Castellano, E. E.; Neves, E. F. D.; Franco, D. W. *Polyhedron* **2004**, *23*, 511-518.

(64) Woollard-Shore, J. G.; Holland, J. P.; Jones, M. W.; Dilworth, J. R. *Dalton T.* **2010**, *39*, 1576-1585.

(65) Sarkar, B.; Konar, S.; Gomez-Garcia, C. J.; Ghosh, A. *Inorg. Chem.* **2008**, *47*, 11611-11619.

(66) Maiti, D.; Lee, D. H.; Sarjeant, A. A. N.; Pau, M. Y. M.; Solomon, E. I.; Gaoutchenova, K.; Sundermeyer, J.; Karlin, K. D. *J. Am. Chem. Soc.* **2008**, *130*, 6700-6701.

(67) Lott, A. L. *J. Am. Chem. Soc.* **1971**, *93*, 5313-5314.

(68) Ozarowski, A.; Allmann, R.; Pouribrahim, A.; Reinen, R. *Z. Anorg. Allg. Chem.* **1991**, *592*, 187-201.

(69) Allmann, R.; Kremer, S.; Kucharzcyk, D. *Inorg. Chim. Acta* **1984**, *85*, L19-L21.

(70) Hill, S. J.; Hubberstey, P.; Li, W. S. *Polyhedron* **1997**, *16*, 2447-2453.

(71) Cullen, D. L.; Lingafel.Ec *Inorg. Chem.* **1971**, *10*, 1264-1268.

(72) Klanderman, K. A.; Hamilton, W. C.; Bernal, I. *Inorg. Chim. Acta* **1977**, *23*, 117-129.
(73) Kujime, M.; Fujii, H. *Angew. Chem. Int. Ed.* **2006**, *45*, 1089-1092.
(74) Yokoyama, H.; Yamaguchi, K.; Sugimoto, M.; Suzuki, S. *Eur. J. Inorg. Chem.* **2005**, 1435-1441.
(75) Manchot, W. *Justus Liebigs Ann. Chem.* **1910**, *375*, 308-315.
(76) Kohlschutter, V.; Kutscheroff, M. *Ber. Dtsch. Chem. Ges.* **1904**, *37*, 3044-3052.
(77) Fraser, R. T. M. *J. Inorg. Nucl. Chem.* **1961**, *17*, 265-272.
(78) Fraser, R. T. M.; Dasent, W. E. *J. Am. Chem. Soc.* **1960**, *82*, 348-351.
(79) Tran, D.; Skelton, B. W.; White, A. H.; Laverman, L. E.; Ford, P. C. *Inorg. Chem.* **1998**, *37*, 2505-2511.
(80) Tsuge, K.; DeRosa, F.; Lim, M. D.; Ford, P. C. *J. Am. Chem. Soc.* **2004**, *126*, 6564-6565.
(81) Sarma, M.; Singh, A.; Gupta, G. S.; Das, G.; Mondal, B. *Inorg. Chim. Acta* **2010**, *363*, 63-70.
(82) Sarma, M.; Mondal, B. *Inorg. Chem.* **2011**, *50*, 3206-3212.
(83) Tonzetich, Z. J.; McQuade, L. E.; Lippard, S. J. *Inorg. Chem.* **2010**, *49*, 6338-6348.
(84) Smith, R. C.; Tennyson, A. G.; Lim, M. H.; Lippard, S. J. *Org. Lett.* **2005**, *7*, 3573-3575.
(85) Lim, M. H.; Lippard, S. J. *J. Am. Chem. Soc.* **2005**, *127*, 12170-12171.
(86) Lim, M. H.; Wong, B. A.; Pitcock, W. H.; Mokshagundam, D.; Baik, M. H.; Lippard, S. J. *J. Am. Chem. Soc.* **2006**, *128*, 14364-14373.
(87) Lim, M. H.; Xu, D.; Lippard, S. J. *Nat. Chem. Biol.* **2006**, *2*, 375-380.
(88) Fujisawa, K.; Ono, T.; Ishikawa, Y.; Amir, N.; Miyashita, Y.; Okamoto, K.; Lehnert, N. *Inorg. Chem.* **2006**, *45*, 1698-1713.
(89) Kujime, M.; Kurahashi, T.; Tomura, M.; Fujii, H. *Inorg. Chem.* **2007**, *46*, 541-551.
(90) Bruce, M. I. *J. Organomet. Chem.* **1972**, *44*, 209-226.
(91) Kitajima, N.; Fujisawa, K.; Fujimoto, C.; Morooka, Y.; Hashimoto, S.; Kitagawa, T.; Toriumi, K.; Tatsumi, K.; Nakamura, A. *J. Am. Chem. Soc.* **1992**, *114*, 1277-1291.
(92) Churchill, M. R.; Deboer, B. G.; Rotella, F. J.; Abusalah, O. M.; Bruce, M. I. *Inorg. Chem.* **1975**, *14*, 2051-2056.
(93) Mealli, C.; Arcus, C. S.; Wilkinson, J. L.; Marks, T. J.; Ibers, J. A. *J. Am. Chem. Soc.* **1976**, *98*, 711-718.
(94) Papish, E. T.; Donahue, T. M.; Wells, K. R.; Yap, G. P. A. *Dalton T.* **2008**, 2923-2925.
(95) Kou, X.; Wu, J.; Cundari, T. R.; Dias, H. V. R. *Dalton T.* **2009**, 915-917.
(96) Mairena, M. A.; Urbano, J.; Carbajo, J.; Maraver, J. J. N.; Alvarez, E.; Diaz-Requejo, M. M.; Perez, P. J. *Inorg. Chem.* **2007**, *46*, 7428-7435.
(97) Hocking, R. K.; Hambley, T. W. *Organometallics* **2007**, *26*, 2815-2823.
(98) Fujisawa, K.; Noguchi, Y.; Miyashita, Y.; Okamoto, K. I.; Lehnert, N. *Inorg. Chem.* **2007**, *46*, 10607-10623.

(99) Zhang, H. M.; Boulanger, M. J.; Mauk, A. G.; Murphy, M. E. P. *J. Phys. Chem. B* **2000**, *104*, 10738-10742.

(100) Franz, K. J.; Lippard, S. J. *J. Am. Chem. Soc.* **1998**, *120*, 9034-9040.

(101) Williams, D. L. H. *Acc. Chem. Res.* **1999**, *32*, 869-876.

(102) Ruggiero, C. E.; Carrier, S. M.; Antholine, W. E.; Whittaker, J. W.; Cramer, C. J.; Tolman, W. B. *J. Am. Chem. Soc.* **1993**, *115*, 11285-11298.

(103) Carrier, S. M.; Ruggiero, C. E.; Tolman, W. B. *J. Am. Chem. Soc.* **1992**, *114*, 4407-4408.

(104) Paul, P. P.; Karlin, K. D. *J. Am. Chem. Soc.* **1991**, *113*, 6331-6332.

(105) Paul, P. P.; Tyeklar, Z.; Farooq, A.; Karlin, K. D.; Liu, S. C.; Zubieta, J. *J. Am. Chem. Soc.* **1990**, *112*, 2430-2432.

(106) Park, G. Y.; Deepalatha, S.; Puiu, S. C.; Lee, D. H.; Mondal, B.; Sarjeant, A. A. N.; del Rio, D.; Pau, M. Y. M.; Solomon, E. I.; Karlin, K. D. *J. Biol. Inorg. Chem.* **2009**, *14*, 1301-1311.

(107) Pietrzyk, P.; Piskorz, W.; Sojka, Z.; Broclawik, E. *J. Phys. Chem. B* **2003**, *107*, 6105-6113.

(108) Sundararajan, M.; Surendran, R.; Hillier, I. H. *Chem. Phys. Lett.* **2006**, *418*, 96-99.

(109) Periyasamy, G.; Sundararajan, M.; Hillier, I. H.; Burton, N. A.; McDouall, J. J. W. *Phys. Chem. Chem. Phys.* **2007**, *9*, 2498-2506.

(110) Silaghi-Dumitrescu, R. *J. Inorg. Biochem.* **2006**, *100*, 396-402.

(111) Wasbotten, I. H.; Ghosh, A. *J. Am. Chem. Soc.* **2005**, *127*, 15384-15385.

(112) Usov, O. M.; Sun, Y.; Grigoryants, V. M.; Shapleigh, J. P.; Scholes, C. P. *J. Am. Chem. Soc.* **2006**, *128*, 13102-13111.

(113) Perdew, J. P. *Phys. Rev. B* **1986**, *33*, 8822-8824.

(114) Becke, A. D. *J. Chem. Phys.* **1986**, *84*, 4524-4529.

(115) Schäfer, A.; Horn, H.; Ahlrichs, R. *J. Chem. Phys.* **1992**, *97*, 2571-2577.

(116) Schäfer, A.; Huber, C.; Ahlrichs, R. *J. Chem. Phys.* **1994**, *100*, 5829-5835.

(117) Frisch, M. J.; Trucks, G. W.; Schlegel, H. B.; Scuseria, G. E.; Robb, M. A.; Cheeseman, J. R.; Montgomery, J. A., Jr.; Vreven, T.; Kudin, K. N.; Burant, J. C.; Millam, J. M.; Iyengar, S. S.; Tomasi, J.; Barone, V.; Mennucci, B.; Cossi, M.; Scalmani, G.; Rega, N.; Petersson, G. A.; Nakatsuji, H.; Hada, M.; Ehara, M.; Toyota, K.; Fukuda, R.; Hasegawa, J.; Ishida, M.; Nakajima, T.; Honda, Y.; Kitao, O.; Nakai, H.; Klene, M.; Li, X.; Knox, J. E.; Hratchian, H. P.; Cross, J. B.; Adamo, C.; Jaramillo, J.; Gomperts, R.; Stratmann, R. E.; Yazyev, O.; Austin, A. J.; Cammi, R.; Pomelli, C.; Ochterski, J. W.; Ayala, P. Y.; Morokuma, K.; Voth, G. A.; Salvador, P.; Dannenberg, J. J.; Zakrzewski, V. G.; Dapprich, S.; Daniels, A. D.; Strain, M. C.; Farkas, O.; Malick, D. K.; Rabuck, A. D.; Raghavachari, K.; Foresman, J. B.; Ortiz, J. V.; Cui, Q.; Baboul, A. G.; Clifford, S.; Cioslowski, J.; Stefanov, B. B.; Liu, G.; Liashenko, A.; Piskorz, P.; Komaromi, I.; Martin, R. L.; Fox, D. J.; Keith, T.; Al-Laham, M. A.; Peng, C. Y.; Nanayakkara, A.; Challacombe, M.; Gill, P. M. W.; Johnson, B.; Chen, W.; Wong, M. W.; Gonzalez, C.; Pople, J. A.; Gaussian, Inc.: Pittsburgh, PA, 2003.

(118) Neese, F.; Version 2.2 ed. Max-Planck Institut für Bioanorganische Chemie, Mülheim/Ruhr, Germany, 2004.

(119) Wilmot, C. M.; Hajdu, J.; McPherson, M. J.; Knowles, P. F.; Phillips, S. E. V. *Science* **1999**, *286*, 1724-1728.

(120) Becke, A. D. *Phys. Rev. A* **1988**, *38*, 3098-3100.
(121) Becke, A. D. *J. Chem. Phys.* **1993**, *98*, 1372-1377.
(122) Becke, A. D. *J. Chem. Phys.* **1993**, *98*, 5648-5652.
(123) Fujisawa, K.; Iwamoto, H.; Tobita, K.; Miyashita, Y.; Okamoto, K. *Inorg. Chim. Acta* **2009**, *362*, 4500-4509.
(124) Kitajima, N.; Fujisawa, K.; Morooka, Y. *J. Am. Chem. Soc.* **1990**, *112*, 3210-3212.
(125) Kumar, M.; Merkle, A. C.; Dixon, N. A.; Papish, E. T.; Lehnert, N. **2011**, *In preparation*.
(126) Billing, D. E.; Dudley, R. J.; Hathaway, B. J.; Tomlinso.A *J. Chem. Soc. A* **1971**, 691-696.
(127) Addison, A. W.; Rao, T. N.; Reedijk, J.; Vanrijn, J.; Verschoor, G. C. *J. Chem. Soc. Dalton Trans.* **1984**, 1349-1356.

Chapter 3

The Mechanism of NO Photodissociation in Photolabile Manganese-Nitrosyl Complexes with Pentadentate N5 Ligands

3.1 Introduction

During the past few decades the role of nitric oxide (NO) in several biological functions such as regulation of blood pressure[1] and neurotransmission[2] has been firmly established.[3] These processes require low concentrations (nM) of endogenous NO that is produced from L-arginine by the enzyme nitric oxide synthase (NOS). In addition, macrophages use relatively high concentrations (μM) of NO to fight invading pathogens as part of our innate immune system.[4] Interestingly, studies have shown that exogenous NO can also be used to induce similar biological responses[5-6] as well as other pathological outcomes. For example, it has been shown that high fluxes of NO can lead to apoptosis in malignant cells of different grade and origin.[7-8] This finding has prompted research aimed at developing suitable NO donors for the treatment of cancer.[9-10]

Metal-nitrosyl complexes that release large quantities of NO upon light exposure would be ideal for site specific delivery of NO to malignant locations.[11-12] Such treatment will come under the realm of Photodynamic Therapy (PDT).[13-14] Historically, the bulk of research on photolabile metal-nitrosyl complexes involved iron-[15] and ruthenium-nitrosyl complexes.[16] Studies in this area have indicated that although iron-nitrosyl complexes tend to be more sensitive to low-energy visible light releasing large amounts of NO, the complexes in general tend to be less stable in aqueous environment. Conversely, most ruthenium-nitrosyl complexes are more stable in aqueous media but require UV light for NO release. This trend becomes clear upon comparison of two isoelectronic iron- and ruthenium-nitrosyl complexes, $[Fe(PaPy_3)(NO)](ClO_4)_2$ and $[Ru(PaPy_3)(NO)](BF_4)_2$, ($PaPy_3^-$ = *N*,*N*-bis(2-pyridylmethyl)amine-*N*-ethyl-2-pyridine-2-carboxamide) reported by us previously.[17-18] When exposed to visible light (500–600 nm),

$[Fe(PaPy_3)(NO)](ClO_4)_2$ releases NO with a quantum yield (ϕ) of 0.18[17,19] while $[Ru(PaPy_3)(NO)](BF_4)_2$ requires UV light (300–450 nm) for NO release and exhibits a lower quantum yield ($\phi \sim 0.05$).[18,20] Since UV light is inherently detrimental to cellular targets, we looked into the possibility of the use of other metal-nitrosyl complexes in light-triggered NO release. Interestingly, the manganese-nitrosyl $[Mn(PaPy_3)(NO)](ClO_4)$ (**1**) not only releases NO upon exposure to low-energy, *visible* (500–600 nm) light but also exhibits stability in aqueous media.[21] This sensitivity has been further enhanced to even lower energy light (500–800 nm) by replacing one pyridine ring of the $PaPy_3^-$ ligand frame with a quinoline moiety (*cf.* Scheme 3.1) in the resulting manganese nitrosyl $[Mn(PaPy_2Q)(NO)](ClO_4)$ (**2**, $PaPy_2Q^-$ = *N*,*N*-bis(2-pyridylmethyl)amine-*N*-ethyl-2-quinoline-2-carboxamide).[21]

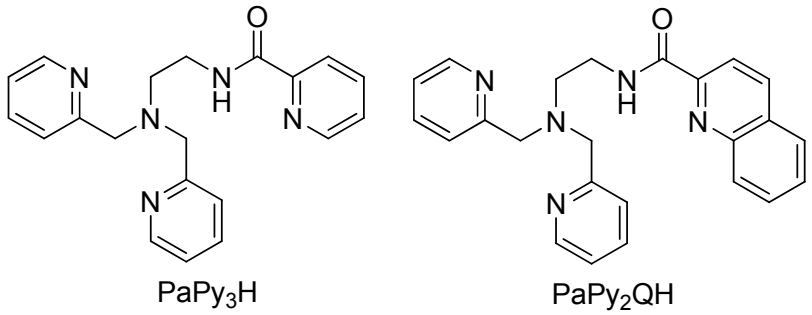

Scheme 3.1 Molecular structure of $PaPy_3H$ and $PaPy_2QH$.

Currently there are relatively few manganese-nitrosyl complexes reported in the literature and even fewer studies that examine their electronic structures in detail. The favorable properties of **1** and **2** have prompted us to further examine their electronic structures in order to gain insights into structure-function relationships leading to NO labilization with *low-energy* light. Such studies are necessary for the smart design of nitrosyls with improved NO donating ability. The non-innocent nature of the NO ligand (possibility of existing as NO^+, $NO^\bullet$ or NO^- in metal-nitrosyl complexes) in general poses a problem in the correct assignment of the formal oxidation states of the metal centers in nitrosyl complexes.[22] Both **1** and **2** are diamagnetic Mn(II) complexes with NO, {Mn–NO} in the Enemark-Feltham notation,[23] and hence there are three possible electronic descriptions: Mn(I)–NO^+, Mn(II)–NO(radical), or Mn(III)-NO^-. In earlier work, researchers have suggested formal oxidation states based on the metric parameters

of the Mn–N–O unit. For example, a low-spin Mn(I)–NO^+ formulation has been suggested for the diamagnetic {Mn-NO}^{6} complexes [Mn(TPP)(NO)] (TPP^{2-} = tetraphenylporphinato dianion)[24] and [Mn-(5-CH_3SALDPT)(NO)] (SALDPT = dianionic pentadentate Schiff base ligand).[25] These complexes have similar NO stretching frequencies (ν(N-O) = 1735 and 1715 cm^{-1}, respectively) compared with those of **1** (1733 cm^{-1}) and **2** (1725 cm^{-1}), indicating similar electronic descriptions. However, more recently, Lippard and Ghosh have used density functional theory (DFT) calculations[26] in addition to magnetic and spectroscopic data to assign the paramagnetic tropocoronand complex, [Mn(NO)(TC-5,5)], as a Mn(III)–NO^- species.[27] Interestingly, the Mn–N–O angle and Mn–N/N–O bond distances of [Mn(NO)(TC-5,5)] (174.1(3)^o, 1.699(3) and 1.179(3) Å, respectively) are very similar to those of [Mn(TPP)(NO)] (174.9(6)^o, 1.644(5) and 1.176(7) Å, respectively). Clearly, the use of metric data alone is not enough to correctly assign the oxidation states of the metal centers in such nitrosyls.

In this study, the spectroscopic properties and the electronic structures of **1** and **2** are investigated using UV-Vis absorption, IR, and resonance Raman spectroscopy coupled to DFT calculations. Raman spectra of the nitrosyl complex **1** are presented for the first time. Using $^{15}N^{18}O$ isotope substitution, the IR and Raman spectra of **1** are assigned, including N-O and Mn-NO stretching and Mn-N-O bending vibrations. Compared to DFT calculations on both singlet and triplet states, such measurements allow for an unambiguous definition of the ground state of these complexes and the formal oxidation states of Mn and NO in **1** and **2**. From these calculations, the electronic structure of both complexes has been defined, and the properties of nitric oxide as a ligand have been evaluated. Finally, details of the photochemistry of **1** and **2** are reported. Time-dependent DFT calculations (TD-DFT) are used to assign the visible absorption spectra of **1** and **2**, and to gain insight into the photophysical mechanisms of NO dissociation in these compounds.

3.2 Experimental and Computational Procedures

3.2.1 Syntheses of Compounds

The ligands *N,N*-bis(2-pyridylmethyl)amine-N-ethyl-2-pyridine-2-carboxamide ($PaPy_3H$) and *N,N*-bis(2-pyridylmethyl)amine-N-ethyl-2-quinoline-carboxamide ($PaPy_2QH$), and the corresponding Mn-nitrosyl complexes, $[Mn(PaPy_3)(NO)]ClO_4$ and $[Mn(PaPy_2Q)(NO)]ClO_4$, respectively, were all synthesized according to literature procedures.[28-29] The starting material, $[Mn(PaPy_3)(H_2O)]ClO_4$, was also synthesized according to previously published methods.[21] Nitric oxide (Cryogenic Gases, Detroit, MI) was purified by first passing through an ascarite II column (NaOH on silica gel) and then through a cold trap at -80 °C to exclude higher nitrogen oxide impurities. Isotopically labeled $^{15}N^{18}O$ was purchased from Sigma-Aldrich and was used as received. All solvents were dried by standard techniques and distilled prior to use. Standard Schlenk techniques were used during all syntheses.

3.2.2 Vibrational Spectroscopy

FT-Raman spectra were recorded on a Bruker IFS 66 interferometer with a Bruker FRA 106 Raman attachment using a Nd:YAG laser for excitation (λ = 1064 nm). Measurements were performed on pure compounds. The resolution was set to 2 cm^{-1}. Mid-infrared (MIR) spectra were obtained from KBr disks on a Perkin-Elmer FT-IR spectrometer SPECTRUM Bx.

The resonance Raman (rRaman) spectra were obtained with solutions of $[Mn(PaPy_3)(NO)]ClO_4$ and the corresponding $^{15}N^{18}O$ labeled complex in CH_3CN using 413, 457, 472, 488, 514, and 647 nm excitation from a SpectraPhysics Beamlok 2060-RS Kr^+/Ar^+ ion gas laser. The excitation beam (10 - 20 mW) was focused onto a ~10.5mM sample in an EPR tube contained in an EPR coldfinger dewar with liquid N_2 to prevent thermal degradation and photolabilization. The scattered photons were dispersed by an Acton two-stage TriVista 555 monochromator and detected by a liquid N_2-cooled Princeton Instruments Spec-10:400B/LN CCD camera. A typical resolution in these experiments was 0.5 cm^{-1}.

3.2.3 DFT Calculations

The structures of $[Mn(PaPy_3)(NO)]^+$ and $[Mn(PaPy_2Q)(NO)]^+$ were fully optimized (for both S = 0, 1 states) without simplifications applying the BP86 functional[30-31] together with Ahlrichs' TZVP basis set.[32-33] The vibrational frequencies of the fully optimized

complexes were again calculated with BP86/TZVP, showing no imaginary frequencies. IR and non-resonance Raman intensities were calculated as well to assist in spectral assignments. All of these calculations were performed using Gaussian 03.[34] To calculate the absorption spectrum of $[Mn(PaPy_3)(NO)]^+$, the time-dependent DFT formalism was applied using both BP86/TZVP and B3LYP/TZVP. Since BP86/TZVP gave an overall better agreement with experiment in the important visible region of the spectrum (see Figure 3.1), this method was used to further assign the UV-Vis absorption spectrum of **1**. TD-DFT calculations were performed using ORCA (University of Bonn).[35] Orbitals were plotted with the program GaussView.

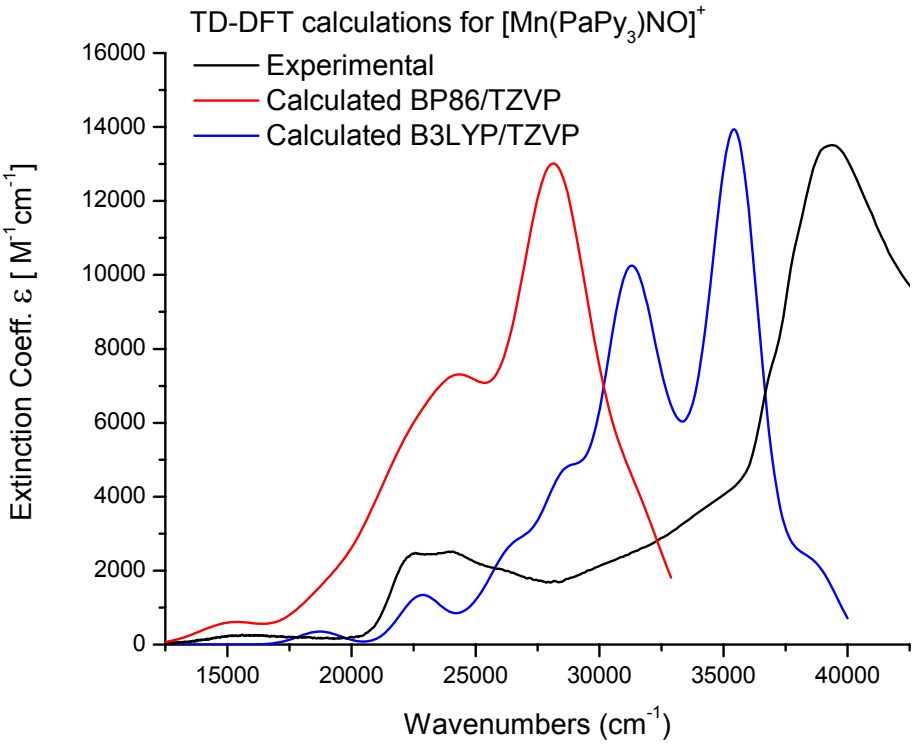

Figure 3.1 TD-DFT calculated absorption spectra of $[Mn(PaPy_3)(NO)]^+$ using B3LYP/TZVP (blue) and BP86/TZVP (red). The BP86/TZVP calculated absorption spectrum is in better agreement in the low energy region with the experimental absorption spectrum (black) taken in MeCN solution at room temperature.

3.3 Results and Analysis

3.3.1 Spectroscopic and Physical Properties

3.3.1.1 Synthesis

Both nitrosyls **1** and **2** were synthesized from their respective water-bound complexes $[Mn(PaPy_3)(H_2O)](ClO_4)$ (**3**) and $[Mn(PaPy_2Q)(H_2O)](ClO_4)$ (**4**). A strong EPR signal with g = 2.00 confirms **3** as a low spin (S = 1/2) Mn(II) species.[21] Conversely, room-temperature EPR measurements indicate that **4** contains a high-spin (S = 5/2) Mn(II) center.[29] Upon exposure to NO gas, the water ligand in **3** and **4** is replaced with NO resulting in the formation of the $\{MnNO\}^6$ nitrosyls **1** and **2**. Room temperature magnetic susceptibility data and sharp resonances in the ^{1}H-NMR spectra of both complexes indicate that these compounds are diamagnetic (S = 0) in the solid state and in solution.

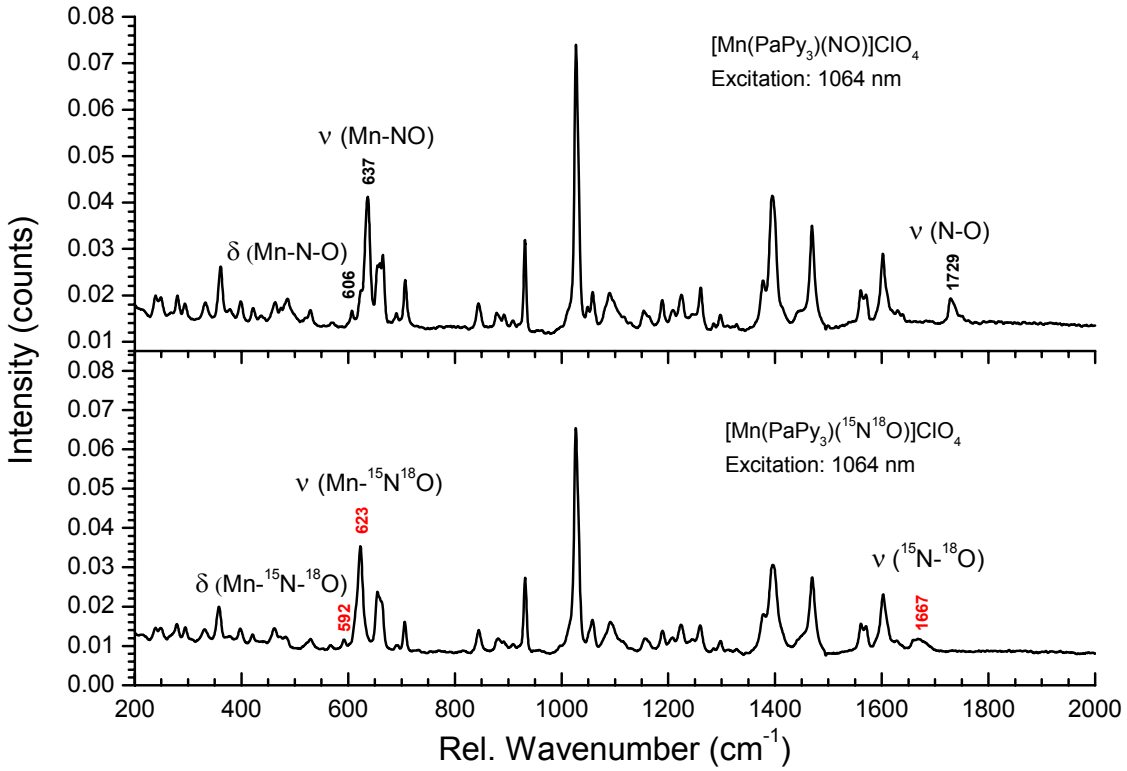

Figure 3.2 FT-Raman spectra of $[Mn(PaPy_3)(NO)]^+$ (top) and $[Mn(PaPy_3)(^{15}N^{18}O)]^+$ (bottom), excited at 1064 nm.

3.3.1.2 Vibrational Properties

The IR spectra of both **1** and **2** contain strong N-O stretching frequencies, ν(N-O), at 1733 cm^{-1} and 1725 cm^{-1}, respectively. Upon $^{15}N^{18}O$ isotope labeling, ν(N-O) of **1** shifts to 1664 cm^{-1}, which confirms this assignment. In order to determine the energies of the Mn-NO stretching and Mn-N-O (linear) bending modes, ν(Mn-NO) and δ(Mn-N-O), Raman spectroscopy was applied. Figure 3.2 shows the non-resonance FT-Raman

spectrum of **1** and of the corresponding $^{15}N^{18}O$ isotope labeled complex. From these data, two isotope-sensitive features are readily identified at 637 cm^{-1} and 606 cm^{-1}, which shift to 623 cm^{-1} and 592 cm^{-1}, respectively, in the $^{15}N^{18}O$ compound (*cf.* Table 3.1). We assign the higher energy feature to the Mn-NO stretch based on three observations. First, the 637 cm^{-1} feature shows significantly higher intensity in the Raman spectrum compared to the 606 cm^{-1} band, which is in agreement with previous assignments of the

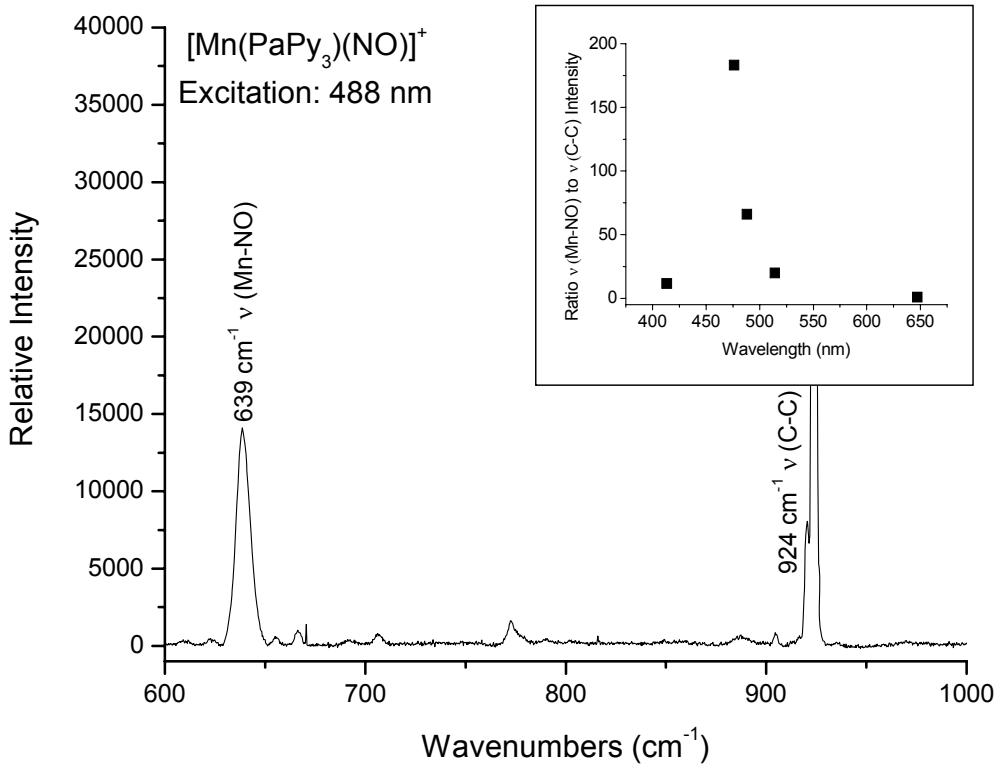

Figure 3.3 Resonance Raman spectrum of $[Mn(PaPy_3)(NO)]^+$ obtained at an excitation wavelength of 488 nm. Insert: resonance Raman excitation profile of the 639 cm^{-1} feature, showing resonance enhancement of this vibration towards the UV region. The ratio of ν(Mn-NO) to ν(C-C) (MeCN) Raman intensity is normalized to the value observed at the excitation wavelength of 647 nm (intensity ratio set to 1).

Ru-NO stretching and Ru-N-O bending modes in $[Ru(NH_3)_5(NO)]X_3$, where the stretch showed considerably more intensity in the FT-Raman spectrum than the bend.[36] Second, the 637 cm^{-1} feature shows resonance enhancement upon laser excitation in the visible region as shown in Figure 3.3 (observed at 639 cm^{-1} in frozen solution), whereas the 606

cm^{-1} feature is not observed under these conditions. Resonance Raman enhancement of metal-ligand vibrations is in most cases related to charge-transfer transitions between the metal and the ligand that lead to a change in the metal-ligand bond in the excited state, and in this way, to an excited state displacement, ΔQ.[37-39] These excited state displacements are generally much more pronounced for metal-ligand bond distances compared to angles, and hence, the metal-ligand stretching, but not bending, modes are in most cases resonance enhanced.[40] The fact that the 637 cm^{-1} mode shows strong resonance enhancement (*cf.* Table 3.2) is therefore indicative that this is in fact the Mn-NO stretch. Finally, our DFT calculations (see below) further support this assignment, as they predict ν(Mn-NO) to be at higher energy than δ(Mn-N-O). These assignments are summarized in Table 3.1. The obtained energy for ν(Mn-NO) also compares well with that reported for Mn-substituted myo- and hemoglobin, observed at ~625 cm^{-1}.[41]

Table 3.1 Experimental and computational vibrational Data of $[Mn(PaPy_3)(NO)]^+$ (**1**) and $[Mn(PaPy_2Q)(NO)]^+$ (**2**).

		1	$^{15}N^{18}O$ labeled: **1**	Difference (N.A.I.-$^{15}N^{18}O$) [b]	**2**
Experimental [cm^{-1}] [a]	ν(N-O)	1733 (IR) 1729 (R)	1664 (IR) 1667 (R)	69 (IR) 60 (R)	1725 (IR)
	ν(Mn-NO)	637 (R) [c]	623 (R)	14	-
	δ(Mn-N-O)	606 (R)	592 (R)	14	-
	ν(C=O)	1630 (IR)	1630 (IR)	0	1634
DFT: BP86/TZVP [cm^{-1}], S = 0	ν(N-O)	1758	1984	74	1737
	ν(Mn-NO)	653	638	15	669
	δ(Mn-N-O)	613/631	620/597	10/15	630/612
	ν(C=O)	1649	1649	0	1641

[a] R = Raman spectroscopy. [b] N.A.I. = natural abundance isotopes complex. [c] observed at 637 cm^{-1} in the solid and at 639 cm^{-1} in frozen solution (*cf.* Figures 3.2 and 3.3, respectively).

3.3.1.3 Electronic Absorption Spectroscopy

The green MeCN solution of **1** exhibits absorption bands with λ_{max} at 22730 (440 nm, ε = 2460 $M^{-1}cm^{-1}$) and 15750 cm^{-1} (635 nm, ε = 220 $M^{-1}cm^{-1}$). The additional conjugation provided by replacement of one pyridine donor with a quinoline moiety in the ligand frame of **2** shifts the position of the absorbance bands to lower energy. For example, the maroon solution of **2** in MeCN displays bands with λ_{max} at 20200 cm^{-1} (495 nm, ε = 2030

$M^{-1}cm^{-1}$) and 15385 cm^{-1} (650 nm, $\varepsilon = 420$ $M^{-1}cm^{-1}$). In addition, the extinction coefficient of the low-energy band of **2** is increased to a significant extent as seen in Figure 3.4. Interestingly, in the case of the corresponding Ru-nitrosyl complexes, $[Ru(PaPy_3)(NO)](BF_4)_2$ and $[Ru(PaPy_2Q)(NO)](BF_4)_2$, there is a much smaller red-shift in λ_{max} (~580 cm^{-1}) upon addition of the quinoline moiety.[18,20]

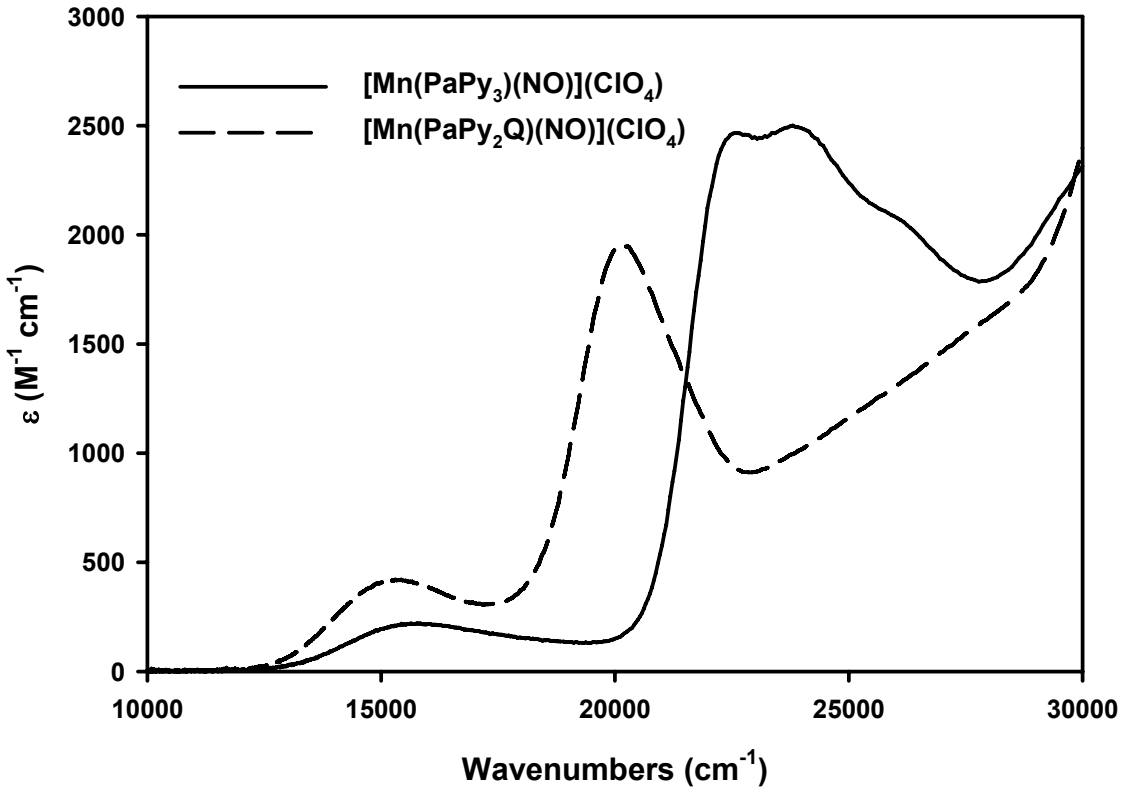

Figure 3.4 Electron absorption spectra of $[Mn(PaPy_3)(NO)]^+$ (solid, black line) and $[Mn(PaPy_2Q)(NO)]^+$ (dashed, black line) obtained in MeCN at room temperature.

3.3.1.4 NO Photolability Measurements.

When solutions of **1** and **2** are exposed to visible light of low intensity (5 mW), rapid loss of NO occurs with concomitant formation of the colorless solvent-bound Mn(II) photoproducts, $[Mn(PaPy_3)(Solv)]^{2+}$ or $[Mn(PaPy_2Q)(Solv)]^{2+}$, respectively. No loss of NO is noted when the solutions are kept in the dark for 48 h. The quantum yield values (ϕ) of **1** and **2** have been determined from changes in the electronic absorption spectra upon exposing the complexes to light of two different wavelengths (500 and 550 nm) in MeCN. The ϕ value of **2** (0.623 ± 0.010 and 0.579 ± 0.010 at 500 and 550 nm,

respectively) are significantly larger than the values of **1** (0.326 ± 0.010 and 0.309 ± 0.010, respectively). This indicates that incorporation of a quinoline moiety in place of the pyridine group is not only effective in moving the photosensitivity to light of longer wavelengths, but also in improving ϕ values of the resulting Mn-nitrosyl. The latter effect, i.e. the approximate doubling of ϕ in complex **2** relative to **1** upon excitation at 500 and 550 nm indicates that **2** has more efficient interconversion channels of the initially excited CT states into the key NO photoreleasing triplet excited states (see Discussion) than **1** (since ϕ is normalized to the extinction of the sample). Additional photophysical studies published previously[42] show that complex **2** photolabilizes NO even upon excitation with NIR light (up to 800 nm), which demonstrates that **2** is a superior NO donor compared to **1** for potential applications *in vivo*.

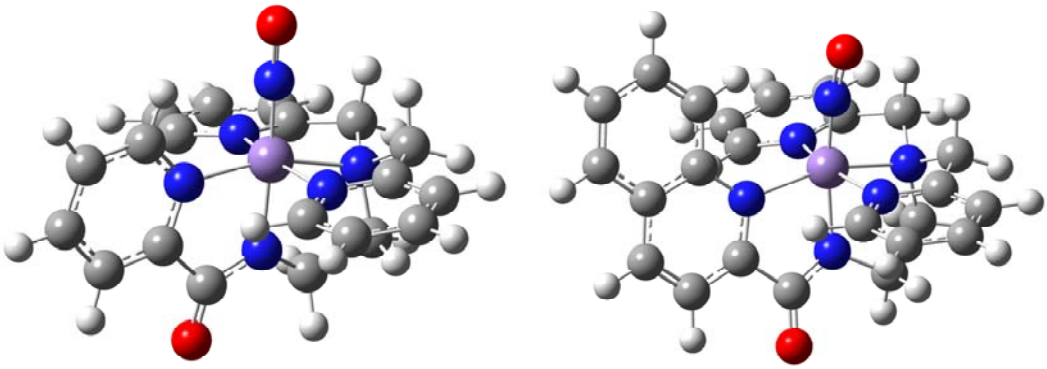

Figure 3.5 Fully optimized structures of $[Mn(PaPy_3)(NO)]^+$ (left) and $[Mn(PaPy_2Q)(NO)]^+$ (right) for S = 0, obtained with BP86/TZVP. Structural data are given in Table 3.3.

Table 3.2 Structural Data of $[Mn(PaPy_3)(NO)]^+$ and $[Mn(PaPy_2Q)(NO)]^+$ from X-ray Crystallography[21,29] and DFT Calculations (BP86/TZVP).

	$[Mn(PaPy_3)(NO)]^+$		$[Mn(PaPy_2Q)(NO)]^+$	
	Crystal Structure	DFT Calculation (S= 0)	Crystal Structure	DFT Calculation (S = 0)
Mn-NO [Å]	1.66	1.67	1.68	1.67
N-O [Å]	1.19	1.18	1.21	1.19
Mn-N-O [deg]	172°	180°	165°	169°
Mn-N_{amide} [Å]	1.96	1.96	1.96	1.96
Mn-N_{amine} [Å]	2.03	2.06	2.06	2.06
Mn-$N_{py(trans\ amide)}$ [Å]	2.00	2.00	2.09	2.06
Mn-$N_{py(trans\ py)}$ [Å]	2.03, 2.02	2.05, 2.05	2.06, 2.03	2.04, 2.05

3.3.2 Electronic Structure of the Manganese(II) Complexes with NO

In order to further investigate the electronic structures of **1** and **2**, and to explain the apparent strength of the Mn-NO bond in these complexes, we applied DFT calculations using the BP86/TZVP functional/basis set combination that has proven to deliver good structures for transition-metal nitrosyls in the past.[22,43-50] The structures of the two complexes $[Mn(PaPy_3)(NO)]^+$ and $[Mn(PaPy_2Q)(NO)]^+$ were optimized without simplifications for both S = 0 and S = 1 as potential ground states. Figure 3.5 shows the obtained structures for the S = 0 cases, and calculated geometric parameters are compared to experiment in Table 3.3. As can be seen from these data, excellent agreement is obtained between the experimental and DFT-calculated structures for the S = 0 state. The predicted vibrational data for the S = 0 and S = 1 states are listed in Table 3.4. The calculated vibrational frequencies provide further support for the idea that both **1** and **2** have diamagnetic (S = 0) ground states. Interestingly, the N-O stretching frequency is quite insensitive to this change in spin state, and is predicted, for example, at 1758 versus 1761 cm^{-1} in the singlet and triplet state of **1**, respectively. In contrast, the Mn-NO stretch and the Mn-N-O bend are very sensitive to the difference in spin state, and are predicted to shift about 70-80 cm^{-1} to lower frequency in the triplet state as shown in Table 3.4. Based on this comparison, it can be safely concluded that both **1** and **2** have diamagnetic (S = 0) ground states. The predicted energy difference between the S = 0 and S = 1 states of **1** and **2** is 16 and 14 kcal/mol, respectively, again favoring the ground state to be S = 0.

Table 3.3 Comparison of Key calculated vibrational Data (BP86/TZVP) between the potential S = 0 and S = 1 Ground States of $[Mn(PaPy_3)(NO)]^+$ and $[Mn(PaPy_2Q)(NO)]^+$.

Complex	Vibrations	Singlet: S = 0	Triplet: S = 1	Experimental
$[Mn(PaPy_3)(NO)]^+$	ν(N-O) ν(Mn-NO) δ(Mn-N-O)	1758 cm^{-1} 653 cm^{-1} 613 / 631 cm^{-1}	1761 cm^{-1} 582 cm^{-1} 520 / 550 cm^{-1}	1733 cm^{-1} 637 cm^{-1} 606 cm^{-1}
$[Mn(PaPy_2Q)(NO)]^+$	ν(N-O) ν(Mn-NO) δ(Mn-N-O)	1737 cm^{-1} 669 cm^{-1} 612 / 630 cm^{-1}	1746 cm^{-1} 590 cm^{-1} 525 / 551 cm^{-1}	1725 cm^{-1}

Based on the exceptional agreement between the optimized and experimental structures of **1** and **2**, we then used the optimized structure of **1** to further characterize the electronic structures of these manganese-nitrosyl complexes in their S = 0 ground states.

Figure 3.6 shows the calculated MO diagram of $[Mn(PaPy_3)(NO)]^+$. In this complex, the Mn(II) ion is in the low-spin state, which would lead to a $[t_{2g}]^5$ electron configuration. However, the additional (unpaired) electron of NO is used to fill the remaining hole in the t_{2g} shell, leading to a formally Mn(I) center with a $[t_{2g}]^6$ electron configuration, and a bound NO^+ ligand. Hence, the ground state is represented by a closed-shell electron configuration, S = 0, where all electrons are perfectly paired. As shown in Figure 3.6, the highest occupied molecular orbital (HOMO) of **1** is the d_{xy} orbital (MO<110>), which is non-bonding with respect to the NO^+ ligand. Here, we apply a coordinate system where the Mn-N(O) bond corresponds to the z axis. An iso-density surface plot of MO<110>, corresponding to the d_{xy} orbital of Mn, is shown in Figure 3.7. Note that simplified ChemDraw representations of important MOs are also included in Figure 3.6, right, to further illustrate the properties of these orbitals with respect to metal-ligand interactions. To lower energy, two $PaPy_3^-$ ligand-based orbitals are found, MO<109> and MO<108>, followed by the two bonding combinations between the π* orbitals of the formally NO^+ unit and the d_{xz} and d_{yz} orbitals of the metal, labeled d_{xz}_π_x* (MO<107>) and d_{yz}_π_y* (MO<106>). The corresponding antibonding combination**,** π_x*_d_{xz} (MO<113>) and

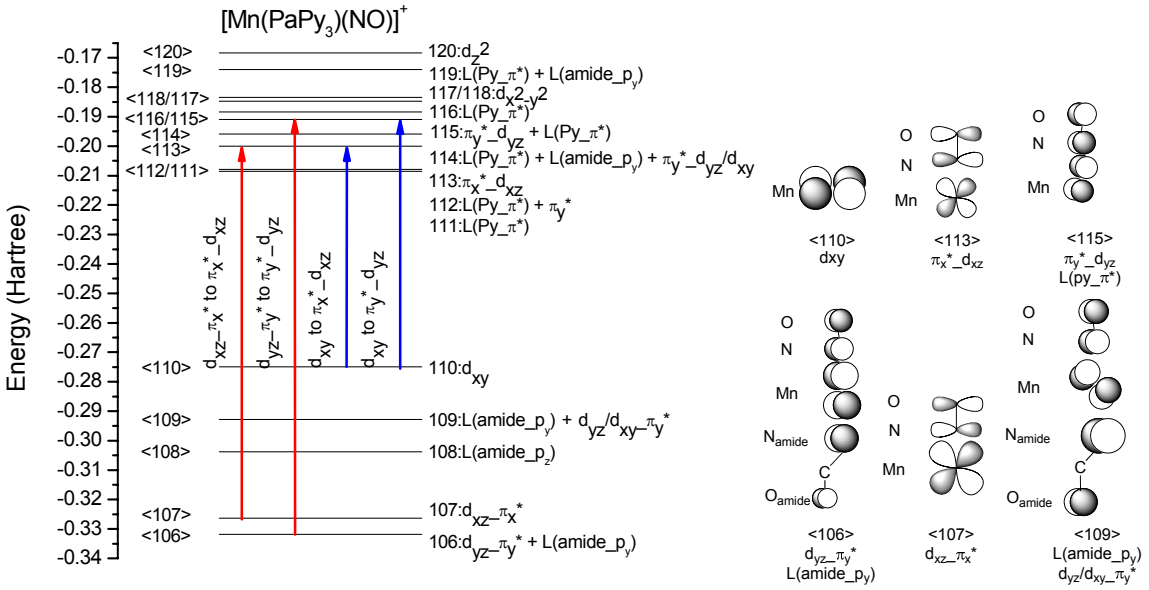

Figure 3.6 The MO diagram of [Mn(PaPy3)(NO)]+ (S = 0) calculated with BP86/TZVP. In the applied coordinate system, the z axis points along the Mn-N(O) bond. The nomenclature '*a*_*b*' indicates that orbital *a* interacts with *b* and that *a* has a larger contribution to the resulting MO. Contour plots of important molecular orbitals are provided in Figure 3.7. Symmetry-allowed (red arrows) and -forbidden (blue arrows) MLCT transitions are indicated (see text). On the right, ChemDraw representations of key MOs are included.

Table 3.4 Selected electronic Transitions in $[Mn(PaPy_3)(NO)]^+$ (**1**) calculated with TD-DFT (BP86/TZVP), and Analysis of underlying One-Electron Transitions.

Band	TD-DFT States	Energy [cm^{-1}]	Energy [nm]	f(osc)	Major Contribution [a]	Percent Contribution
1	S4	14663	682	0.002	d_{xy} to L(Py_π*)	49%
1	S6	15368	651	0.006	d_{xy} to L(Py_π*)	42%
2	S13	18716	534	0.006	d_{yz}/d_{xy}_π_y* to L(Py_π*) L(amide_p_y) to L(Py_π*)	45%
2	S15	18881	530	0.006	d_{xy} to L(Py_π*)	31%
3	S31	21945	456	0.031	d_{xy} to L(Py_π*)	30%
4	S38	23315	429	0.012	d_{xy} to L(Py_π*)	23%
4	S42	24059	416	0.017	d_{yz}/d_{xy}_π_y* to L(Py_π*)	36%
4	S46	24731	404	0.047	**d_{yz}/d_{xy}_π_y* to π_y*_d_{yz}**	18%
4	S47	25076	399	0.007	**d_{yz}/d_{xy}_π_y* to π_y*_d_{yz}**	41%
5	S63	27269	367	0.042	L(Py_π) to L(Py_π*) d_{yz}/d_{xy}_π_y* to L(Py_π*)	37%
5	S67	28165	355	0.026	L(amide_p_y) to L(Py_ π*) d_{yz}/d_{xy}_π_y* to d_{z^2}	24%
					d_{yz}_π_y* to L(Py_π*)	11%
5	S68	28210	355	0.086	d_{yz}_π_y* to L(Py_π*)	32%
6	S80	30759	325	0.016	d_{yz}_π_y* to L(Py_π*) **d_{yz}_π_y* to π_y*_d_{yz}/d_{xy}**	25%
6	S86	31514	317	0.019	L(amide_p_z) to d_{z^2}	17%
					d_{yz}_π_y* to π_y*_d_{yz}	16%
6	S87	31804	314	0.010	d_{yz}_π_y* to L(Py_π*)	42%

[a] Py_π* = pyridine π* orbitals; amide_p_n = amide nitrogen p_y or p_z orbitals

π_y*_d_{yz} (MO<115>), are unoccupied and found to slightly higher energy than the lowest unoccupied molecular orbital (LUMO) of the complex. Iso-density surface plots of all of these key orbitals are shown in Figure 3.7, and Figure 3.6 includes simplified ChemDraw representations of these MOs. The LUMO and LUMO+1 of **1** are $PaPy_3^-$ ligand-based MOs, centered on the pyridine rings (MOs<111/112>; *cf.* Figure 3.6). As shown in Figure 3.7, the d_{yz}_π_y* bonding combination also shows strong admixture of the p_y donor orbital of the amide nitrogen atom of $PaPy_3^-$, trans to NO, which is located at similar energy as the t_{2g} orbitals of manganese. Figure 3.6 shows ChemDraw representations that better illustrate this interaction. The main component of this amide orbital is observed in MO<109> (*cf.* Figure 3.7), which has 55% amide character. On the other hand, the

π_y*_d_{yz} antibonding combination is mixed with pyridine π* orbitals (see MO<115> in Figure 3.7). Because of this complication, the strength of the Mn(I)-NO^+ π-backbond is best estimated from the d_{xz}/π_x* set: here, the occupied MO, d_{xz}_π_x* (MO<107>), has 54% Mn and 36% NO^+ character, whereas the antibonding combination, π_x*_d_{xz} (MO<113>), has 54% NO^+ and 37% Mn contributions (see also the simplified drawings of these MO's in Figure 3.6). The fact that the occupied MO has more metal character is again in agreement with the idea that these electrons should formally be assigned to manganese, in accordance with the Mn(I)-NO^+ description. Nevertheless, these charge contributions correspond to an extraordinarily strong π-backbond, due to the soft nature of the formally Mn(I) center. Hence, *via* covalency (orbital mixing), the charge density of about 1.3 electrons is transferred back from the Mn(I) center to NO^+. Since the transferred charge density has 50% α and 50% β spin, this does *not* correspond to an electron transfer, because an electron has a charge *and* a corresponding spin. This is purely an effect of metal-ligand covalency. Finally, the σ bond between Mn(I) and NO^+ is weak: as shown in Figure 3.6, the corresponding antibonding combination between d_{z^2} and the σ-donor orbital of NO^+, MO<120>, only has 7% NO character. Therefore, the Mn(I)-NO^+ interaction in **1** is dominated by π-backbonding.

The electronic structure of the optimized triplet complex mentioned above corresponds to a [$d_{xz}^2 d_{yz}^2 d_{xy}^1 d_{x2-y2}^1$] electron configuration, i.e. a $d_{xy} \rightarrow d_{x2-y2}$ ligand field (excited) triplet state relative to the singlet ground state. Here, the triplet electron configuration leads to a strong spin polarization of the Mn-NO backbond. In fact, the complex adopts an electronic structure that is now better described as Mn(III)-NO^-. In the case of the α-MOs, the Mn-NO backbond is greatly weakened compared to the singlet ground state, whereas in the β-MO case, an inverted bonding scheme is observed where the occupied orbitals of the Mn-NO π bond now have more dominant π*(NO) character. Hence, NO can be considered as NO^- (S = 1) ligand where both β-π* orbitals of NO are singly occupied and strongly donate into the β-d_{xz} and β-d_{yz} orbitals of Mn (in the coordinate system applied here). This situation is similar to ferrous non-heme iron-

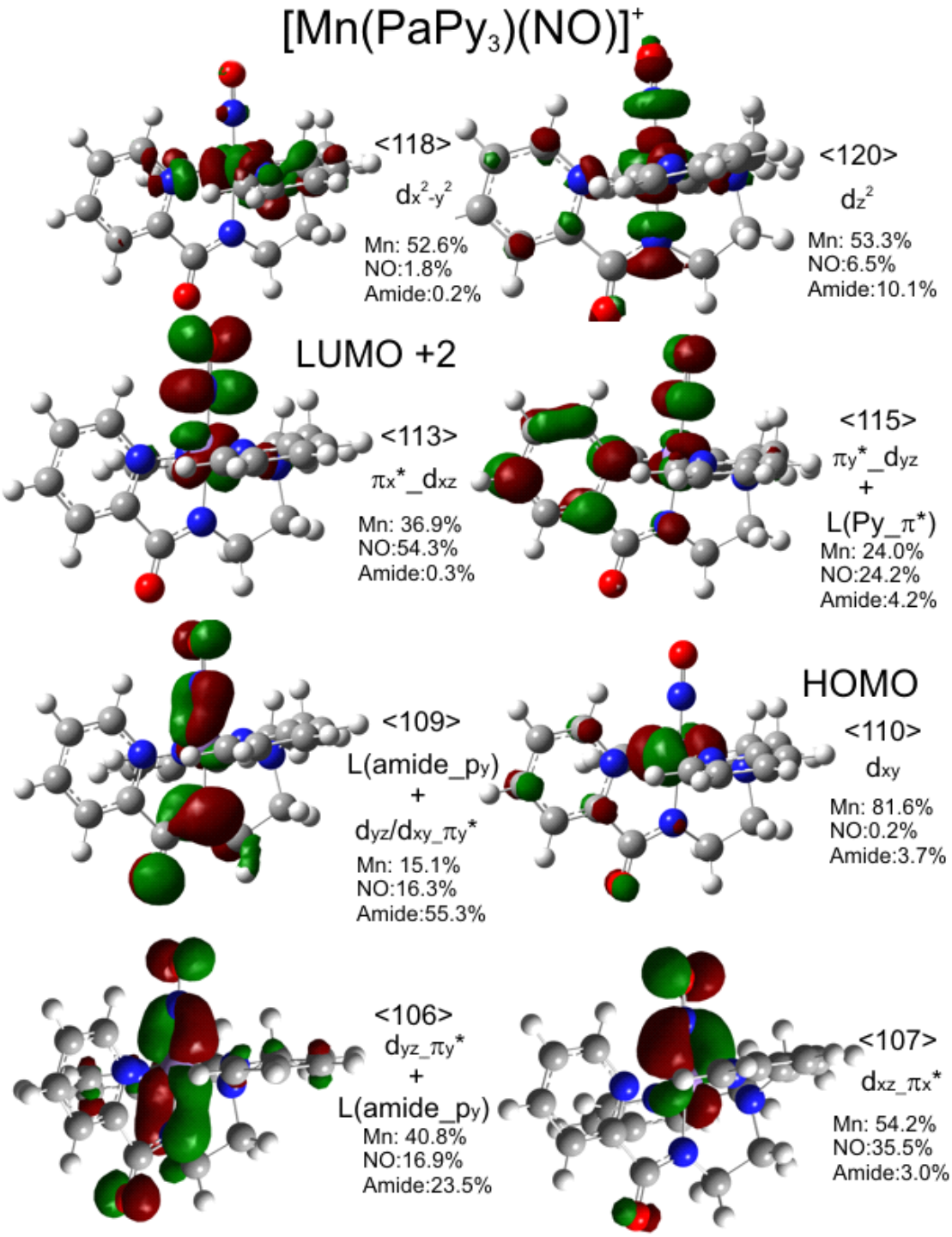

Figure 3.7 Iso-density surface plots of important molecular orbitals of $[Mn(PaPy_3)(NO)]^+$, calculated with BP86/TZVP. Orbital energies increase from bottom to top. Percent compositions of these MOs are included.

nitrosyl complexes.[51] This leads to a less covalent, weaker Mn-NO bond compared to the singlet ground state, which explains the predicted reduction of the Mn-NO stretching frequency from 653 (for S = 0) to 582 cm^{-1} (for S = 1) in the calculation for **1**. Collectively, these theoretical results along with the resonance Raman data strongly suggest that the Mn(III)-NO^- description is not appropriate for the present set of manganese-nitrosyl complexes.

Table 3.5 Fit of the UV-Vis Absorption Spectrum of $[Mn(PaPy_3)(NO)]^+$ (**1**).

Band	Position [cm^{-1}] (nm)	ε-coeff [$M^{-1}cm^{-1}$]	Assignment
A	15641 (639)	323	d_{xy} to L(Py_π*)
B	18626 (537)	190	
C	20569 (486)	170	
D	22142 (452)	2099	d_{xy} to L(Py_π*)
E	23632 (423)	2370	t_{2g} to L(Py_π*) **d_{yz}/d_{xy}_π_y* to π_y*_d_{yz}**
F	26014 (384)	2393	t_{2g} to L(Py_π*) **d_{yz}/d_{xy}_π_y* to π_y*_d_{yz}**
G	30184 (331)	2566	t_{2g} to L(Py_π*) L(Py_π) to L(Py_π*) **d_{yz}_π_y* to π_y*_d_{yz}**
H	33118 (302)	2488	
I	35838 (279)	4190	
J	39289 (255)	17891	

The MO diagram of $[Mn(PaPy_2Q)(NO)]^+$ (not shown) in the singlet ground state is overall similar to $[Mn(PaPy_3)(NO)]^+$, but more complex due to the additional ligand orbitals present in the HOMO-LUMO region that originate from the quinoline (Q) group. The small differences between **1** and **2** in terms of electronic structure are directly reflected by the calculated vibrational frequencies, where **1** has a higher ν(N-O) and lower ν(Mn-NO) frequency compared to **2** (*cf.* Table 3.4). This inverse correlation of the N-O and metal-NO stretching frequencies between **1** and **2** directly indicates that complex **2** has a *slightly* stronger Mn(I)-NO^+ π-backbond.[52] Here, an increased donation from the d_π orbitals of the metal into π* of NO^+ leads to a weaker N-O bond (lower ν(N-O) frequency) and stronger Mn-NO bond (higher ν(Mn-NO) frequency) in **2**.

3.3.3 TD-DFT Calculations and Spectral Assignments

TD-DFT calculations were used to explore the nature of the lowest-lying excited states in **1** and **2** in order to assign their electronic spectra and to determine why these complexes can be photoactivated using visible light. BP86/TZVP was used for the TD-DFT

calculations to predict the 90 lowest-lying excited states of $[Mn(PaPy_3(NO)]^+$ and $[Mn(PaPy_2Q)(NO)]^+$. Both of these complexes show overall similar results, so $[Mn(PaPy_3)(NO)]^+$ is discussed in the following. At this point the reader should be reminded that TD-DFT is generally not able to describe CT excited states well, and correspondingly, one has to be cautious when evaluating TD-DFT results. We therefore limit our analysis to a semi-quantitative interpretation that is focused on the relative energies and intensities of different types of electronic transitions, but not so much on absolute values.

Table 3.5 lists selected TD-DFT calculated singlet excited states (oscillator strength, f(osc) > 0.006) for $[Mn(PaPy_3)(NO)]^+$. The absorption spectrum of complex **1** together with a Gaussian deconvolution of the experimental spectrum (bands A–J) is shown in Figure 3.8 (*cf.* Table 3.6), in comparison to the TD-DFT results. The main features in the calculated spectrum, labeled bands 1–6, are assigned as listed in Table 3.5. Based on the overall excellent agreement between the experiment and the calculations below 25000 cm^{-1}, the visible absorption spectrum of **1** can be assigned (*cf.* Table 3.6). The experimental bands A–C at 15641, 18626, and 20569 cm^{-1}, respectively, are associated with calculated bands 1 and 2 and are assigned to d_{xy} to pyridine (π^*) metal-to-ligand (ML) CT transitions, $d_{xy} \rightarrow L(Py\_\pi^*)$, of the $PaPy_3^-$ ligand. The intense bands D, E, and F at higher energy between 22000 – 26000 cm^{-1} correspond to the calculated features 3 and 4, which have again $t_{2g} \rightarrow L(Py\_\pi^*)$ character, but also show symmetry-allowed $d_\pi\_\pi^*(NO) \rightarrow \pi^*(NO)\_d_\pi$ MLCT contributions (corresponding to the transitions between MOs <109> → <115>; *cf.* Figure 3.7). Here, MO<109> corresponds to the antibonding combination between the $d_{yz}\_\pi_y^*$ orbital and the amide π-donor orbital of the $PaPy_3^-$ ligand. Above 25000 cm^{-1}, the deviation between the experimental and the calculated UV-Vis spectrum becomes quite pronounced. The intense, calculated feature 5, which is mostly of metal(d) → L(Py_π^*) MLCT and inner ligand ($PaPy_3^-$) character (*cf.* Table 3.5), has no equivalent feature at similar energy in the experimental data, and likely contributes to the intense features G and H. Finally, a main contribution to the symmetry-allowed $d_\pi\_\pi^* \rightarrow \pi^*\_d_\pi$ CT transition (corresponding to the transition between MOs <106> → <115>; *cf.* Figure 3.7) is calculated at about 31000 cm^{-1} (~325 nm), which is in fact quite similar to the analogous Ru(III) complex with NO (see Figure

3.9), in addition to other Ru(III)-nitrosyl complexes including $(NEt_4)_2[Ru(hybeb)(NO)]$.[53] In the case of **2**, stronger low-energy absorptions at 674 nm and 540 nm are observed, which are assigned to additional d_{xy} → L(Py/Q_π*) transitions, based on the presence of the Q group in the coligand that has a more extended π system than Py.

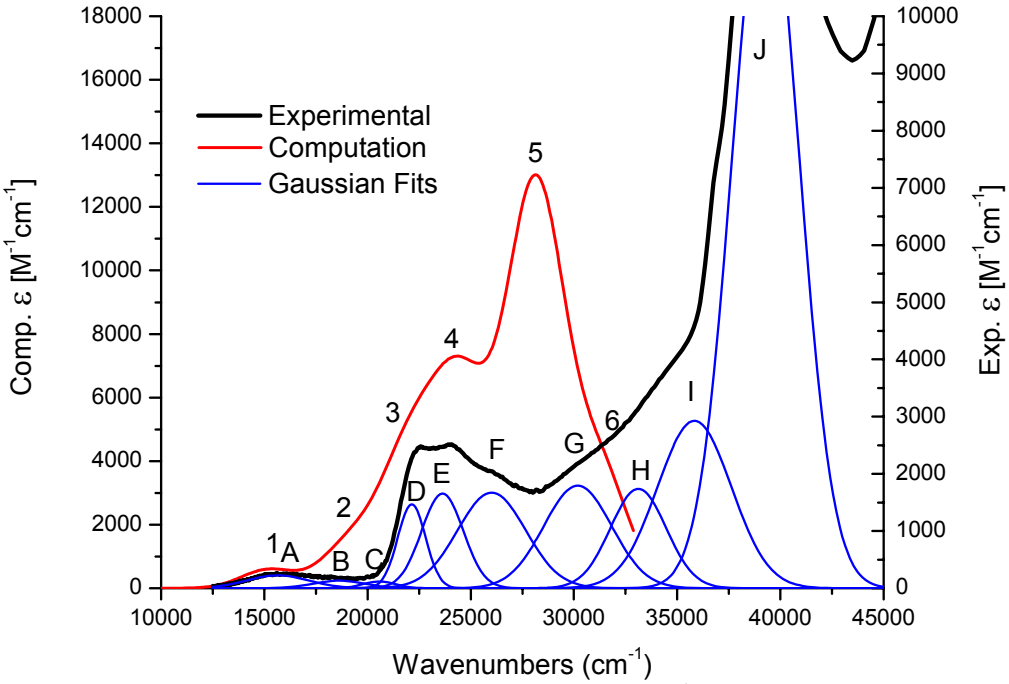

Figure 3.8 Experimental absorption spectrum of $[Mn(PaPy_3)(NO)]^+$ taken in MeCN solution at room temperature (black line, right vertical axis), including a Gaussian fit of the experimental data (blue lines). The resulting features A - J are listed in Table 3.7. The TD-DFT calculated spectrum (red line, left vertical axis) has six main features, labeled 1 – 6, as defined in Table 3.6. The calculated spectrum is cut off at about 32000 cm^{-1} since only 90 excited states were calculated.

Previously, it has been speculated that the photolability of ruthenium(III) complexes with NO arises from symmetry-allowed d_π_π* → π*_d_π CT transitions between the corresponding metal-NO bonding and antibonding MOs (red arrows in Figure 3.6).[54] Our results now show that the corresponding excited states for **1** and **2** are in fact located in the UV region, similar to $[Ru(PaPy_3)(NO)]^{2+}$ and, therefore, the Mn-nitrosyl complexes should be similar to the analogous Ru complexes and show photolabilization mostly in the UV range. The fact that some photolabilization of NO in complexes **1** and **2** is observed upon excitation in the 400 – 450 nm region (*cf.* Table 3.2) can then be explained with the admixture of some d_π_π* → π*_d_π CT character into the metal(d) → L(Py_π*) CT transitions that dominate this spectral region. This is different from

$[Ru(PaPy_3)(NO)]^{2+}$, where no such admixture of $d_\pi \rightarrow \pi^*(NO)$ CT character into the metal(d) → L(Py_π*) CT transitions is observed in the visible region. However, these results can still not explain why the NO ligand in complexes **1** and **2** can be photolabilized with excitation wavelengths as low as 600 nm (**1**) and even 800 nm (**2**), where only $d_{xy} \rightarrow$ L(Py/Q_π*) transitions are observed. The photolabilization of NO at these low excitation energies must therefore be caused by other mechanisms than direct excitation of the d_π_π* → π*_d_π transitions. This aspect is further evaluated in the Discussion.

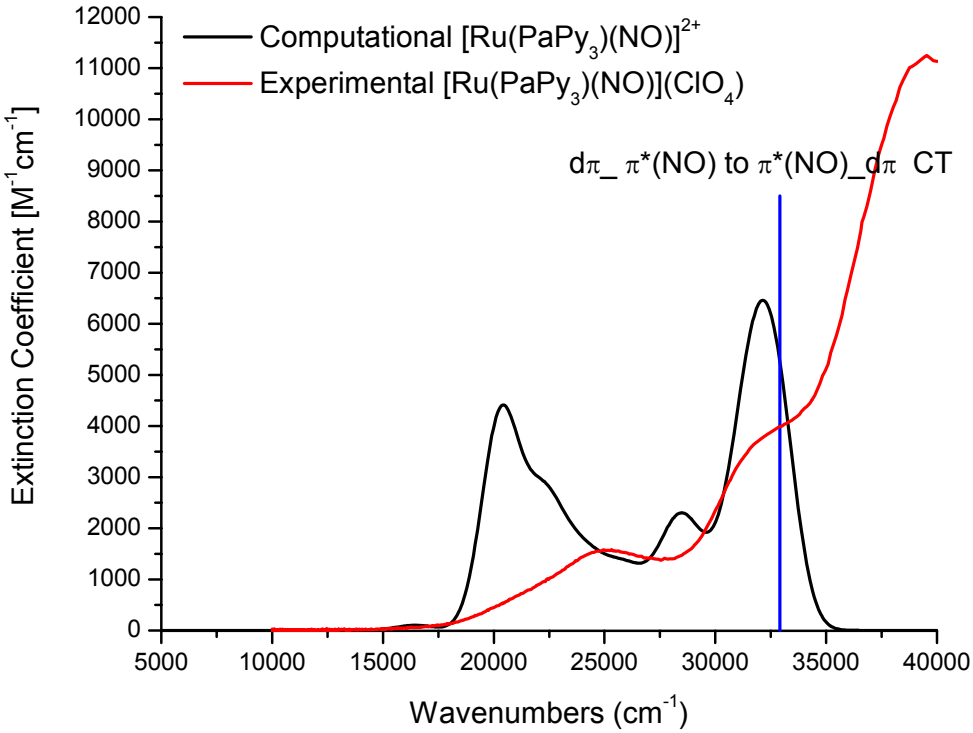

Figure 3.9 TD-DFT (BP86/TZVP) calculated spectrum of $[Ru(PaPy_3)(NO)]^{2+}$ (black line). The main d_π_π*(NO) → π*(NO)_d_π CT transition is predicted at ~300 nm (~33000 cm^{-1}; blue line).

3.4 Discussion

In this paper, the spectroscopic properties and electronic structures of two analogous Mn(II) complexes with NO, $[Mn(PaPy_3)(NO)]^+$ (**1**) and $[Mn(PaPy_2Q)(NO)]^+$ (**2**), are analyzed, and based on the results, the nature of the Mn-NO bond in these complexes is characterized in detail. In addition, reasons for the photolability of the NO ligand upon Vis-NIR excitation of these complexes are explored. Both **1** and **2** show similar geometric structures with short Mn-NO bond distances of 1.66 – 1.68 Å and close to

linear Mn-N-O units. Vibrational spectroscopy further confirms the similarity in the properties of the Mn-NO units in these complexes, showing the diagnostic N-O stretch at 1733 and 1725 cm^{-1} (from IR) in **1** and **2**, respectively. Using Raman spectroscopy, we were able to identify the Mn-NO stretch in **1** at 637 cm^{-1}, which shifts to 623 cm^{-1} upon $^{15}N^{18}O$ labeling. These vibrational data provide key insight into the properties of the Mn-NO bond in these complexes. The observed ν(N-O) values fall within the range of other diamagnetic manganese-nitrosyl complexes (1700-1775 cm^{-1}; see Introduction),[24-25,55-56] but they are quite different from the N-O stretch in the paramagnetic [Mn(NO)(TC-5,5)] complex (1662 cm^{-1}).[18] This indicates that **1** and **2** have similar electronic structures as the other diamagnetic Mn(II)-nitrosyl complexes, for example [Mn(TPP)(NO)], which have previously been described as Mn(I)-NO^+. In addition, the Mn-NO frequency of 637 cm^{-1} is one of the highest transition-metal NO stretching frequencies reported to date, which even supersede ν(Fe-NO) in ferric heme-nitrosyl complexes (580 – 590 cm^{-1})[22,49] and ν(Ru-NO) in ruthenium(III) complexes with NO (~600 cm^{-1}).[36] This shows that the Mn-NO bond is very strong in the ground state of complexes **1** (and **2**), and hence the Mn-NO bond is likely very stable thermodynamically in these complexes (although there can be exceptions to this extrapolation due to low-lying excited states, see ref. 49). DFT calculations are able to reproduce these geometric and spectroscopic properties well in the diamagnetic (S = 0) state of the complexes, whereas in the alternative triplet ground state, a distinct weakening of the Mn-NO bond is observed. This result along with the NMR data of the complexes clearly show that **1** and **2** indeed have diamagnetic (S = 0) ground states. The electronic structure of the complexes is best described as Mn(I)-NO^+, where Mn(I) is in the diamagnetic $[t_{2g}]^6$ low-spin state, and the NO^+ ligand forms two very strong π-backbonds with the d_{xz} and d_{yz} orbitals of the metal (where the Mn-N(O) bond corresponds to the z axis). This explains the strong Mn-NO bonds observed in these complexes as reflected by their high Mn-NO stretching frequencies.

Importantly, the Mn(II) complexes with NO in their Mn(I)-NO^+ type ground states are isoelectronic to ferric heme-nitrosyl complexes and Ru(III) complexes with NO, which can be best described as having the analogous Fe(II)/Ru(II)-NO^+ ground state electronic structures.[3,23,36,49,57-61] Note that all these compounds fall within the $\{M\text{-}NO\}^6$ category according to the Enemark-Feltham notation.[23] These iron- and ruthenium-

nitrosyl complexes exhibit similar, short Fe/Ru-NO bond distances (~1.65 Å in the iron case),[3,62] linear Fe/Ru-N-O units as observed for **1** and **2**, and Fe/Ru-NO and N-O stretching frequencies in the 580 – 600 and ~1900 cm^{-1} range, respectively.[16,22,49,52,63] In the case of $[Fe(PaPy_3)(NO)]^{2+}$ and $[Ru(PaPy_3)(NO)]^{2+}$, the N-O stretch is observed at 1919 and 1899 cm^{-1}, respectively.[17-18] Therefore, relative to these analogous nitrosyls, complexes **1** and **2** exhibit *higher* metal-NO and *lower* N-O stretching frequencies as reported in this paper. This indirect correlation indicates a stronger π-backbond in complexes **1** and **2** compared to the isoelectronic iron- and ruthenium-nitrosyl complexes. This is further confirmed by our DFT calculations, which show a distinct increase in the orbital mixing between the d_{xz}/d_{yz} (d_π) orbitals of the metal and the π* orbitals of NO. For example, the corresponding antibonding combination, $d_{xz}\_\pi^*_x$, in complex **1** has 54% π* and 37% Mn character, compared to ~70% π* and ~25% metal contributions in the Fe/Ru-nitrosyl complexes.[36,49] Therefore, the softer Mn(I) center forms the stronger π-backbond with the π* orbitals of NO^+ compared to the harder Fe(II) and Ru(II) centers, which explains the higher metal-NO and lower N-O stretching frequency in the manganese case; complexes **1** and **2** in fact have one of the strongest metal-NO^+ π-backbonds reported so far.

The Mn(I)-NO^+ electronic structure description implies that one-electron oxidation of complexes **1** and **2** should be metal centered, resulting in a Mn(II)-NO^+ species, since oxidation of the NO^+ ligand seems unlikely. In fact, complex **1** can be oxidized chemically (and electrochemically), and the resulting compound, $\mathbf{1^{ox}}$, exhibits an N-O stretching frequency of 1875 cm^{-1}, which is much higher than that of **1** (1733 cm^{-1}). Interestingly, this number is very close to ν(N-O) in the Fe/Ru(II)-NO^+ type complexes as discussed above. Hence, π-backbonding from the harder Mn(II) center in $\mathbf{1^{ox}}$ is reduced compared to **1** and likely similar to Fe/Ru(II), and this accounts for the higher ν(N-O) value of $\mathbf{1^{ox}}$.

The photolabilization of NO in simple Ru(III) complexes with NO, which is generally observed upon UV excitation of the complexes,[53,63-65] has been ascribed to the population of excited states with NO(π*) character,[16] and analogous observations are made here. The symmetry-allowed metal-to-ligand CT transitions within the Mn-N-O π

system, $d_{xz}\_\pi^*_x \rightarrow \pi^*_x\_d_{xz}$ (MOs <107> → <113>) and $d_{yz}\_\pi^*_y \rightarrow \pi^*_y\_d_{yz}$ (MOs <106> → <115>), generally labeled $d_\pi\_\pi^* \rightarrow \pi^*\_d_\pi$ in the following (see red arrows in Figure 3.6), are located in the UV region around 300 nm in both the Mn-nitrosyl complexes **1** and **2**, and corresponding Ru-nitrosyl complexes (*cf.* Figure 3.9). Excitation into these MLCT transitions effectively leads to the transfer of one electron from the metal back to the formally NO^+ ligand. This charge separation leads to excited states with effective Mn(II)-NO(radical) and Ru(III)-NO(radical) character, respectively. Due to the occupation of the metal-NO antibonding $\pi^*\_d_\pi$ orbitals (*cf.* Figure 3.7), the metal-NO bond is greatly weakened in these excited states (*cf.* also refs. 16, 66). Hence, the $d_\pi\_\pi^* \rightarrow \pi^*\_d_\pi$ MLCT excited states are ideally suited to promote photodissociation of NO in these complexes. This could further be promoted if the complexes could undergo an intersystem crossing into the corresponding $d_\pi\_\pi^* \rightarrow \pi^*\_d_\pi$ excited triplet states, which, due to their extended life times, are expected to be much more efficient in the photodissociation of NO.[63]

Table 3.6 Electronic Transitions in $[Mn(PaPy_3(NO)]^+$ (1) with significant $d_{xy} \rightarrow \pi^*\_d_\pi$ Character, calculated with TD-DFT (BP86/TZVP).

TD-DFT State	Energy [cm^{-1}]	Energy [nm]	f(osc)	Major Contribution	Percent Contribution
S1	**13551**	**738**	**0**	**d_{xy} to $\pi_x^*\_d_{xz}$**	**33%**
S5	14802	675	0	d_{xy} to $\pi_x^*\_d_{xz}$ d_{xy} to $\pi_y^*\_d_{yz}$	9% 3%
S7	15657	639	0	d_{xy} to $\pi_y^*\_d_{yz}$	7%
S8	16181	618	0	d_{xy} to $\pi_y^*\_d_{yz}$	23%
S9	16687	599	0	d_{xy} to $\pi_y^*\_d_{yz}$	13%
S10	17849	560	0.0001	d_{xy} to $\pi_x^*\_d_{xz}$	47%

An additional difference between the Mn- and Ru-nitrosyl complexes with the $PaPy_3^-$ and similar coligands is the fact that the ruthenium complexes generally show photolability upon UV excitation, whereas in **1** and **2**, NO can also be photodissociated upon excitation around 400 – 500 nm. The TD-DFT calculations presented in this paper are able to straightforwardly explain this difference. Whereas in the Ru(III) complexes with NO, the $d_\pi\_\pi^* \rightarrow \pi^*\_d_\pi$ MLCT transitions are only observed in the UV region as discussed above, the analogous Mn complexes **1** and **2** exhibit lower-energy electronic transitions around 400 nm that are of $Mn(t_{2g}) \rightarrow L(Py\_\pi^*)$ character and contain

significant d_π_π^* → π^*_d_π (MOs <109> → <115>) MLCT contributions. No such transitions are observed in the analogous ruthenium complexes with the $PaPy_3^-$ and other similar coligands.[16] The presence of d_π_π^* → π^*_d_π excited states in the 400 – 500 nm spectral region of **1** (and **2**) is further substantiated by the observed strong resonance Raman enhancement of the Mn-NO stretch upon laser excitation in this energy region (*cf.* Figure 3.3). In fact, the strong resonance enhancement of this mode points towards an excited state that has a substantial displacement along the Mn-NO bond, in accordance with the proposed electron excitation into a Mn-NO antibonding orbital.

Direct excitation into the symmetry-allowed d_π_π^* → π^*_d_π MLCT transitions therefore explains the photolability of NO upon irradiation of complexes **1** and **2** in the 450 nm and the UV region (*direct mechanism*). In the case of Ru-nitrosyl complexes, this mechanism is limited to the UV region, which explains this apparent difference in the photochemistry of the analogous Mn(II) and Ru(III) complexes with NO. We believe that this difference relates to the fact that ruthenium (a) is a second row transition metal, and (b) carries a larger positive charge, which significantly increases the ligand field splitting in the ruthenium complexes, and hence, shifts all MLCT transitions to higher energy. However, photolabilization of NO *via* this direct mechanism is still not able to explain why complexes **1** and **2** can be photolyzed upon excitation in the Vis-NIR region, where no d_π_π^* → π^*_d_π MLCT transitions occur according to the TD-DFT results.

Table 3.7 The first seven Triple Excited States of $[Mn(PaPy_3(NO)]^+$ (**1**) with significant d_{xy} → π^*_d_π Character, calculated with TD-DFT (BP86/TZVP).

TD-DFT State	Energy [cm^{-1}]	Energy [nm]	f(osc)	Major Contribution	Percent Contribution
T1	**134713**	**742**	**0**	**d_{xy} to π_x^*_d_{xz}**	**66%**
T2	13584	736	0	d_{xy} to π_x^*_d_{xz} d_{xy} to π_y^*_d_{yz}	1% 3%
T3	14377	696	0	d_{xy} to π_x^*_d_{xz}	14%
T4	14739	679	0	d_{xy} to π_x^*_d_{xz} d_{xy} to π_y^*_d_{yz}	17% 6%
T5	15484	646	0	d_{xy} to π_y^*_d_{yz}	13%
T6	16141	620	0	d_{xy} to π_y^*_d_{yz}	48%
T7	16640	601	0	d_{xy} to π_y^*_d_{yz}	25%

Our spectroscopic results show that the Mn-N-O units in **1** and **2** have very similar properties, and correspondingly, should show quite similar energies for the d_π_π^* → π^*_d_π MLCT excited states. In contrast to this finding, the rates of NO photorelease in the Vis-NIR region differ significantly between these two complexes: addition of the quinoline group to the ligand frame induces not only an increase in extinction coefficient of the low-energy d_{xy} → L(Py/Q_π^*) bands and a small shift of these transitions to lower energy, but at the same time, increases the quantum yield for NO release. This strong correlation between coligand properties and NO releasing properties of the complexes combined with the absence of d_π_π^* → π^*_d_π MLCT transitions in the Vis-NIR region provides direct evidence that the photochemical mechanism of NO dissociation must be different in the Vis-NIR region, and cannot correspond to the direct mechanism described above. We therefore propose that NO photorelease in the Vis-NIR region is due to an *indirect mechanism*, where photoexcitation of the complexes first leads to occupation of a d_{xy} → L(Py/Q_π^*) excited state, which then interconverts into a Mn(d) → NO(π^*) excited state. The latter state has to correspond to a symmetry-forbidden (overlap-forbidden) MLCT, so no direct excitation into this Mn(d) → NO(π^*) excited state is possible. There are two potential candidates for such symmetry-forbidden MLCTs: these could either be of symmetry-forbidden d_π_π^* → π^*_d_π character, which correspond to the d_{xz}_π^*_x → π^*_y_d_{yz} and d_{yz}_π^*_y → π^*_x_d_{xz} transitions, or of d_{xy} → π^*_d_π (n → π^*) type. A closer inspection of the TD-DFT results for **1** shows that a multitude of excited states with distinct d_{xy} → π^*_d_π MLCT character are in fact predicted in the Vis-NIR region as shown in Table 3.7, which all have close to zero extinction coefficients due to the symmetry-forbidden nature of these transitions. *In particular, the lowest-energy excited singlet state is predicted to have significant d_{xy} → π^*_d_π character*. Furthermore, intersystem crossing into the corresponding triplet states would be advantageous for NO photorelease due to the extended life time of triplet excited states (see above). We therefore propose the following model for the indirect mechanism of NO photolabilization of complexes **1** and **2** in the Vis-NIR region: initial excitation of the complexes leads to the occupation of d_{xy} → L(Py/Q_π^*) excited states, which then interconvert into d_{xy} → π^*_d_π excited states. These latter states are ideally set up to

undergo intersystem crossing into the corresponding $d_{xy} \rightarrow \pi^*\_d_\pi$ triplet states, due to strong spin-orbit coupling between analogous $d_{xy} \rightarrow \pi^*\_d_\pi$ singlet and triplet excited states. Here, intersystem crossing is promoted by the strong admixture of d_π character into the unoccupied π^* orbitals of NO^+. The $d_{xy} \rightarrow \pi^*\_d_\pi$ triplet states show a Mn(II)-NO(radical) type electronic structure where one electron has been transferred back to the NO^+ ligand, and the Mn-NO bond is weakened (due to occupation of a Mn-NO antibonding orbital). These excited states are therefore ideally suited for photorelease of NO (see above). The TD-DFT calculations further support these ideas and show that the lowest lying triplet state (T1) in fact has significant

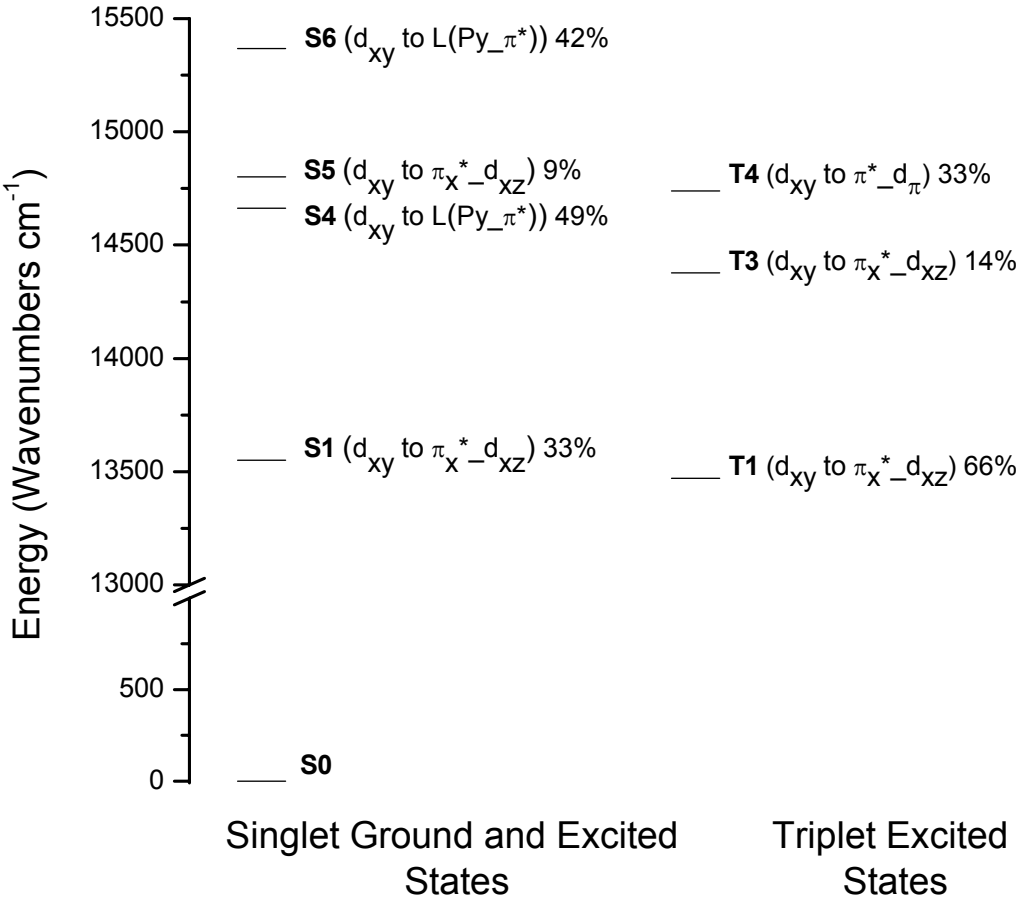

Figure 3.10 Selected singlet and triplet excited states of $[Mn(PaPy_3)(NO)]^+$.

$d_{xy} \rightarrow \pi^*\_d_\pi$ CT character as shown in Table 3.8. We therefore propose that complexes **1** and **2** release NO from their T1 ($d_{xy} \rightarrow \pi^*\_d_\pi$) excited states. Figure 3.10 shows a summary of the properties of the lowest excited states of **1** that illustrates the indirect

mechanism of NO photorelease. Once the molecule has entered a $d_{xy} \rightarrow \pi^*\_d_\pi$ excited triplet state, the Mn-NO antibonding nature of this state will promote ligand dissociation. Similar indirect mechanisms have also been demonstrated by rigorous TD-DFT calculations for the photodissociation of ligands in $[Ru(bpy)_2L_2]^{2+}$ complexes[66] and methylcobalamine.[67] Finally, the energies of the $d_{xy} \rightarrow \pi^*\_d_\pi$ excited triplet states show a small solvent dependency, and the corresponding excitation energies shifts to lower frequencies in polar solvents like acetonitrile (Table 3.8).

Table 3.8 The first seven triple excited states of $[Mn(PaPy_3(NO)]^+$ (**1**) in MeCN with significant $d_{xy} \rightarrow \pi^*\_d_\pi$ character, calculated with TD-DFT (BP86/TZVP) using COSMO.[a] The results show that the solvent field leads to a noticeable shift of the $d_{xy} \rightarrow \pi^*\_d_\pi$ transitions to lower energy (*cf.* Table 8).

TD-DFT State	Energy [cm^{-1}]	Energy [nm]	f(osc)	Major Contribution	Percent Contribution
T1	12879	777	0	d_{xy} to $\pi_y^*\_d_{yz}$ d_{xy} to $\pi_y^*\_d_{xz}$	93% 5%
T2	13522	740	0	d_{xy} to $\pi_x^*\_d_{xz}$	88%
T3	14767	677	0	d_{xy} to $\pi_y^*\_d_{xz}$	6%
T4	15330	652	0	d_{xy} to $\pi_y^*\_d_{xz}$	57%
T5	16250	615	0	d_{xy} to $\pi_y^*\_d_{yz}$	5%
T6	16581	603	0	d_{xy} to $\pi_y^*\_d_{xz}$	21%
T7	17912	558	0	d_{xy} to $\pi_x^*\_d_{yz}$	70%

This indirect mechanism by itself is not a new finding, but (a) somewhat resembles the established mechanism of action of organic triplet sensitizers, although the actual details of the underlying process are different. In addition, (b) it has been known for a long time that many transition-metal complexes after initial excitation relax into excited states (by internal conversion and intersystem crossing) that are not *directly* accessible *via* light excitation, but which are active in ligand dissociation or chemical reactions.[68-72] However, up until now it was unclear if analogous mechanisms could be involved in the photodissociation of NO from transition-metal nitrosyls. Importantly, the identification of such an indirect mechanism in the light activation of manganese-nitrosyl complexes as reported here opens up the door for a great tunability of the NO photorelease properties of the complexes with respect to two aspects:

(a) the better the energies of the initial $d_{xy} \rightarrow L(Py/Q\_\pi^*)$ and the final $d_{xy} \rightarrow \pi^*(NO)\_d_\pi$ excited triplet states are matched, the more efficient is the

interconversion between these states, and hence, the higher the quantum yields for NO photorelease; and

(b) an increase in extinction coefficient in the Vis-NIR region that leads to a larger number of molecules per second that are excited into the $d_{xy} \rightarrow L(Py/Q\_\pi^*)$ state will likely lead to an increase in k_{NO}^{off} values for NO release.

Both of these properties can be tuned *via* a variation in the coligand (here: $PaPy_3^-$ and $PaPy_2Q^-$). For example, coligands with even larger extinction coefficients in the NIR region should further enhance the NO photorelease properties. The critical $d_{xy} \rightarrow \pi^*\_d_\pi$ triple excited state could be further lowered in energy by adding coligands with in-plane (xy) π-donor properties, enabling NO photorelease at even lower excitation energies. In addition, inner ligand $\pi \rightarrow \pi^*$ triplet excited states could in principle also be utilized to populate the key $d_{xy} \rightarrow \pi^*\_d_\pi$ triple excited state required for photolabilization of NO. *Hence, the Mn(II) complexes with NO show the desired and long sought-after potential for easy tunability of their NO photolabilization properties*. This has been found difficult for compounds that operate *via* the direct mechanism (like Ru(III) complexes with NO), since the properties of the metal-NO^+ bond are much more difficult to vary to a greater extend compared to the properties of the coligand. On the other hand, the indirect mechanism does not seem to be operative for the Ru(III) complexes with NO, likely due to the stronger ligand field in this case that shifts the corresponding $d_{xy} \rightarrow \pi^*\_d_\pi$ MLCT excited states to higher energy, and hence, the $d_{xy} \rightarrow L(Py/Q\_\pi^*)$ and $d_{xy} \rightarrow \pi^*\_d_\pi$ MLCT excited singlet states are no longer in resonance for efficient interconversion.[73]

3.5 Conclusions

The vibrational spectroscopic properties and electronic structures of two Mn(II)-nitrosyl complexes were analyzed using IR- and resonance Raman spectroscopy coupled to DFT calculations. These complexes exhibit very strong Mn-NO bonds as reflected by their large Mn-NO stretching frequencies. The DFT calculations show that this is due to a Mn(I)-NO^+ type electronic structure in the singlet ground state of the complexes, where the NO^+ ligand then forms two very strong π–backbonds with the formally Mn(I) center. The photolability of NO upon excitation in the UV region is similar to analogous Ru(III)- and Fe(III)-complexes with NO and can be explained by direct excitation of $d_\pi\_\pi^* \rightarrow$

$\pi^*\_d_\pi$ CT states (transition within the Mn-NO π bond) that leads to population of Mn-NO antibonding orbitals (*direct mechanism*). On the other hand, the unusual photolability of the Mn-nitrosyl complexes upon irradiation in the Vis-NIR region is explained by the presence of low-lying $d_{xy} \rightarrow \pi^*\_d_\pi$ singlet and triplet excited states. These have close to zero oscillator strengths, but can be populated by initial excitation into $d_{xy} \rightarrow$ L(Py/Q_π^*) CT transitions between Mn and the coligand, followed by intersystem crossing into the corresponding triplet states. These can then relax into the $d_{xy} \rightarrow \pi^*\_d_\pi$ triplet excited states, which are strongly Mn-NO antibonding in nature, and hence, promote dissociation of the NO ligand (*indirect mechanism*). In comparison, in the analogous Ru(III) complexes with NO, the $d_{xy} \rightarrow \pi^*\_d_\pi$ excited states are located at higher energy, which prevents photoactivation of the NO ligand upon Vis-NIR excitation in these complexes. *The Mn*-nitrosyl complexes *therefore show the long sought-after potential for easy tunability of the NO photorelease properties by simple changes in the coligand*, due to NO photodissociation *via* the indirect mechanism, which is strongly coligand dependent.

3.6 References

(1) Ignarro, L. J. *Nitric Oxide : Biology and Pathobiology*; 1st ed.; Academic Press: San Diego, 2000.

(2) Kalsner, S. *Nitric Oxide and Free Radicals in Peripheral Neurotransmission*; Birkhäuser: Boston, 2000.

(3) Lehnert, N.; Berto, T. C.; Galinato, M. G. I.; Goodrich, L. E. *The Role of Heme-Nitrosyls in the Biosynthesis, Transport, Sensing, and Detoxificcation of Nitric Oxide (NO) in Biological Systems: Enzymes and Model Complexes; in "The Handbook of Porphyrin Science"*; World Scientific: Singapore, 2011; Vol. 14, Page 1-247 (Chapter 63).

(4) Fang, F. C. *Nitric Oxide and Infection*; Kluwer Academic/Plenum Publishers: New York, 1999.

(5) Degoute, C. S. *Drugs* **2007**, *67*, 1053-1076.

(6) Moncada, S.; Higgs, E. A.; Bagetta, G. *Nitric Oxide and the Cell : Proliferation, Differentiation, and Death.*; Princeton University Press: London, 1998.

(7) Kanwar, J. R.; Kanwar, R. K.; Burrow, H.; Baratchi, S. *Curr. Med. Chem.* **2009**, *16*, 2373-2394.

(8) Hirst, D.; Robson, T. *J. Pharm. Pharmacol.* **2007**, *59*, 3-13.

(9) Fry, N. L.; Mascharak, P. K. *Acc. Chem. Res.* **2011**, *44*, 289-298.

(10) Ford, P. C. *Acc Chem Res* **2008**, *41*, 190-200.

(11) Rose, M. J.; Mascharak, P. K. *Curr. Opin. Chem. Biol.* **2008**, *12*, 238-244.

(12) Eroy-Reveles, A. A.; Mascharak, P. K. *Future Med. Chem.* **2009**, *1*, 1497-1507.
(13) Castano, A. P.; Mroz, P.; Hamblin, M. R. *Nat. Rev. Cancer* **2006**, *6*, 535-545.
(14) Detty, M. R.; Gibson, S. L.; Wagner, S. J. *J. Med. Chem.* **2004**, *47*, 3897-3915.
(15) Ford, P. C.; Bourassa, J.; Miranda, K.; Lee, B.; Lorkovic, I.; Boggs, S.; Kudo, S.; Laverman, L. *Coord. Chem. Rev.* **1998**, *171*, 185-202.
(16) Rose, M. J.; Mascharak, P. K. *Coord. Chem. Rev.* **2008**, *252*, 2093-2114.
(17) Patra, A. K.; Afshar, R.; Olmstead, M. M.; Mascharak, P. K. *Angew. Chem. Int. Ed.* **2002**, *41*, 2512-2515.
(18) Patra, A. K.; Mascharak, P. K. *Inorg. Chem.* **2003**, *42*, 7363-7365.
(19) Eroy-Reveles, A. A.; Hoffman-Luca, C. G.; Mascharak, P. K. *Dalton T.* **2007**, 5268-5274.
(20) Rose, M. J.; Olmstead, M. M.; Mascharak, P. K. *Polyhedron* **2007**, *26*, 4713-4718.
(21) Ghosh, K.; Eroy-Reveles, A. A.; Avila, B.; Holman, T. R.; Olmstead, M. M.; Mascharak, P. K. *Inorg. Chem.* **2004**, *43*, 2988-2997.
(22) Goodrich, L. E.; Paulat, F.; Praneeth, V. K. K.; Lehnert, N. *Inorg. Chem.* **2010**, *49*, 6293-6316.
(23) Enemark, J. H.; Feltham, R. D. *Coord. Chem. Rev.* **1974**, *13*, 339-406.
(24) Scheidt, W. R.; Hatano, K.; Rupprecht, G. A.; Piciulo, P. L. *Inorg. Chem.* **1979**, *18*, 292-299.
(25) Coleman, W. M.; Taylor, L. T. *J. Am. Chem. Soc.* **1978**, *100*, 1705-1710.
(26) Tangen, E.; Conradie, J.; Franz, K.; Friedle, S.; Telser, J.; Lippard, S. J.; Ghosh, A. *Inorg. Chem.* **2010**, *49*, 2701-2705.
(27) Franz, K. J.; Lippard, S. J. *J. Am. Chem. Soc.* **1998**, *120*, 9034-9040.
(28) Rowland, J. M.; Olmstead, M.; Mascharak, P. K. *Inorg. Chem.* **2001**, *40*, 2810-2817.
(29) Eroy-Reveles, A. A.; Leung, Y.; Beavers, C. M.; Olmstead, M. M.; Mascharak, P. K. *J. Am. Chem. Soc.* **2008**, *130*, 4447-4458.
(30) Perdew, J. P. *Phys. Rev. B* **1986**, *33*, 8822-8824.
(31) Becke, A. D. *J. Chem. Phys.* **1986**, *84*, 4524-4529.
(32) Schäfer, A.; Horn, H.; Ahlrichs, R. *J. Chem. Phys.* **1992**, *97*, 2571-2577.
(33) Schäfer, A.; Huber, C.; Ahlrichs, R. *J. Chem. Phys.* **1994**, *100*, 5829-5835.
(34) Frisch, M. J.; Trucks, G. W.; Schlegel, H. B.; Scuseria, G. E.; Robb, M. A.; Cheeseman, J. R.; Montgomery, J. A., Jr.; Vreven, T.; Kudin, K. N.; Burant, J. C.; Millam, J. M.; Iyengar, S. S.; Tomasi, J.; Barone, V.; Mennucci, B.; Cossi, M.; Scalmani, G.; Rega, N.; Petersson, G. A.; Nakatsuji, H.; Hada, M.; Ehara, M.; Toyota, K.; Fukuda, R.; Hasegawa, J.; Ishida, M.; Nakajima, T.; Honda, Y.; Kitao, O.; Nakai, H.; Klene, M.; Li, X.; Knox, J. E.; Hratchian, H. P.; Cross, J. B.; Adamo, C.; Jaramillo, J.; Gomperts, R.; Stratmann, R. E.; Yazyev, O.; Austin, A. J.; Cammi, R.; Pomelli, C.; Ochterski, J. W.; Ayala, P. Y.; Morokuma, K.; Voth, G. A.; Salvador, P.; Dannenberg, J. J.; Zakrzewski, V. G.; Dapprich, S.; Daniels, A. D.; Strain, M. C.; Farkas, O.; Malick, D. K.; Rabuck, A. D.; Raghavachari, K.; Foresman, J. B.; Ortiz, J. V.; Cui, Q.; Baboul, A. G.; Clifford, S.; Cioslowski, J.; Stefanov, B. B.; Liu, G.; Liashenko, A.; Piskorz, P.; Komaromi, I.;

Martin, R. L.; Fox, D. J.; Keith, T.; Al-Laham, M. A.; Peng, C. Y.; Nanayakkara, A.; Challacombe, M.; Gill, P. M. W.; Johnson, B.; Chen, W.; Wong, M. W.; Gonzalez, C.; Pople, J. A.; Gaussian, Inc.: Pittsburgh, PA, 2003.

(35) Neese, F.; Version 2.2 ed. Max-Planck Institut für Bioanorganische Chemie, Mülheim/Ruhr, Germany, 2004.

(36) Paulat, F.; Kuschel, T.; Nather, C.; Praneeth, V. K. K.; Sander, O.; Lehnert, N. *Inorg. Chem.* **2004**, *43*, 6979-6994.

(37) Albrecht, A. C. *J. Chem. Phys.* **1961**, *34*, 1476-1484.

(38) Spiro, T. G. *Iron Porphyrins*; Lever, A. B. P., Gray, H. B., Eds.; Addison-Wesley: Reading, Mass., 1983; Part 2, Pg. 91 - 159.

(39) Krushinskii, L.; Shorygin, P. P. *Opt. Spectry.* **1961**, *11*, 12-17.

(40) Lehnert, N.; Ho, R. Y. N.; Que, L.; Solomon, E. I. *J. Am. Chem. Soc.* **2001**, *123*, 8271-8290.

(41) Parthasarathi, N.; Spiro, T. G. *Inorg. Chem.* **1987**, *26*, 2280-2282.

(42) Hoffman-Luca, C. G.; Eroy-Reveles, A. A.; Alvarenga, J.; Mascharak, P. K. *Inorg. Chem.* **2009**, *48*, 9104-9111.

(43) Fujisawa, K.; Tateda, A.; Miyashita, Y.; Okamoto, K.; Paulat, F.; Praneeth, V. K. K.; Merkle, A.; Lehnert, N. *J. Am. Chem. Soc.* **2008**, *130*, 1205-1213.

(44) Paulat, F.; Lehnert, N. *Inorg. Chem.* **2007**, *46*, 1547-1549.

(45) Lehnert, N.; Sage, J. T.; Silvernail, N.; Scheidt, W. R.; Alp, E. E.; Sturhahn, W.; Zhao, J. *Inorg. Chem.* **2010**, *49*, 7197-7215.

(46) Lehnert, N.; Praneeth, V. K. K.; Paulat, F. *J. Comp. Chem.* **2006**, *27*, 1338-1351.

(47) Praneeth, V. K. K.; Nather, C.; Peters, G.; Lehnert, N. *Inorg. Chem.* **2006**, *45*, 2795-2811.

(48) Praneeth, V. K. K.; Neese, F.; Lehnert, N. *Inorg. Chem.* **2005**, *44*, 2570-2572.

(49) Praneeth, V. K. K.; Paulat, F.; Berto, T. C.; George, S. D.; Nather, C.; Sulok, C. D.; Lehnert, N. *J. Am. Chem. Soc.* **2008**, *130*, 15288-15303.

(50) Praneeth, V. K. K.; Haupt, E.; Lehnert, N. *J. Inorg. Biochem.* **2005**, *99*, 940-948.

(51) Berto, T. C.; Hoffman, M. B.; Murata, Y.; Landenberger, K. B.; Alp, E. E.; Zhao, J.; Lehnert, N. *J. Am. Chem. Soc.* **2011**, *133*, ASAP.

(52) Soldatova, A. V.; Ibrahim, M.; Olson, J. S.; Czernuszewicz, R. S.; Spiro, T. G. *J. Am. Chem. Soc.* **2010**, *132*, 4614-4625.

(53) Fry, N. L.; Rose, M. J.; Rogow, D. L.; Nyitray, C.; Kaur, M.; Mascharak, P. K. *Inorg. Chem.* **2010**, *49*, 1487-1495.

(54) Rose, M. J.; Mascharak, P. K. *Inorg. Chem.* **2009**, *48*, 6904-6917.

(55) Franceschi, F.; Hesschenbrouck, J.; Solari, E.; Floriani, C.; Re, N.; Rizzoli, C.; Chiesi-Villa, A. *J. Chem. Soc., Dalton Trans.* **2000**, 593-604.

(56) Lewis, J.; Irving, R. J.; Wilkinson, G. *J. Inorg. Nucl. Chem.* **1958**, *7*, 32-37.

(57) Bottomley, F. *Coord. Chem. Rev.* **1978**, *26*, 7-32.

(58) Bottomley, F. *Acc. Chem. Res.* **1978**, *11*, 158-163.

(59) Averill, B. A. *Chem. Rev.* **1996**, *96*, 2951-2964.

(60) Linder, D. P.; Rodgers, K. R.; Banister, J.; Wyllie, G. R. A.; Ellison, M. K.; Scheidt, W. R. *J. Am. Chem. Soc.* **2004**, *126*, 14136-14148.

(61) Roncaroli, F.; Videla, M.; Slep, L. D.; Olabe, J. A. *Coord. Chem. Rev.* **2007**, *251*, 1903-1930.

(62) Wyllie, G. R. A.; Scheidt, W. R. *Chem. Rev.* **2002**, *102*, 1067-1089.

(63) Tfouni, E.; Krieger, M.; McGarvey, B. R.; Franco, D. W. *Coord. Chem. Rev.* **2003**, *236*, 57-69.

(64) Works, C. F.; Jocher, C. J.; Bart, G. D.; Bu, X. H.; Ford, P. C. *Inorg. Chem.* **2002**, *41*, 3728-3739.

(65) Bordini, J.; Hughes, D. L.; Neto, J. D. D.; da Cunha, C. J. *Inorg. Chem.* **2002**, *41*, 5410-5416.

(66) Salassa, L.; Garino, C.; Salassa, G.; Gobetto, R.; Nervi, C. *J. Am. Chem. Soc.* **2008**, *130*, 9590-9597.

(67) Lodowski, P.; Jaworska, M.; Andruniow, T.; Kumar, M.; Kozlowski, P. M. *J. Phys. Chem. B* **2009**, *113*, 6898-6909.

(68) Adamson, A. W.; Waltz, W. L.; Zinato, E.; Watts, D. W.; Fleischa.Pd; Lindholm, R. D. *Chem. Rev.* **1968**, *68*, 541-585.

(69) Finkenzeller, W. J.; Thompson, M. E.; Yersin, H. *Chem. Phys. Lett.* **2007**, *444*, 273-279.

(70) Lamansky, S.; Djurovich, P.; Murphy, D.; Abdel-Razzaq, F.; Lee, H. E.; Adachi, C.; Burrows, P. E.; Forrest, S. R.; Thompson, M. E. *J. Am. Chem. Soc.* **2001**, *123*, 4304-4312.

(71) Nataraja.P; Endicott, J. F. *J. Phys. Chem.* **1973**, *77*, 971-972.

(72) Crosby, G. A.; Alire, R. M.; Whan, R. E. *J. Chem. Phys.* **1961**, *34*, 743-748.

(73) Footnote *The TD-DFT calculations on the analogous [Ru(PaPy3)(NO)]2+ complex provide some support for this idea, as in this case the lowest energy dxy -> p*_dp singlet excited state is predicted to be ~5000 cm-1 higher in energy compared to 1.*

Chapter 4

Synthesis, Photolabilization and Spectroscopic Analysis of Water Soluble Ruthenium-Nitrosyl Complexes

4.1 Introduction

The physiological importance of the diatomic molecule nitric oxide (NO) was established in the 1980's, a discovery that was later rewarded with the Nobel Prize in Medicine in 1998 to Robert F. Furchgott, Ferid Murad, and Louis J. Ignarro.[1-3] The Nobel Prize was awarded for the establishment of NO as a signaling molecule within biological systems, involved in neurotransmission and regulation of blood pressure. Here, small concentrations of NO (nM) were found to be essential for biological functions. The transformation of L-arginine to citrulline by nitric oxide synthase (NOS) was found to produce NO. Within the immune system, large concentrations of NO (μM) are used to fight invasive pathogens.[4] In addition, NO has been shown to generally kill cells by inducing apoptosis, in particular cancer cells.[5-6] This property of NO has allowed researchers to incorporate NO into compounds for the treatment of cancer.

Release of NO from metal-nitrosyl complexes upon exposure to light would allow for site-specific delivery of the reactive species NO to cells *via* photodynamic therapy (PDT) and has been the focus of many studies in the recent literature.[7-12] Traditionally, PDT is a process where a photosensitizer, a non-reactive species, is irradiated with light and activated. This active species excites triplet oxygen to form singlet oxygen which can then react within the system to create reactive oxygen species, that damage biological molecules and eventually cause cell death.[8] Photorelease of NO from metal-nitrosyl complexes can be included in photodynamic therapy, since the activation of the metal-nitrosyl is caused by light, leading to the release of NO that will react with biological molecules similar to reactive oxygen species. Most research in the area of the photolabilization of metal-nitrosyl complexes has focused on iron-,[9] manganese-[13-14], and

ruthenium-nitrosyl[15] complexes, labeled $\{MNO\}^6$ in the Enemark-Feltham notation.[16] Previous work has shown that corresponding iron- and ruthenium-nitrosyl complexes are best described as M(II)-NO^+ complexes, where the bound NO^+ ligand forms two strong π backbonds with the M(II)-d^6 metal center.[17] This is in agreement with the high NO stretching frequencies (ν_{NO}: 1820-1960 cm^{-1}) of these complexes.[15-27] Correspondingly, NO adducts of analogous Mn(II) complexes have recently been shown to have Mn(I)-NO^+ type electronic structures.[28]

Although some iron-nitrosyl $\{FeNO\}^6$ complexes (ie. sodium nitroprusside and Roussin's salts) have been shown to release large amounts of NO when irradiated with low energy light, the lack of stability and toxicity of these complexes under physiological conditions has led to a search for suitable alternatives, in particular manganese- and ruthenium-nitrosyl $\{MNO\}^6$ complexes.[9] Analysis of analogous Fe, Ru, and Mn complexes with the same pentadentate ligand has shown great differences in the photolability of these compounds. For example, $[Fe(PaPy_3)(NO)](ClO_4)_2$ ($PaPy_3^-$ = *N*,*N*-bis(2-pyridylmethyl)amine-*N*-ethyl-2-pyridine-2-carboxamide) when exposed to visible light (500–600 nm) releases NO with a quantum yield (ϕ) of 0.18,[29-31] while $[Mn(PaPy_3)(NO)]ClO_4$ has a quantum yield of ~0.3 when irradiated with 500-550 nm light.[13] In contrast, the quantum yield of RuNO complexes is drastically lower: $[Ru(PaPy_3)(NO)](BF_4)_2$ requires UV light (300–450 nm) for NO release and exhibits a lower quantum yield of only ~ 0.05.[31-32]

Initial research on the photoactivation of RuNO complexes involved investigation of compounds with simple monodentate ligands, which were found to labilize under a range of conditions in addition to having a lower cytotoxicity than nitroprusside. For example, $[Ru(NH_3)_4(X)(NO)]^{3+}$, where X is NH_3, pyridine, imidazole etc., labilizes NO under acidic conditions with quantum yields ranging from 0.04-0.30.[26,33-36] Attaching polydentate ligands allows for greater control in solubility and reactivity and further decreases the toxicity of the metal ions. A number of research groups have synthesized ruthenium-nitrosyl complexes bound to polydentate ligands that are photolabile when irradiated with UV-light.[32,37-46] The mechanism by which these complexes undergo photolabilization has been analyzed by a number of research groups, and it has been found that a direct excitation of an electron from a bonding d_π_π* orbital to an

antibonding $\pi^*\_d_\pi$ orbital as shown in Scheme 4.1 left, red arrow, releases the NO from the ruthenium to form the Ru(III)-solvent photoproduct.[47-50] Adding an antenna to the Ru(II)-NO^+ complexes,[44-46,51-52] for example in [Ru($(OMe)_2$IQ1)(NO)(Resf)] (Resf = resorfin) , has shown to both increase the quantum yield and the wavelength of light required to photolabilize the Ru-NO bond; here, the quantum yield increases from 0.035 for [Ru($(OMe)_2$IQ1)(NO)(Cl)] to 0.271 for [Ru($(OMe)_2$IQ1)(NO)(Resf)] when irradiated with ~ 500 nm light.[53]

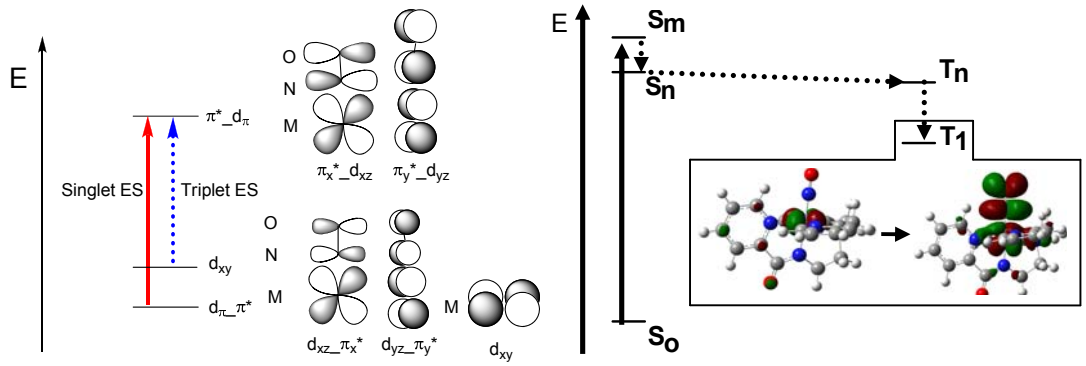

Scheme 4.1 Mechanisms of the photoactivation of NO Left: the *direct excitation* of an electron from a bonding $d_\pi\_\pi^*$ orbital to an antibonding $\pi^*\_d_\pi$ orbital (singlet excited state, red line), is responsible for photorelease of NO in ruthenium-nitrosyl complexes. The symmetry forbidden $d_{xy} \rightarrow \pi^*\_d_\pi$ metal to ligand charge transfer transition (triplet excited state, blue dashed line). Cannot be excited directly, but the corresponding triplet state can be accessed by an indirect mechanism. Right: the *indirect mechanism* for photolabilizing of the transition metal NO bond requires excitation an electron into a higher singlet excited state which can then relaxing into the symmetry forbidden $d_{xy} \rightarrow \pi^*\_d_\pi$ triplet excited state.

On the other hand, the Mn(I)-NO^+ complexes $[Mn(PaPy_3)(NO)]^+$ and $[Mn(PaPy_2Q)(NO)]^+$ show quantum yields ranging from 0.3 to 0.6, respectively, when irradiated with Vis-NIR light.[13,54-55] The process by which these Mn(I)-NO^+ complexes undergo photolabilization has recently been shown to occur through two different mechanisms, the direct mechanism as observed for the ruthenium-nitrosyl complexes (transitions from the bonding $d_\pi\_\pi^*$ to the antibonding $\pi^*\_d_\pi$ orbitals), along with an indirect mechanism where initial metal to coligand charge transfer transitions occur, followed by relaxation into a symmetry forbidden triplet excited state, as shown in Scheme 4.1, right and as indicated with a dashed blue line in Scheme 4.1, left.[28] This mechanism allows for the photolabilization of the Mn(I)-NO^+ complex to release NO at Vis-NIR energies. Although these complexes have been shown to be highly photolabile,

these compounds have a limited stability in aqueous buffer, which is not ideal for the development of a prodrug which releases NO when irradiated with light.[13] Ruthenium-nitrosyl complexes, on the other hand, have been shown to be stable under physiological conditions.[31,45] Therefore, a number of research groups have studied the photolabilization of the Ru-NO bond in a range of complexes as described above. However, most of these studies are focused on the photolabilization of the complexes in organic solvents, whereas the effect of water at physiological conditions is not well understood.[32,40,45-46]

In this chapter, we present several water-soluble ruthenium(III)-nitrosyl complexes with the coligands tris(2-methylpyridine)amine (TPA) and ethylenediaminetetraacetic acid (edta), and corresponding water-insoluble analogues, and we analyze how different solvents affect the photolabilization of these Ru-NO complexes. Previous work has indicated that such $\{RuNO\}^6$ complexes with the edta coligand are not photolabile in water; however, using a myoglobin (Mb)-based assay, we are able to show that these complexes are able to release NO photochemically. The obtained Ru-NO complexes are further characterized spectroscopically and by X-ray crystallography.

4.2 Experimental

4.2.1 Materials

All chemicals were purchased from Aldrich Chemical Co. and used without further purification, except $RuCl_3 \bullet 3H_2O$ which was obtained from Pressure Chemical Co. and picolylchloride•HCl which was purchased from Acros Organics. Nitric oxide (Cryogenic Gases, Detroit, MI) was purified by first passing through an ascarite II column (NaOH on silica gel) and then through a cold trap at -80 °C to exclude higher nitrogen oxide impurities. Isotopically labeled $^{15}N^{18}O$ was purchased from Sigma-Aldrich and was used as received. Isotopically labeled $K^{15}NO_2$ was purchased from Cambridge Isotopes and used without further purification. All solvents were dried by standard techniques and distilled prior to use. Standard Schlenk line techniques were utilized for all reactions with NO.

4.2.2 Synthesis of Precursors.

The syntheses of tris(2-pyridylmethyl)amine (TPA),[56-57] $[RuCl_2(dmso)_4]$,[58] $[Ru(TPA)Cl_2]ClO_4$ (**1**),[59] $[Ru(TPA)Cl(dmso)]PF_6$,[60] $[Ru(H_2edta)Cl(NO)]$ (**6**),[61] and [Ru(Hedta)(NO)] (**7**) [62] were performed according to literature procedures.

Caution!!! Perchlorate salts are highly explosive. Proper precautions need to be taken before synthesizing perchlorate containing complexes.

4.2.3 Preparation of Complexes.

4.2.3.1 $[Ru(TPA)Cl_2(NO)]ClO_4$ (2)

A sample of 885 mg (1.5 mmol) of **1** was placed in a purged Schlenk flask, followed by addition of 25 mL of dried deaerated acetonitrile. Nitric oxide was then introduced and the solution was stirred for 2 hours. The resulting brown solution was concentrated to a brown oil using a rotary evaporator. The brown oil was then dissolved in chloroform and a light tan solid was precipitated with diethyl ether. The precipitate was filtered, washed with diethyl ether, and collected. Yield: 721 mg (81%). This solid was further purified by recrystallizing the crude material from dichloromethane to produce brown needle-like crystals suitable for X-ray diffraction. Yield: 237 mg (23%). Selected IR frequencies (KBr disk, cm^{-1}) 1903 (ν(N-O)). Selected FT-Raman frequencies (solid, cm^{-1}) 585 (ν(Ru-NO)), 619 (δ(RuNO)). UV-Vis absorption spectrum, λ_{max}, 314 nm (880, $M^{-1}cm^{-1}$). Isotopically labeled $[Ru(TPA)Cl_2(^{15}N^{18}O)]ClO_4$ was synthesized using $^{15}N^{18}O$ as the NO source. Selected IR frequencies (KBr disk, cm^{-1}) 1868/1824 (ν(^{15}N-^{18}O)). Selected FT-Raman frequencies (solid, cm^{-1}) 565 (ν(Ru-$^{15}N^{18}O$)) and 600 (δ(Ru$^{15}N^{18}O$)). ^{1}H-NMR (CD_2Cl_2, ppm) 9.213-9.186 (2H, t, J(H,H) = 4.8 Hz, H-Py_2), 8.484-8.472 (1H, d, J(H,H) = 4.9 Hz, H-Py_1), 8.016-7.958 (2H, mult, J(H,H) = 7.7 Hz, H-Py_2), 7.888-7.849 (1H, t, J(H,H) = 6.0 Hz, H-Py_1), 7.792-7.772 (1H, d, J(H,H) = 7.8 Hz, H-Py_1), 7.631-7.593 (2H, t, J(H,H) = 7.6 Hz, H-Py_2), 7.519-7.466 (2H, quart, J(H,H) = 7.1 Hz, H-Py_2), 7.417-7.385 (1H, quart, J(H,H) = 4.9 Hz, H-Py_1), 6.099-5.004 (6H, mult, CH_2-Py). LCT-MS: m/z 492.0 $[Ru(TPA)Cl_2(NO)]^+$.

4.2.3.2 $[Ru(TPA)(NO_2)_2]$ (3)

A sample of 97 mg (0.15 mmol) of $[Ru(TPA)Cl(dmso)]PF_6$ was placed in 5 ml of water and stirred. To the $[Ru(TPA)Cl(dmso)]PF_6$ suspension, 36 mg (0.42 mmol) of KNO_2 in 4 ml of water was added dropwise and then refluxed for 4 hrs. The solution was cooled to room temperature. Upon cooling, the target complex precipitated out of solution as a yellow powder. Yield: 52 mg (72%). $[Ru(TPA)(NO_2)_2]$ was further purified *via* recrystallization from methanol. Selected IR frequencies (KBr disk, cm^{-1}) 1350-1190 (ν(N-O)nitrite). Isotopically labeled $[Ru(TPA)(^{15}NO_2)_2]$ was synthesized using $K^{15}NO_2$ as the NO_2^- source. Selected IR frequencies (KBr disk, cm^{-1}) 1320-1170 (ν(^{15}N-O)nitrite). ^{1}H-NMR (CD_3OD, ppm) 9.097-9.083 (2H, d, J(H,H) = 5.5 Hz, H-Py_2), 8.865-8.851 (1H, d, J(H,H) = 5.7 Hz, H-Py_1), 7.640-7.601 (2H, t, J(H,H) = 7.7 Hz, H-Py_2), 7.443-7.424 (1H, t, J(H,H) = 7.8 Hz, H-Py_1), 7.320-7.301 (2H, d, J(H,H) = 7.8 Hz, H-Py_2), 7.209-7.176 (2H, t, J(H,H) = 6.6 Hz, H-Py_2), 7.108-7.091 (1H, t, J(H,H) = 6.7 Hz, H-Py_1), 7.000-6.980 (1H, d, J(H,H) = 8.0 Hz, H-Py_1), 5.045 (2H, d, J(H,H) = 15.0 Hz, -CH_2-Py_1), 4.488 (4H, d, J(H,H) = 11.8 Hz -CH_2-Py_2). LCT-MS: m/z 438.0 $[Ru(TPA)(NO_2)]^+$.

4.2.3.3 $[Ru(TPA)(ONO)(NO)](PF_6)_2$ (4)

A sample of 100 mg (0.205 mmol) of $[Ru(TPA)(NO_2)_2]$ was suspended in 5 mL of water. To the suspension excess HPF_6 was added dropwise which turned the solid pink. The resulting suspension was stirred for 18 hours. The suspension was filtered and washed with cold water to obtain a number of isomer. The crude $[Ru(TPA)(ONO)(NO)](PF_6)_2$ complex was collected. Yield: 0.145 g (96%). Selected IR frequencies (KBr disk, cm^{-1}) 1954/1935/1920 (ν(N-O)). The crude $[Ru(TPA)(ONO)(NO)](PF_6)_2$ material was purified *via* recrystallization from water. Yield: 8 mg (5%). Selected IR frequencies (KBr disk, cm^{-1}) 1930 (ν(N-O)). ^{1}H-NMR (CD_3CN, ppm). 8.931 (1H, d, H-Py_1), 8.704 (2H, d, H-Py_2), 8.285-8.253 (2H, t, J(H,H) = 6.4 Hz, H-Py_2), 8.160-8.144 (1H, t, J(H,H) = 6.3 Hz, H-Py_1), 7.922-7.905 (2H, d, J(H,H) = 6.7 Hz, H-Py_2), 7.779-7.725 (3H, m, J(H,H) = 7.3 Hz, 1-H-Py_1 & 2-H-Py_2), 7.630-7.614 (1H, d, J(H,H) = 6.5 Hz, H-Py_1), 5.915 (2H, d, J(H,H) = 16.4 Hz, -CH_2-Py_1), 5.533 (4H, d, J(H,H) = 16.4 Hz, -CH_2-Py_2) LCT-MS: no observable mass peak.

4.2.3.4 [Ru(TPA)(Urea)(NO)](PF$_6$)$_3$ (5)

Crude [Ru(TPA)(ONO)(NO)](PF$_6$)$_2$ (80 mg, 0.1 mmol) was placed in 5 mL of water and heated until completely dissolved. To this solution 18 mg (0.2 mmol) of urea and 0.2 mL of HPF_6 were added and the resulting solution was heated for 1 hour, then cooled. To this solution excess HPF_6 was added to precipitate out [Ru(TPA)(Urea)(NO)](PF$_6$)$_3$ which was washed with cold water. Yield: 84 mg (92%). Selected IR frequencies (KBr disk, cm^{-1}) 1932 (ν(N-O). Selected FT-Raman frequencies (solid, cm^{-1}) 577 (ν(Ru-N)) and 616/597 (δ(RuNO)). Isotopically labeled [Ru(TPA)(Urea)(^{15}NO)](PF$_6$)$_2$ was synthesized using [Ru(TPA)(ONO)(^{15}NO)](PF$_6$)$_2$. Selected IR frequencies (KBr disk, cm^{-1}) 1895 (ν(^{15}N-O)). Selected FT-Raman frequencies (solid, cm^{-1}) 571 (ν(Ru-^{15}NO)) and 604/590 (δ(Ru^{15}NO)). ^{1}H-NMR (d6-dmso, ppm). 8.85 (d, 2H, H-Py$_2$), 8.19 (t, 2H, H-Py$_2$), 7.98 (t, 1H, H-Py$_1$), 7.77 (d, 2H, H-Py$_2$), 7.61 (t, 2H, H-Py$_2$), 7.43 (d, 1H, H-Py$_1$), 7.21-6.80 (br d, 2H, H-Py$_1$), 6.80-4.00 (br s, H_2O H-bonding to urea), 5.51 (m, H_2-N$_{urea}$). LCT-MS: no observable mass peak.

Table 4.1 Crystal Data and results of the structure refinement for compounds **1•0.5MeOH•0.5H$_2$O**, **2•CH$_2$Cl$_2$**, **3•2MeOH** , **4.**

Complex	**1•0.5MeOH•0.5H$_2$O**	**2•CH$_2$Cl$_2$**	**3•2MeOH**	**4**
Empirical formula	$C_{18.5}H_{21}Cl_3N_4O_5Ru$	$C_{19}H_{20}Cl_5N_5O_5Ru$	$C_{20}H_{26}N_6O_6Ru$	$C_{18}H_{18}F_{12}N_6O_3P_2Ru$
Formula weight (g/mol)	566.81	676.75	547.54	757.39
T(K)	85	85	85	85
Space Group	Monoclinic, P2(1)/c	Monoclinic, P2(1)	Orthorhombic, Pccn	Monoclinic, P2(1)/n
a (Å)	10.4799	9.7546	19.347	16.3726
b (Å)	15.1542	13.7776	14.704	9.9439
c (Å)	14.4573	9.9353	16.562	17.3570
α (deg)	90	90	90	90
β (deg)	108.579	110.935	90	114.313
γ (deg)	90	90	90	90
V (Å^3)	2176.4	1247.11	4712	2575.2
Z	4	2	8	4
μ (mm^{-1})	1.129	10.393	0.713	7.272
λ (Å)	0.71073	1.54187	0.71073	1.54178
Collected reflns	75588	16404	63152	39910
Unique reflns	6147	3946	3651	4645
R_{int}	0.0313	0.0343	0.1070	0.0512
GOF	1.073	1.050	1.096	1.159
R1[a] [I > 2σ(I)]	0.0214	0.0175	0.0599	0.0462
wR2 (all data)	0.0578	0.0405	0.1521	0.1137

[a] R1= ∑jj*F*oj - j*F*cjj/∑j*F*oj; wR2) [∑[*w*(*F*o^2 - *F*c^2)^2]/∑[*w*(*F*o^2)^2]]$^{1/2}$

4.2.4 Crystal Structure Determination

Crystal structure determination was carried out using a Bruker SMART APEX CCD-based X-ray diffractometer equipped with a low temperature device and a fine focus Mo-target X-ray tube (wavelengths: 0.71073, 1.54178 or 1.54187 Å) operated at 1500 W power (50 kV, 30 mA).[63] The data were processed with SADABS and corrected for absorption. The structures were solved and refined with the Bruker SHELXTL (ver. 2008/3) software package.[64-65] Instrument parameters, crystal data, and data collection parameters for all the complexes are summarized in Table 4.1. Selected bond distances and bond angles for **1** – **4** are listed in Table 4.2.

4.2.5 Spectroscopy

4.2.5.1 UV-Vis Spectroscopy

The electronic absorption spectra were recorded in 1 cm quartz cuvettes using a Varian-Cary 5000 or a Varian-Cary 1E UV-Visible spectrophotometer.

4.2.5.2 Vibrational Spectroscopy

Mid-infrared spectra (MIR) were obtained from KBr disks on a Perkin-Elmer FT-IR spectrometer SPECTRUM Bx at room temperature. FT-Raman spectra were recorded on a Bruker IFS 66 interferometer with a Bruker FRA 106 Raman attachment using a Nd:YAG laser for excitation (λ = 1064 nm). Measurements were performed on pure compounds at room temperature. The resolution was set to 2 cm^{-1}.

4.2.5.3 EPR and ^{1}H-NMR Spectroscopy

A Bruker X-band EMX spectrometer equipped with an Oxford Instruments liquid nitrogen or liquid helium cryostat was used for EPR measurements. EPR spectra were typically obtained on frozen solutions using ~ 20 mW microwave power and 100 kHz field modulation with the amplitude set to 1 G. Sample concentrations employed were ~ 5 mM. Proton nuclear magnetic resonance spectra were recorded on a Varian Inova 400 MHz instrument in a variety of deuterated solvents.

4.2.5.4 Mass Spectrometry

LCT-ESI mass spectra were obtained on a Micromass LCT Time-of-Flight mass spectrometer.

4.2.6 Density Functional Calculations

Spin-restricted DFT calculations using the BP86 functional[66-67] together with Ahlrichs' TZVP basis set were performed using Gaussian 03.[68-70] The structures of the cations $[Ru(TPA)Cl_2(NO)]^+$ and $[Ru(TPA)(ONO)(NO)]^{2+}$ were fully optimized and the vibrational frequencies of the fully optimized complexes were calculated with BP86/TZVP, showing no imaginary frequencies. IR and non-resonance Raman intensities were calculated as well to assist in spectral assignments. In addition, the structures of the two isomers of $[Ru(TPA)X(NO)]^{n+}$, where X = Cl^-, H_2O, NO_2^-, and ONO^-, were fully optimized with BP86/TZVP and the vibrational frequencies were calculated. No imaginary frequencies were observed for all of these structures. Based on these results, the relative change in ν(N-O) and the total energy of these isomers can be predicted.

4.2.7 Photolabilization and Quantum Yield Measurements

The photolabilization experiments with the ruthenium-nitrosyl complexes were performed using a UV lamp and followed by UV-Vis absorption spectroscopy. Chemical actinometry was used to obtain the photon flux *via* photolysis of ferric oxalate solutions.[71] The light source was a 100 W high-pressure mercury lamp with a UV filter in addition to a broadband filter to decrease the intensity of the light used to irradiate the samples. A sample of known volume in a 1 cm quartz cuvette was repeatedly irradiated for a defined time period, usually 1 minute. The UV-Vis spectrum of the sample was recorded after each irradiation period, and this procedure was repeated until the complex was completely photodissociated or the complete formation of metmyoglobin was observed. Only the first 20% of the photolabilization data were used to determine the quantum yield. For example, solutions of $[Ru(TPA)Cl_2(NO)]ClO_4$ and $[Ru(TPA)(Urea)(NO)](PF_6)_3$ in DMF were photolabilized completely, while the quantum yield was calculated from the first 20% of the reaction. The water-soluble ruthenium-nitrosyl complexes were photolabilized in the presence of oxymyoglobin, with a

ruthenium to oxymyoglobin ratio of ~ 5:1. The complete transformation of oxymyoglobin to metmyoglobin therefore corresponds to ~20% of the ruthenium complexes photolabilized, and these data were used to obtain the quantum yield.[72] The quantum yields were determined by first calculating the intensity of the light used for irradiating the samples *via* chemical actinometry.[71] Equation 1 then shows the formula that is used to calculate an unknown quantum yield with the known intensity of light.[73] Substituting A/ε with the rearranged Lambert-Beer law gives equation 2 which can be used to find the unknown quantum yield. Here, c is the concentration of the photoproduct, I is the intensity of light in einsteins min^{-1}, d is the path length of the UV-Vis cuvette used to obtain the absorption spectra, V_2 is the volume of irradiated solution in liter, ϕ is the quantum yield, and t is the irradiation time in minutes. Fitting the concentration versus time plots of the different complexes was then used to obtain the slope, which is a constant multiplied by the quantum yield, as shown in equation 2. In this way, the quantum yields for the different complexes were obtained.

$$I = \frac{AV_2}{\varepsilon d \phi t} \qquad (1)$$

$$c = \frac{Id}{V_2}\ \phi t \qquad \text{plot c vs. t to calculate } \phi \qquad (2)$$

4.3 Results and Analysis

4.3.1 Syntheses and Structures of {Ru(TPA)} Precursors

In order to synthesize the ruthenium-nitrosyl complexes two different routes were explored using ruthenium precursors in different oxidation states. For the synthesis of $[Ru(TPA)Cl_2(NO)]ClO_4$ (**2**), the Ru(III) precursor $[Ru(TPA)Cl_2]ClO_4$ (**1**) was prepared by refluxing $Ru(III)Cl_3 \bullet 3H_2O$ with TPA in methanol for 18 hours.[59] On the other hand, the precursor for $[Ru(TPA)(ONO)(NO)](PF_6)_2$ (**4**) was obtained by reaction of TPA with $[RuCl_2(dmso)_4]$ to form $[Ru(TPA)Cl(dmso)]PF_6$, following published procedures.[60] To this Ru(II) complex, two equivalents of potassium nitrite were added, and the resulting mixture was refluxed in methanol for 12 hours. This lead to the formation of the ruthenium(II) complex $[Ru(TPA)(NO_2)_2]$ (**3**), which is the first bis-nitrite complex of Ru(II) with a multidentate coligand that has been reported to date (to the best of our

knowledge). All $Ru(NO_2)_2$ complexes reported so far contain mono-, bidentate, or macrocyclic coligands.[74-85]

X-ray quality crystals of **1** were prepared *via* the recrystallization of crude **1** in methanol. In this way, brown plate-like crystals of **1** were obtained that show the monoclinic space group P2(1)/c. The bond distances between ruthenium and the nitrogen atoms of TPA were found to be 2.070, 2.060, 2.065, and 2.078 Å for the $Ru\text{-}N_{am}$ (am = amine), the two $Ru\text{-}N_{py}$ (trans to py; py = pyridine), and the $Ru\text{-}N_{py}$ (trans to Cl) bonds, respectively. The distances for the Ru-Cl bonds were long with 2.329 (trans to am) and 2.359 Å (trans to py), respectively. Note that these geometric parameters are averages over the four complexes in the unit cell. These bond distances are also in close agreement with other crystal structures of **1** published previously, where this complex crystallized in space group $P2_12_12_1$.[59,86] The structure of **1** shows that the Ru-Cl bond trans to py is 0.03 Å longer than the other one, which led us to believe that when the complex is reacted with NO, the Cl^- ligand with the longer Ru-Cl bond would be displaced by NO. To our surprise, this was not the case. In fact, NO replaces one of the py rings of TPA as

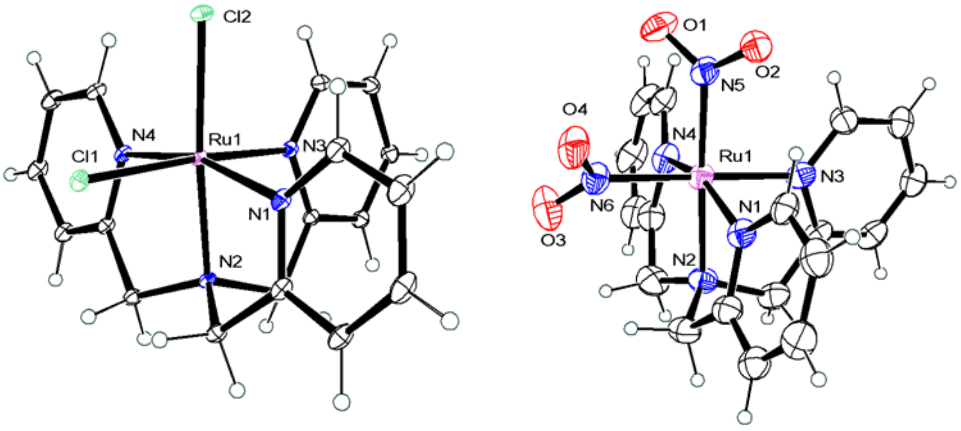

described below. In retrospect, this explains why the resulting complex, **2**, is not water-soluble. This complex is in fact only a monocation.

Figure 4.1 Crystal structures of $[Ru(TPA)Cl_2]ClO_4 \bullet 0.5MeOH \bullet 0.5H_2O$ (1, left) and $[Ru(TPA)(NO_2)_2] \bullet 2MeOH$ (3, right) with labeling. Ellipsoids are drawn at 50% probability. Counter ions are omitted for clarity. Experimental parameters are given in Table 4.1. Table 4.2 lists important geometric parameters.

Complex **3** was crystallized in methanol to form orange X-ray quality crystals with the orthorhombic space group Pccn. The $Ru\text{-}N_{am}$ bond distance is 2.104 Å in **3**, which is slightly longer than that found in **1** (2.070 Å). The two $Ru\text{-}N_{py}$ (trans to py) bond

distances of 2.066 and 2.101 Å differ more strongly from each other compared to **1**. The overall shorter Ru-N distances in **1** are a reflection of the higher oxidation state of Ru in this complex. Finally, the Ru-N_{NO2} distances of 2.031 and 2.034 Å are essentially identical. Interestingly, both nitrite ligands are N-bound in complex **3**. In addition, the Ru-N_{NO2} bonds in **3** are shorter than those in other Ru(II)-$(NO_2)_2$ complexes. For example, $[Ru(HaaiCH_2Ph)_2(NO_2)_2]$ has equivalent Ru-N_{NO2} bond distances of 2.137 Å.[87] Complexes with more than two nitrites bound to Ru(II), on the other hand, have very

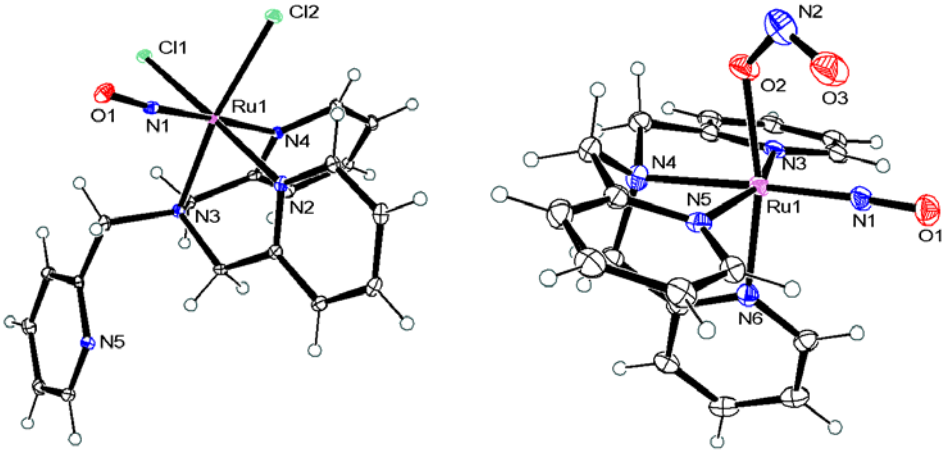

similar bond distances to **3**. Since both Ru-N_{NO2} distances are similar in **3**, one might expect that addition of acid to this complex to form the corresponding NO complex would generate two isomers with NO trans to either am or py. Table 4.2 lists structural parameters of **1** and **2**.

Figure 4.2 Crystal structures of $[Ru(TPA)Cl_2(NO)]ClO_4 \bullet CH_2Cl_2$ (2, left) and $[Ru(TPA)(ONO)(NO)](PF_6)_2$ (4, right) with labeling. Ellipsoids are drawn at 50% probability. Counter ions are omitted for clarity. Experimental parameters are given in Table 4.1. Table 4.2 lists important geometric parameters.

4.3.2 Syntheses and Structures of {Ru(TPA)} Nitrosyls

The syntheses of the two different Ru-NO complexes utilized the Ru(III) and Ru(II) precursors **1** and **3** described above. Using precursor **1**, compound **2** was obtained by the simple reaction of **1** with NO gas in an air free environment, followed by stirring the resulting solution for 2 hours. On the other hand, complex **4** was synthesized by reacting the Ru(II)-bisnitrite complex, **3**, with an excess of acid. Here, the reaction of NO_2^- with acid formed coordinated NO^+ and water. The crude material obtained this way was a mixture of different ruthenium-nitrosyl complexes as evident from IR spectroscopy (see

below). The crystallization of **4** in water formed crystals of only one species suitable for X-ray crystallography in low yield (see below). In summary, both of these general synthetic routes applied here successfully form $\{RuNO\}^6$ complexes, in agreement with reports in the literature.[72]

Table 4.2 Geometric parameters [in Å] of ruthenium complexes **1** – **4** obtained from the crystal structures, and BP86/TZVP optimized structures of complexes **2** and **4**.

	1	**2**			**3**	**4**	
	Exp.	Exp.	Opt.		Exp.	Exp.	Opt.
Ru-N_{am}	2.070	2.126	2.202	Ru-N_{am}	2.104	2.143	2.127
Ru-N_{py} (trans to Cl)	2.078	2.062	2.138	Ru-N_{py} (trans to py)	2.101, 2.066	2.084, 2.078	2.126, 2.133
Ru-N_{py} (trans to py or NO)	2.060, 2.065	2.102	2.160	Ru-N_{py} (trans to NO_2 or ONO)	2.068	2.091	2.156
Ru-Cl (trans to am)	2.329	2.365	2.391	Ru-N_{NO2} or Ru-O_{ONO}	2.031, 2.034	2.030	2.022
Ru-Cl (trans to py)	2.359	2.377	2.407	N-O_{NO2}	1.245, 1.252 1.218, 1.255	1.329, 1.182	1.452, 1.173
Ru-NO	-	1.743	1.783	Ru-NO	-	1.773	1.818
N-O	-	1.148	1.151	N-O	-	1.131	1.152
Ru-N-O[a]	-	172°	174°	Ru-N-O[a]	-	176°	175°
[a] in degrees							

Compound **2** was crystallized from dichloromethane to form brown needle-like crystals with the monoclinic space group P2(1). The bond distances between the ruthenium and the nitrogen atoms of TPA are 2.126, 2.062 and 2.102 Å for the Ru-N_{am}, Ru-N_{py} (trans to Cl), and Ru-N_{py} (trans to am) bonds, respectively. Interestingly, the TPA ligand is only 3-coordinate in **2**, which means that NO replaces one of the py groups of TPA when this diatomic binds to $[Ru(TPA)Cl_2]^+$. Neither of the chloride ligands dissociate from the ruthenium to bind NO. The Ru-N_{am} and Ru-N_{py} (trans to am) bond distances are distinctively longer than those of precursor **1**. The Ru-N_{NO} bond distance of 1.743 Å for **2** and the Ru-N-O angle of 172° are characteristic of $\{RuNO\}^6$ complexes having a Ru(II)-NO^+ electronic structure,[17] which is further supported by vibrational spectroscopy (see below). The N-O distance is obtained at 1.148 Å.

Compound **4** was crystallized from methanol to form red blade-like crystals with the monoclinic space group P2(1)/n. The distances for the Ru-$N_{am,}$ Ru-N_{py} (trans to py), Ru-N_{py} (trans to py), and Ru-N_{py} (trans to ONO) bonds are 2.143, 2.084, 2.078, and 2.091 Å, respectively as shown in Table 4.2. Interestingly, the crystal structure of complex **4** shows nitrite O-bound and not N-bound like the precursor. The resulting Ru-O_{ONO} bond distance is 2.030 Å, which is similar to the Ru-N_{NO2} distance in the bisnitrite complex **3**

(2.031 and 2.034 Å). We therefore postulate that the different isomers of **4** observed in the crude material correspond to complexes where nitrite is either O- or N-bound, and where the trans ligand of NO is either the am or a py group of TPA. The Ru-NO and N-O bond distances, 1.773 and 1.131 Å, in addition to the end-on bound NO with a Ru-N-O angle of 176^{o} are in agreement with this {RuNO}^{6} complex having a Ru(II)-NO^{+} electronic structure.[17] Geometric parameters of **2** and **4** are collected in Table 4.2.

Table 4.3 Comparison of experimental and DFT-calculated vibrational frequencies of the RuNO units in complexes **2**, **4**, **5**, and comparison to literature values.

			ν(N-O) [cm^{-1}]	δ(RuNO) [cm^{-1}]	ν(Ru-NO) [cm^{-1}]	Diff. δ–ν[d]
2	Experimental	NAI	1903	585	619	-34
		$^{15}N^{18}O$	1824/1868	565	600	-35
		Δ[a]	79	18	19	-
	Computational[b]	NAI	1900	568/557	592	-30
		$^{15}N^{18}O$	1819	550/539	573	-29
		Δ[a]	81	18	19	-
4	Experimental	NAI	1930	-	-	-
	Computational[b]	NAI	1878	580/537	569/519	15
		^{15}NO	1841	567/530	565/515	9
		Δ	37	13/7	4	-
5	Experimental	NAI	1930	616/597	577	30
		^{15}NO	1895	604/590	571	26
		Δ[a]	35	12/7	6	-
$[Ru(NH_3)_5(NO)]^{3+}$ [17]	Experimental	NAI	1911	602	594	8
		^{15}NO	1872	588	590	-2
		Δ[a]	55	14	4	-
	Computational[c]	NAI	1905	591/586	567	22
$[Ru(PaPy_3)(NO)]^{2+}$ [31]	Experimental	NAI	1899	-	-	-
$[Ru(NO)Cl_5]^{2-}$ [88]	Experimental	NAI	1900	-	-	-
Trans-$[Ru(NH_3)_4(NO)(4\text{-pic})]^{3+}$ [26]	Experimental	NAI	1934	-	-	-
trans-[Ru(cyclam)Cl(NO)]$^{2+}$ [89]	Experimental	NAI	1875	-	-	-

[a]Δ is the difference between natural abundance (NAI) and the isotopically labeled vibrations.
[b]BP86/TZVP [c]B3LYP/LanL2DZ [d] Difference between δ(RuNO) and ν(Ru-NO).

4.3.3 Spectroscopic Properties

^{1}H-NMR spectra were measured for complexes **2**, **3** and **4**. The ruthenium-nitrosyl complexes, **2** and **4**, have sharp narrow-width peaks in the ^{1}H-NMR spectrum and lack EPR signals, which confirms an S=0 ground state in agreement with the Ru(II)-NO^{+} electronic structure description. Due to the trigonal facial binding mode of the TPA ligand in complex **2**, the pyridine hydrogen atoms of each ring are all in slightly different

environments. The two bound pyridines have very similar local environments, so the ^{1}H-NMR spectra show overlapping signals, i.e. a multiplet at 8.0 ppm. In contrast, the free py group in complex shows the aromatic C-H resonance at 8.5, 7.8, and 7.4 ppm. In addition, the -CH_2-Py hydrogen atoms are all in different environments, so the ^{1}H-NMR resonances of these methylene hydrogens are found anywhere between 6.1 ppm to 5.0 ppm. For the other complexes **3** and **4**, the ^{1}H-NMR signals of the py protons are all very similar (see Figures 4.3, 4.4 and 4.5)

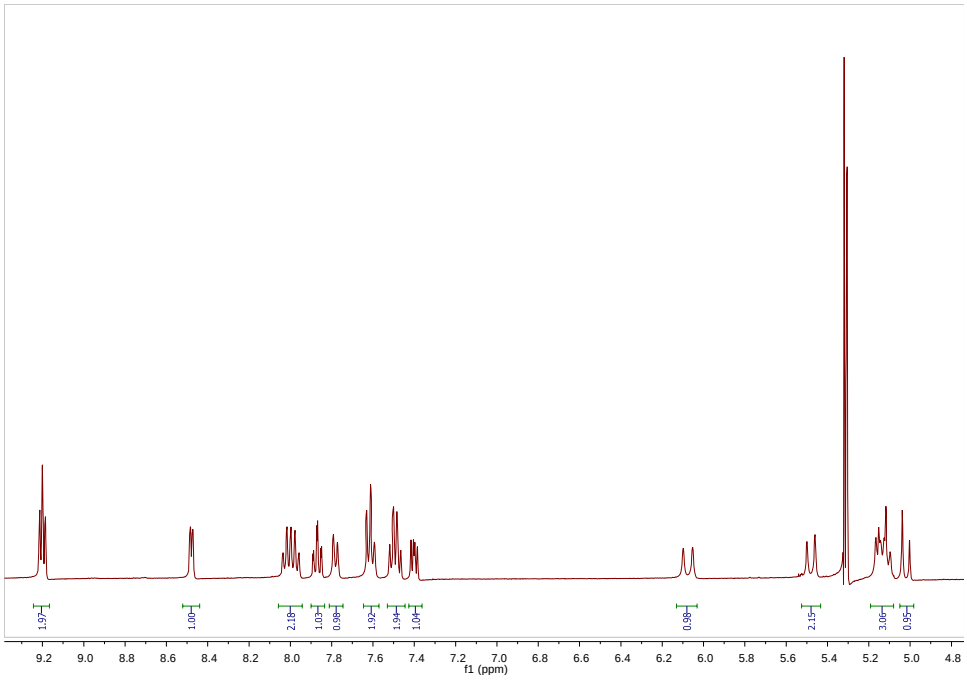

Figure 4.3 ^{1}H-NMR spectrum of **2** in deuterated dichloromethane. The aromatic protons are observed as a range of doublets and multiplets. The methylene hydrogens are found in a wide range between 5 and 6 ppm.

Vibrational data for complexes **2, 3** and **4** were obtained using mid-IR (MIR) and FT-Raman spectroscopy. Complexes **2** and **4** were found to have NO vibrations at 1903 cm^{-1} and 1930 cm^{-1}, respectively. Isotopically labeled NO, $^{15}N^{18}O$, shifts the ν(N–O) vibration from 1903 cm^{-1} to 1825 cm^{-1} (plus a shoulder at 1868 cm^{-1}) in complex **2**. These numbers are similar to the N-O stretching frequencies observed for other Ru(II)-NO^{+} complexes reported previously (see Table 4.3).[17]

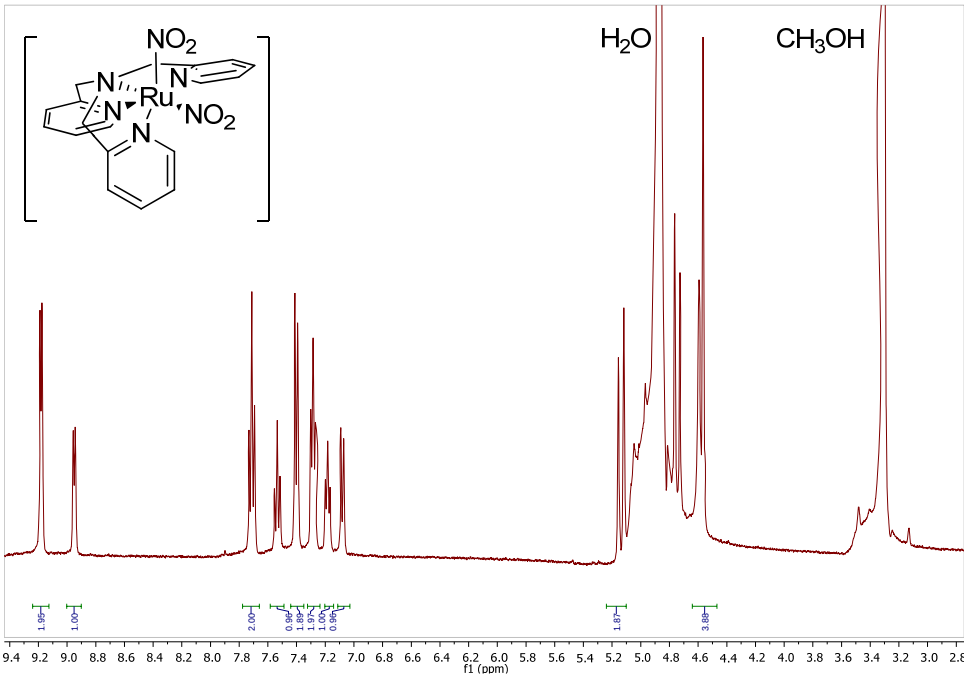

Figure 4.4 ^{1}H-NMR spectrum of **3** in deuterated methanol. The aromatic protons are observed as a range of doublets and triplets. The methylene hydrogens are found around ~5 ppm.

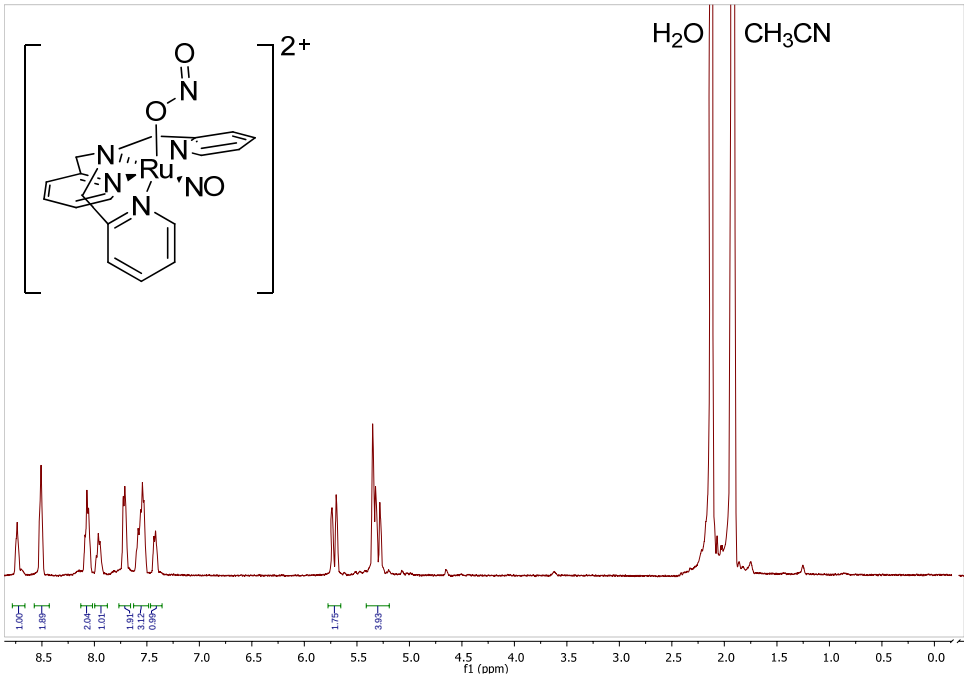

Figure 4.5 ^{1}H-NMR spectrum of **4** in deuterated acetonitrile. The aromatic protons are observed as a range of doublets and triplets. The methylene hydrogens are found around ~5 ppm.

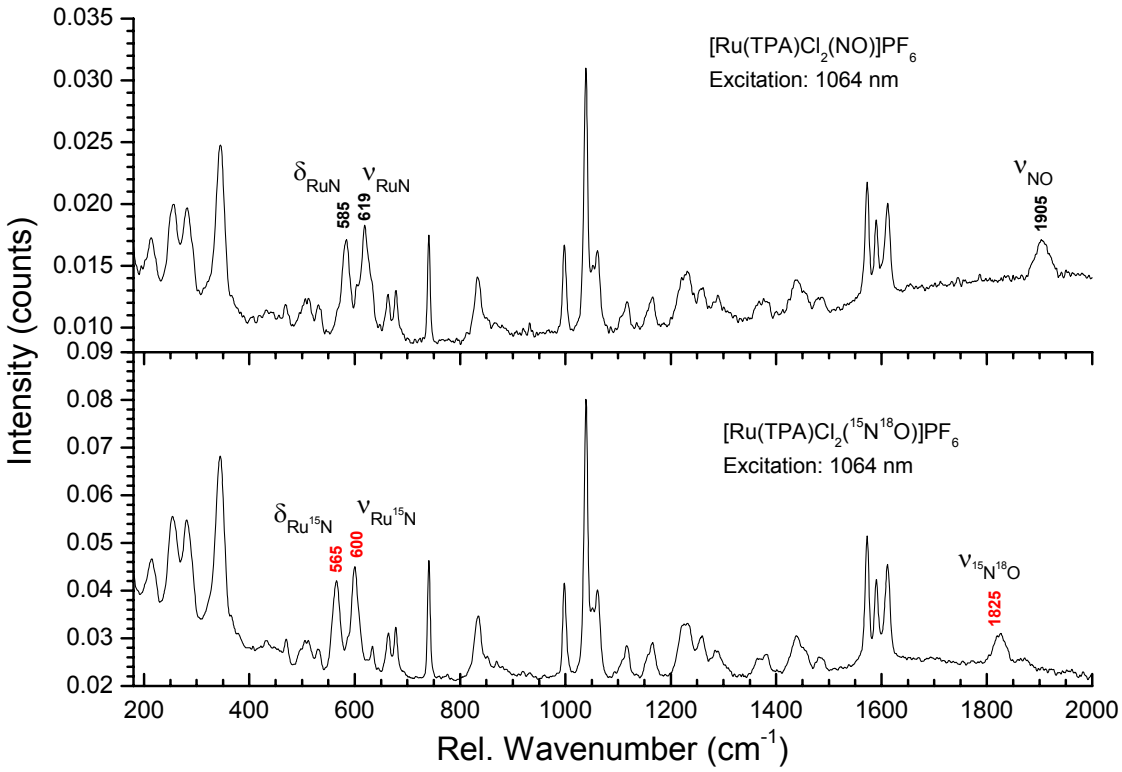

Figure 4.6 FT-Raman spectrum of 2 NAI and $^{15}N^{18}O$.

The crude **4** was shown to have a number of different N-O stretching vibrations, 1954, 1934, 1921 and 1911 cm^{-1}. Upon crystallization of this material, we obtained a complex with only ν(N–O) vibration at 1930 cm^{-1}. A range of different isomers with the overall structure $[Ru(TPA)X(NO)]^{n+}$, where X is NO_2^-, ONO^-, H_2O, and Cl^-, were computationally analyzed for their vibrational frequencies, optimized geometries, and relative energies (see below) to obtain insight into the nature of the different NO complexes obtained in the crude material.

The Ru-NO stretching mode, ν(Ru-NO), of complex **2** is observed at 619 cm^{-1}, while the linear bending modes, δ(RuNO), are found at 585 cm^{-1} in the FT-Raman spectra. These shift to 600 and 565 cm^{-1} in the $^{15}N^{18}O$-labeled complex, respectively. These assignments are included in Table 4.3. The assignments of the Ru-NO stretch and the Ru-N-O linear bends in **2** and **4** were further corroborated using DFT calculations on the BP86/TZVP level. For both **2** and **4**, the computationally optimized structures of these complexes are similar to the experimental structures, *cf.* Table 4.2. For example, the

calculated Ru-NO and N-O bond distances of 1.743 and 1.151 for **2** and 1.773 and 1.152 Å for **4** compare well to the experimental bond lengths.

Table 4.4 Frequencies and relative energies of different isomers of complexes 4: 4b, *cis*-$[Ru(TPA)(NO_2)(NO)]^{2+}$ (8), *trans*-$[Ru(TPA)(NO_2)(NO)]^{2+}$ (8b), 5, 5b, *cis*-$[Ru(TPA)Cl(NO)]^{2+}$(9) and *trans*-$[Ru(TPA)Cl(NO)]^{2+}$(9b).

	X= ONO^-		X=NO_2^-		X=H_2O		X = Cl^-	
Position of X	Cis am	Trans am	Cis am	Trans am	Cis am	Trans am	Cis am	Trans am
	4	**4b**	**8**	**8b**	**10**	**10b**	**9**	**9b**
Ru-N_{am} [Å]	2.127	2.154	2.150	2.187	2.123	2.085	2.141	2.141
Ru-N_{py} (trans to py) [Å]	2.126, 2.133	2.126, 2.126	2.122, 2.146	2.153, 2.151	2.139, 2.145	2.148, 2.147	2.129, 2.134	2.123, 2.126
Ru-N_{py} (trans to X or NO) [Å]	2.156	2.123	2.226	2.153	2.083	2.103	2.147	2.153
Ru-X [Å]	2.022	2.025	2.140	2.143	2.236	2.251	2.396	2.395
N-O_{NO2} [Å]	1.452, 1.173	1.450, 1.176	1.237, 1.224	1.234, 1.229	-	-	-	-
Ru-NO [Å]	1.818	1.821	1.805	1.807	1.819	1.825	1.799	1.800
N-O [Å]	1.152	1.151	1.146	1.147	1.142	1.141	1.147	1.146
Ru-N-O	175°	177°	179°	175°	177°	174°	174°	171°
ν(N-O) [cm^{-1}]	1878	1885	1908	1911	1930	1933	1911	1919
ν(Ru-NO) [cm^{-1}]	569 / 519	570/514	564	567	544	529	583[a]	582[a]
δ(Ru-N-O) [cm^{-1}]	580/ 537	591/537	581/ 536	595/ 585/529	592/ 572	596/ 577	577/ 552[a]	587/ 536[a]
Relative ν(N-O)	0	7	30	33	52	55	33	41
Relative Energy (BP86/TZVP)	+1.3	+3.3	+2.2	0	0	+3.5	0	+7.3

[a] These bending and stretching vibrations are strongly mixed.

In complex **2**, the linear bending modes are predicted at 568/557 cm^{-1} whereas the stretching mode is obtained at 592 cm^{-1} in the DFT calculations. Computational vibrational frequencies of complex **4** are calculated at 580/537 cm^{-1} and 569/519 cm^{-1} for the Ru-N-O linear bending and the Ru-NO stretching modes, respectively. *Interestingly, for complex **2** the DFT calculations predict that ν(Ru-NO) is at higher energy than the linear bends, whereas this order is reversed for complex **4**.* The complex $[Ru(NH_3)_5(NO)]^{3+}$ that we previously studied shows the same energy sequence as **4** as shown in Table 3.17 Importantly, the bending and stretching modes of **4** can be

distinguished using the isotopically labeled data, because in this case, only the nitrogen atom of NO is labeled (^{15}NO). Because of this, the bending mode has a larger isotope shift (predicted: 13 cm^{-1}) than the stretching mode (predicted: 4 cm^{-1}). All assignments are collected in Table 4.3. Note that the frequencies of the N-O stretching modes for complexes **2** and **4** of 1903 and 1930 cm^{-1}, respectively, are again indicative of the Ru(II)-NO^+ ground state description of these complexes.[17]

4.3.4 DFT Calculations on Complex Isomers

Analysis of the four different isomers that $[Ru(TPA)(NO_2)(NO)]^{2+}$ could have with N-bound and O-bound are shown in Table 4.4. The lowest energy structure was found to be N-bound trans to the amine of the TPA ligand (**8b**). The crystallized structure was 1.3 kcal/mol higher in energy than the lowest energy structure **8b**. Most interesting is the large range of NO vibrations ranging from 1878 to 1911 cm^{-1} depending on the binding mode of nitrite. The large range of ν(N-O) vibration was also observed in the crude product of **4**, see above. The highest NO vibration was calculated to be the complexes with water bound, experimentally this was also the case (Table 4.3).

Table 4.5 Quantum yield (ϕ) values and absorption parameters of {Ru-NO}^{6} complexes prepared here.

Complex	Quantum Yield ϕ (λ_{irr}, nm)	Solvent	λ_{max}[b] RuNO, nm (ε, $M^{-1}cm^{-1}$)
2	0.06 ±0.03 (365)	CH_3CN	314 (880)
2	0.03 ±0.02 (365)	DMF	451 (180)
4	0 (365)	CH_3CN	479 (360)
4	0.01 ± 0.002 (365)	DMF	419 (1900)
5	0.007 ± 0.01 (365)	DMF	433 (220)
5	0.002 ± 0.001 (365)	H_2O & oxy-Mb[a]	418 (136000)[c]
[Ru(H_2edta)Cl(NO)] (**6**)	0.004 ± 0.003(365)	H_2O & oxy-Mb[a]	418 (136000) [c]
[Ru(Hedta)(NO)] (**7**)	0.0002 ± 0.0001 (365)	H_2O & oxy-Mb[a]	418 (136000) [c]

[a]Photolablization experiments were performed in H_2O. However, in this case NO rebinding after photorelease of NO is fast, such that no net release of NO is observed upon UV-excitation. To overcome this problem, oxy-Mb is used to trap the NO before it has a chance to rebind to Ru(III).[b] Here λ_{max} is the absorption feature that grows in when NO is released. [c]Extinction coefficient for oxyMb.

4.3.5 NO Photolabilization of {RuNO} Complexes in Organic Solvents

Complexes **2**, **4**, and **5** in their solid states are stable when stored in the dark. Complex **2**, when dissolved in CH_3CN or DMF, is stable in both the dark and ambient light. Complexes **4** and **5**, when dissolved in DMF, are stable in the dark but when exposed to ambient light at room temperature these compounds start to release NO within a few

minutes. Upon irradiation of complex **2** in CH_3CN or DMF, and complexes **4** and **5** in DMF at room temperature with UV-light (365 nm, 10^{-6} - 10^{-7} einsteins min^{-1}), release of NO was observed in each case. The quantum yields for complexes **2**, **4**, and **5** in DMF

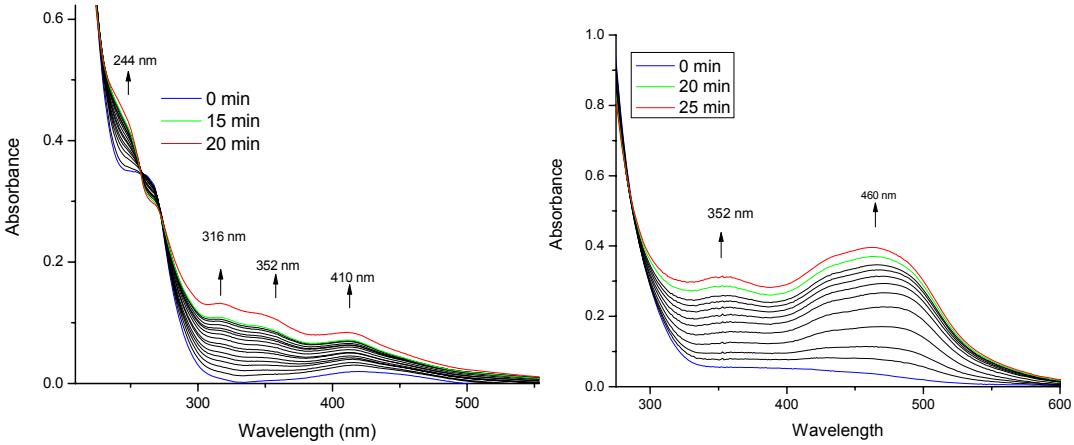

Figure 4.7 UV-Vis absorption spectra of **2** (left) in CH_3CN, 0.05 mM, and **2** (right) in DMF, 0.2 mM. Light intensity: ~1.0 x 10^{-6} einsteins min^{-1}.

were calculated to be 0.03, 0.01 and 0.007, respectively, as listed in Table 4.5. For complex **2**, the release of NO was monitored *via* the appearance of new absorption features at 316, 352 and 410 nm in CH_3CN, and 352 and 461 nm in DMF, respectively, which correspond to MLCT and/or d-d transitions of the Ru(III) photoproduct (*cf.* Figure 3). Quantum yields of complex **2** in acetonitrile and DMF are similar, 0.06 and 0.03, respectively, which is likely due to the fact that these solvents are similar in polarity. On the other hand, complex **4** is not photolabile in CH_3CN, but photolability is observed in DMF upon irradiation with UV-light ($\phi = 0.01$). Here, a change in the absorption spectrum at 451 nm was utilized to track the release of NO. Removal of the nitrite bound to compound **4**, give $[Ru(TPA)(Urea)(NO)](PF_6)_3$ (**5**) which is also photolabile in DMF. The quantum yield for this complex was calculated to be 0.007, which is about an order of magnitude lower than that of **2** and maybe **4**. For complex **5**, changes in the absorption spectrum at 354 and 433 nm were used to track the release of NO.

The release of NO from $\{RuNO\}^6$ complexes generally leads to the formation of a Ru(III)-solvent complex as shown in equation 3.

$$Ru(II)\text{-}NO^{+} + h\nu + solv \longrightarrow Ru(III)\text{-}(solv) + NO\bullet \quad (3)$$

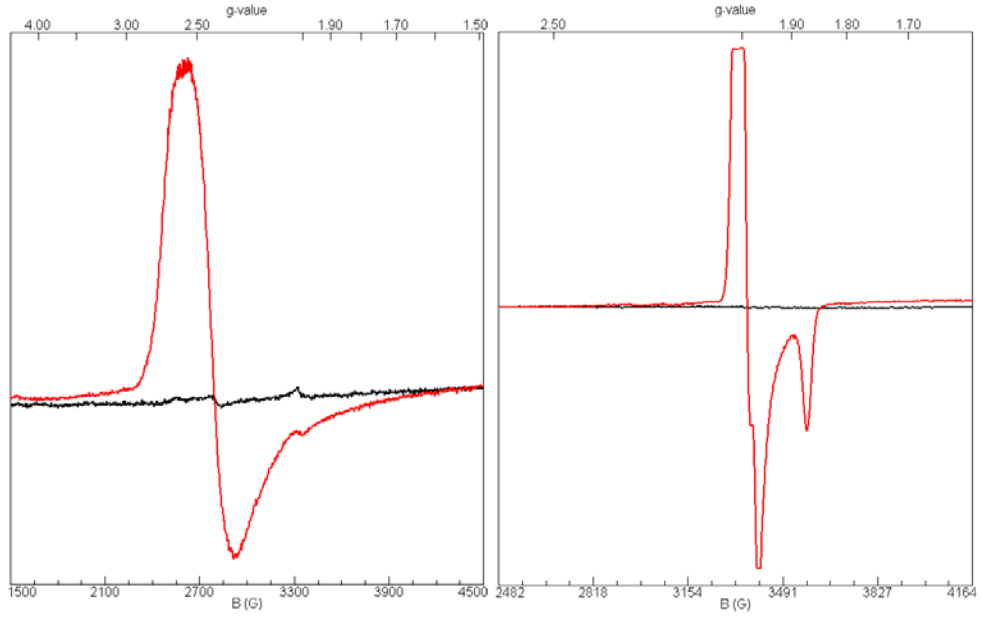

Figure 4.8 Left: Overlay of the EPR spectra of $[Ru(TPA)Cl_2(NO)]ClO_4$ (**2**, black) and its photoproduct $[Ru(TPA)Cl_2(solv)]^{+}$ (red), in a frozen 1:1 mixture of frozen proptionitrile and butyronitrile at 10K. Right: Overlay of the EPR spectra of $[Ru(TPA)(ONO)(NO)](PF_6)_2$ (**4**, black) and its photoproduct $[Ru(TPA)(ONO)(solv)]^{2+}$ (red), obtained in frozen DMF at 10K.

Since the [Ru(III)-(solv)] photoproducts are paramagnetic (S=1/2), the release of NO from the Ru(II)-NO^{+} complexes can also be monitored by EPR spectroscopy. In fact, we observed the EPR signal of a low-spin Ru(III) complex in both photoproducts of complexes **2** and **4**, Figure 4.8 left and right respectively.

4.3.6 NO Photolabilization of {RuNO} Complexes in Water

Complexes $[Ru(H_2edta)Cl(NO)]$ (**6**) and [Ru(Hedta)(NO)] (**7**) were not observed to be photolabile in the solid state when in the dark or in ambient light. These complexes are also stable in aqueous solution in ambient light. When the complexes were irradiated with UV-light in water at pH ~7, no appreciable release of NO was detected *via* UV-Vis absorption spectroscopy, in agreement with reports in the literature that these complexes do not photorelease NO.[62] The Griess assay was also used to detect any nitrite formed in solution after irradiation, but no nitrite was found. In order to test whether the complexes are really not photolabile, or whether rebinding of NO was too fast, oxymyoglobin (oxy-Mb) was then added to the solutions prior to UV irradiation. Here, the formation of

metmyoglobin (met-Mb) from oxy-Mb is used to trap any NO released from the Ru complexes, as shown in equation 4.[90]

$$\text{oxy-Mb} + \text{NO} \longrightarrow \text{met-Mb} + \text{NO}_3^- \qquad (4)$$

The shift in the Soret band from 418 nm (oxy-Mb) to 410 nm (met-Mb) was used to quantify the amount of NO release. One problem with this assay for NO is that oxy-Mb itself is also slightly photolabile, but this reaction can be suppressed by cooling the solution to 0 ^{o}C during UV irradiation and by keeping the intensity of the UV-light low,

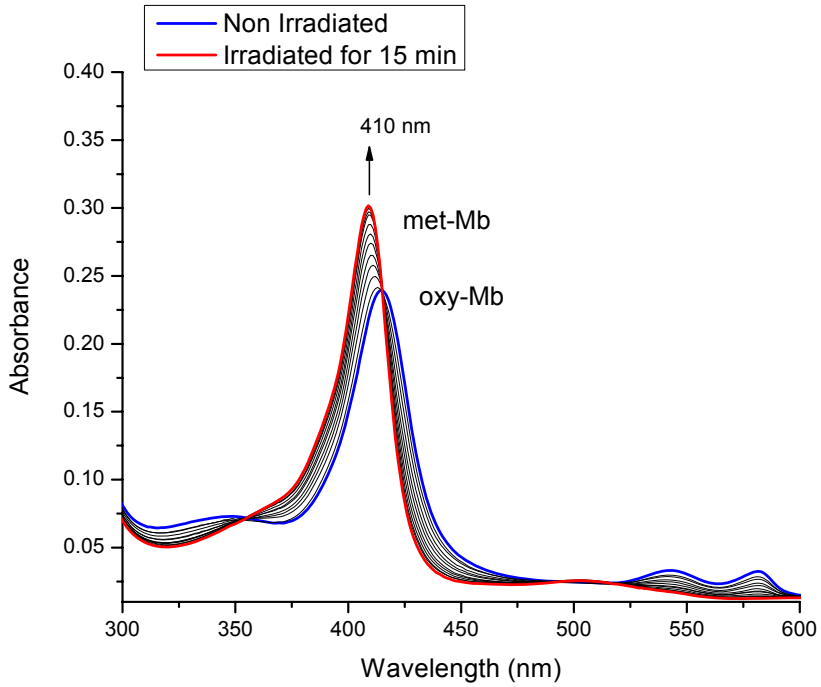

Figure 4.9 UV-Vis absorption spectra of [Ru(H_2edta)(NO)] (7), 0.009 mM, in the presence of oxy-Mb. The Ru:Mb ratio is 5:1. In order to minimize the photooxidation of oxy-Mb, the temperature was kept at 0^{o} C at all times and the intensity of light was kept at ~4.0 x 10^{-7} einstein min^{-1}.[89]

around 10^{-6} and 10^{-7} einstein min^{-1}.[91] Importantly, these experiments show that complexes **6** and **7** are in fact photolabile (*cf.* Figure 4). However, the quantum yields of these complexes are really low, and were calculated to be 0.004 and 0.0002 for **6**, and **7**, respectively, as shown in Table 4.5. In addition, we investigated the photolabilization of the water-soluble complex **5** in water for comparison. The quantum yield in this case was determined to be 0.002, which is distinctively lower compared to the photolabilization of this complex in DMF (0.007, see above).

4.4 Discussion

The ruthenium-nitrosyl complexes **2**, **4**, **5**, **6**, and **7** all have $\{RuNO\}^6$ electronic structures. Vibrational and ^{1}H-NMR spectroscopy confirm the similarity in the electronic structure, $\{RuNO\}^6$, of the Ru-NO units in these complexes, showing diagnostic N-O stretching frequencies ranging from 1890 - 1930 cm^{-1}. The Ru-N stretching modes and Ru-N-O bending modes were identified using FT-Raman spectroscopy and assigned in comparison to DFT calculations. For example, the RuNO bending mode of complex **2** is assigned to 585 cm^{-1} which is 34 cm^{-1} lower than the Ru-N stretching mode at 619 cm^{-1}. Interestingly, this is contrary to the assignment of the bending and stretching mode of other Ru-NO complexes (**4**, **5** and $[Ru(NH_3)_5(NO)]^{3+}$) where the stretching mode is lower in energy than the bending mode (*cf.* Table 4.3). The Ru-NO stretch (619 cm^{-1}) shows a distinctively larger intensity in the Raman spectrum as compared with the Ru-N-O bending mode (585 cm^{-1}) for **2** (*cf.* Figure 4.3), which is in agreement with previous assignments of the Ru-NO stretching and Ru-N-O bending modes in $[Ru(NH_3)_5(NO)]^{3+}$.[17]

The photolabilization of complexes **6** and **7** was previously reported to not lead to the release of NO. However, using a myoglobin based assay we were able to show that complexes **6** and **7** actually photolabilize the ruthenium-nitrosyl bond. When adding oxy-Mb to the Ru-NO solutions complexes **6** and **7** were found to have quantum yields of 0.004 and 0.0002, respectively, when irradiated with UV-light. Although these complexes are only slightly photolabile, the release of NO is observed. In addition to the photolabilization of the edta water-soluble complexes, a {Ru(TPA)(NO)} complex, **5**, was also photolabilized in buffer and oxy-Mb. This complex was found to release NO in the Mb solution with a quantum yield of 0.002. In contrast, when photolabilized in DMF, complex **5** has a quantum yield of 0.007, which is almost four times larger in the organic solvent as the aqueous solution. Although $[Ru(TPA)(Urea)(NO)]^{3+}$ (**5**) releases more NO in DMF than in an aqueous environment, other Ru-NO complexes, $[Ru(PaPy_3)(NO)]^{2+}$ and $[Ru(PaPy_2Q)(NO)]^{2+}$, have shown the opposite trend.[15]

It is interested to note that the water insoluble complex **2**, $[Ru(TPA)Cl_2(NO)]^+$, has the largest quantum yield of all complexes analyzed here. In CH_3CN and DMF the

quantum yield of **2** is 0.06 and 0.03, respectively. Overall complex **2** has a higher quantum yield than the other complexes, **4** and **5**, in DMF.

4.5 Conclusion

The photolability of a number or ruthenium-nitrosyl complexes was analyzed in both aqueous and organic solvents. We found that water-soluble complexes $[Ru(TPA)(Urea)(NO)]^{3+}$, $[Ru(H_2edta)(NO)]$ and $[Ru(Hedta)(NO)]$ were slightly photolabile in a water and myoglobin solution. A myoglobin based assay was used to show that "non-photolabile" complexes were in fact photolabile.[61] In addition to photolabilizing ruthenium-nitrosyl complexes in aqueous solutions, organic solvents such as DMF and CH_3CN were used to analyze the photolability of water-insoluble ruthenium nitrosyls. The ruthenium-nitrosyl complexes photolabilized in organic solvents had higher quantum yields than the complexes in aqueous solutions. In conclusion, photolabilization of ruthenium-nitrosyl complexes in aqueous solutions may not increase the amount of NO released into the solvent. So water is not a particularly good solvent for the photolabilization of NO, which is a potential obstacle for the development of corresponding PDT agents. The myoglobin assay is a good method for an accurate determination of the quantum yield of NO release in ruthenium-nitrosyl complexes, as it prevents the trapping of NO by the formed Ru(III) complex.

4.6 Appendix

In addition to studying the photolabilization of TPA and edta, other multidentate ligands were synthesized and characterized to investigate the photolabilization of ruthenium-nitrosyl complexes. The synthesis and preliminary characterization of ruthenium complexes bound to N,N-bis(2-pyridylmethyl)amine acetate (BMPA-Ac), N,N-bis(2-pyridylmethyl)-N-(bis-2-pyridylmethyl)amine) (N4Py), and N, N-bis(2-pyridylmethyl)-aminomalonate (N2Py2O) are discussed here.

4.6.1 Experimental

4.6.1.1 Synthesis of [Ru(BMPA-Ac)Cl(NO)]Cl

Using the reactions shown in Scheme 4.2, the synthesis of [Ru(BMPA-Ac)Cl(NO)]Cl was accomplished.

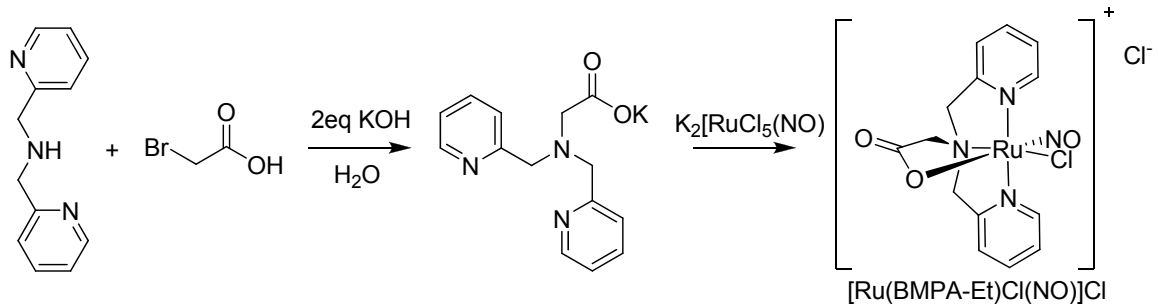

Scheme 4.2 Synthetic scheme of [Ru(BMPA-Ac)Cl(NO)]Cl.

The synthesis of K(BMPA-Ac) was based on slightly modified literature procedures.[92-93] First, bis[(2-pyridyl)methyl]amine (420 mg, 2 mmol) was added to 2 mL of water and bromoacetic acid (275 mg, 2 mmol) and stirred. A separate solution of potassium hydroxide (208 mg, 3.7 mmol) in 3 mL of water was created and added dropwise to the other solution. The reaction mixture was stirred under nitrogen for 2 days. The reaction mixture went from a yellow to dark brown. The water was removed *via* vacuum distillation and the resulting oil was dissolved in methanol and filtered. The methanol was removed by rotoevaporation and the solid was washed with acetonitrile and collected. Yield: 500 mg (92%). ^{1}H-NMR (D_2O, ppm) 8.24 (2H, d, J(H,H) = 4.2 Hz, H-Py,), 7.82 (2H, t, J(H,H) = 5.8 Hz, H-Py), 7.51 (2H, d, J(H,H) = 7.6 Hz, H-Py), 7.49 (2H, t, J(H,H) = 4.8 Hz, H-Py), 4.06 (4H, s, CH_2-Py), 3.40 (2H, s, CH_2-COOK).

The ruthenium-nitrosyl, [Ru(BMPA-Ac)Cl(NO)]Cl, was synthesized by reacting $K_2[RuCl_5(NO)]$ (65 mg, 0.17 mmol) with the K(BMPA-Ac) (50 mg, 0.17 mmol) in 10 mL of water. The reaction mixture was refluxed for 2 hours and the water removed *via* vacuum distillation. The solid was dissolved in methanol, then diethyl ether was added to the solution to precipitate and collect the compound. Yield: 77 mg (95%). Selected IR frequencies (KBr disk, cm^{-1}) 1890 (ν(N-O)) as shown in Figure 4.10. LCT-MS: m/z 422.9 $[Ru(BMPA\text{-}Ac)Cl(NO)]^+$.

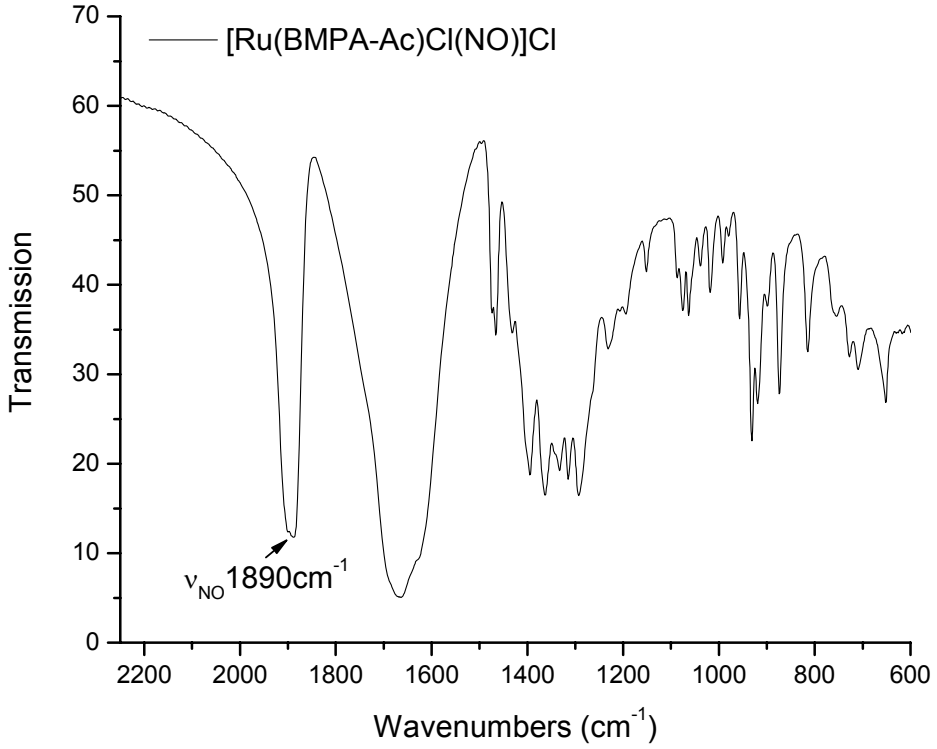

Figure 4.10 IR spectrum of [Ru(BMPA-Ac)Cl(NO)]Cl in KBr.

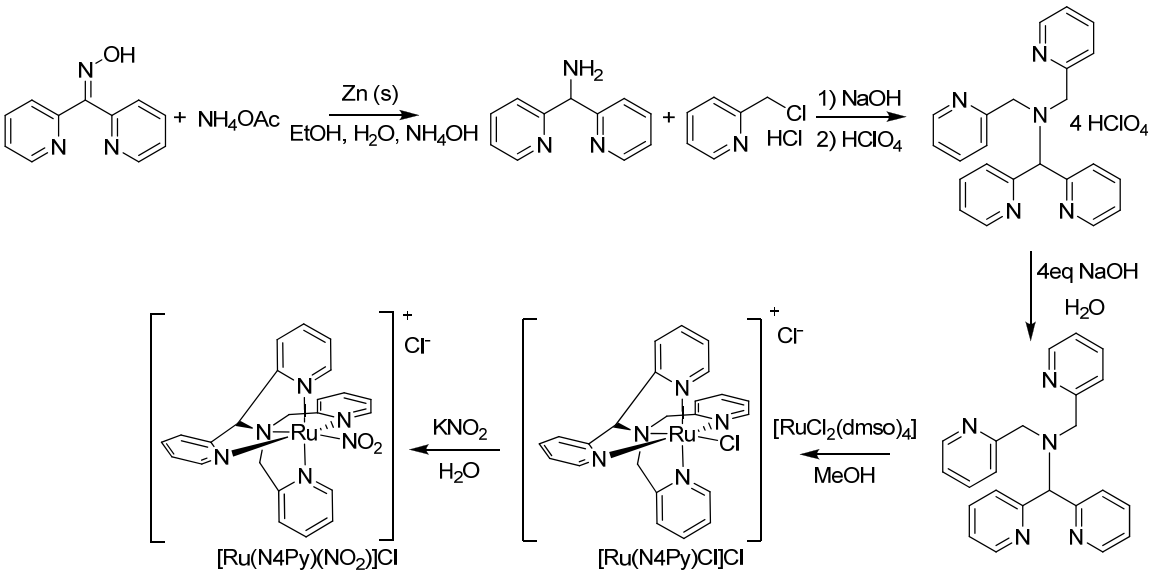

Scheme 4.3 Synthetic scheme of [Ru(N4Py)(NO_2)]Cl.

4.6.1.2 Synthesis of $[Ru(N4Py)(NO_2)]Cl_2$

Using the reactions shown in Scheme 4.3, the synthesis of $[Ru(N4Py)(NO_2)]Cl_2$ was accomplished.

The ligand $N4Py{\bullet}4HClO_4$ was synthesized using literature procedures.[94-95] Di(2-pyridyl)methylamine was synthesized by reacting ketone oxime (0.50 g, 2.5 mmol) in 8.5 mL ethanol and 5 mL water with 7.5 mL ammonium hydroxide. The reaction was heated under argon at 80°C while zinc powder (0.74 g, 11.3 mmol) was added over 30 minutes. The reaction was heated for another 4.5 hours. The solution was filtered to remove excess zinc and the solution was concentrated down to an oil. 10 mL of 10M sodium hydroxide was added to the solution. The amine was extracted from the aqueous layer by dichloromethane, which was washed with brine and dried *via* magnesium sulfate. Yield: 0.354g (76 %). ^{1}H-NMR ($CDCl_3$, ppm) 8.53 (2H, d, J(H,H) = 4.8 Hz, H-Py), 7.60 (2H, t, J(H,H) = 7.5 Hz, H-Py), 7.36 (2H, d, J(H,H) = 7.8 Hz, H-Py), 7.11 (2H, t, J(H,H) = 4.7 Hz, H-Py), 5.30 (1H, s, CH), 2.41 (2H, br s, NH).

$N4Py{\bullet}4HClO_4$ was synthesized by reacting picolyl chloride hydrochloride (1.354 g, 8.26 mmol) with 2 mL of 5M sodium hydroxide. To this solution di(2-pyridyl)methylamine (0.763g, 4.12 mmol) was added and stirred for 24 hours. To this solution $HClO_4$ was added to precipitate out the yellow $N4Py{\bullet}4HClO_4$. The yellow solid was washed with ethanol and collected. Yield: 1.023 g (32 %).

The neutral N4Py was synthesized by reacting $N4Py{\bullet}4HClO_4$ (470 mg, 0.62 mmol) in 10 mL of water with excess sodium hydroxide, 20 mL of a 2.5 M solution, by dropwise additions. The reaction turned from yellow to pink. The neutral N4Py was extracted from the water layer with dichloromethane. The solvent was evaporated and the oil collected. Yield: 175 mg (78%). ^{1}H-NMR ($CDCl_3$, ppm) 8.57 (2H, d, J(H,H) = 4.7 Hz, H-Py), 8.51 (2H, d, J(H,H) = 4.8 Hz, H-Py), 7.63 (8H, m, H-Py), 7.13 (4H, m, H-Py), 5.35 (1H, s, CH), 3.97 (4H, s, CH_2).[94]

The $[Ru(N4Py)Cl]Cl$ precursor was synthesized by reacting $[Ru(dmso)_4Cl_2]$ (320 mg, 0.66 mmol) with the N4Py (175 mg, 0.48 mmol) in 35 mL of methanol and refluxed for 27 hours. The reaction was cooled and the methanol was removed *via* rotoevaporation and the oil was dissolved in a small amount of hot methanol. Diethyl ether was added to precipitate out red $[Ru(N4Py)Cl]Cl$. Yield: 41 mg (16%).^{1}H-NMR ($CDCl_3$, ppm) 9.43-

9.417 (2H, d, J(H,H) = 4.5 Hz, H-Py), 9.06-9.05 (2H, d, J(H,H) = 4.7 Hz, H-Py), 8.04-8.02 (2H, d, J(H,H) = 7.8 Hz, H-Py), 7.75-7.70 (2H, t, J(H,H) = 6.2 Hz, H-Py), 7.46-7.42 (2H, t, J(H,H) = 6.3 Hz, H-Py), 7.19-7.10 (4H, dt, J(H,H) = 6.5, 1.2 Hz, H-Py), 7.14-7.10 (2H, d, J(H,H) = 6.8 Hz, H-Py), 4.67-4.38 (4H, ddki, J(H,H) = 18.5 Hz, H_2C-Py), 3.46 (1H, s, $CHPy_2$).

Finally, the synthesis of the ruthenium-nitrosyl precursor, $[Ru(N4Py)(NO_2)]^+$ was achieved by reacting 10 mg (0.02 mmol) of [Ru(N4Py)Cl]Cl with 6 mg (0.07 mmol) of potassium nitrite in 3 mL of water. The solution was refluxed for 4 hours and the solvent removed by vacuum distillation. The obtained solid was dissolved in methanol and filtered to obtain a small amount (~1 or 2 mg) of a dark brown/black solid, that is believed to be $[Ru(N4Py)(NO)]^{3+}$ due to an IR frequency observed at 1840 cm^{-1} (ν(N-O)) as seen in Figure 4.13. The calculated IR frequency for [Ru(N4Py)(NO)] is 1921 cm^{-1}. The expected product, $[Ru(N4Py)(NO_2)]^+$ was not isolated from solution or further characterized.

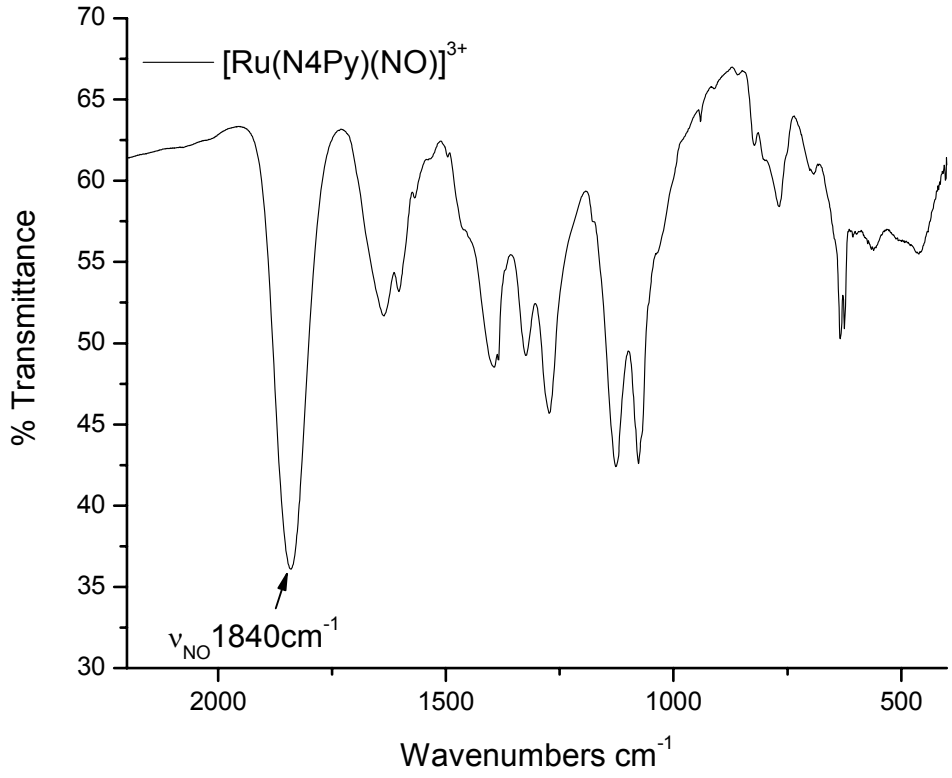

Figure 4.11 IR spectrum of $[Ru(N4Py)(NO)]^{3+}$ in KBr.

4.6.1.3 Synthesis of [Ru(N2Py2O)(dmso)]

Using the reactions shown in Scheme 4.4 the synthesis of [Ru(N2Py2O)(dmso)] was accomplished.

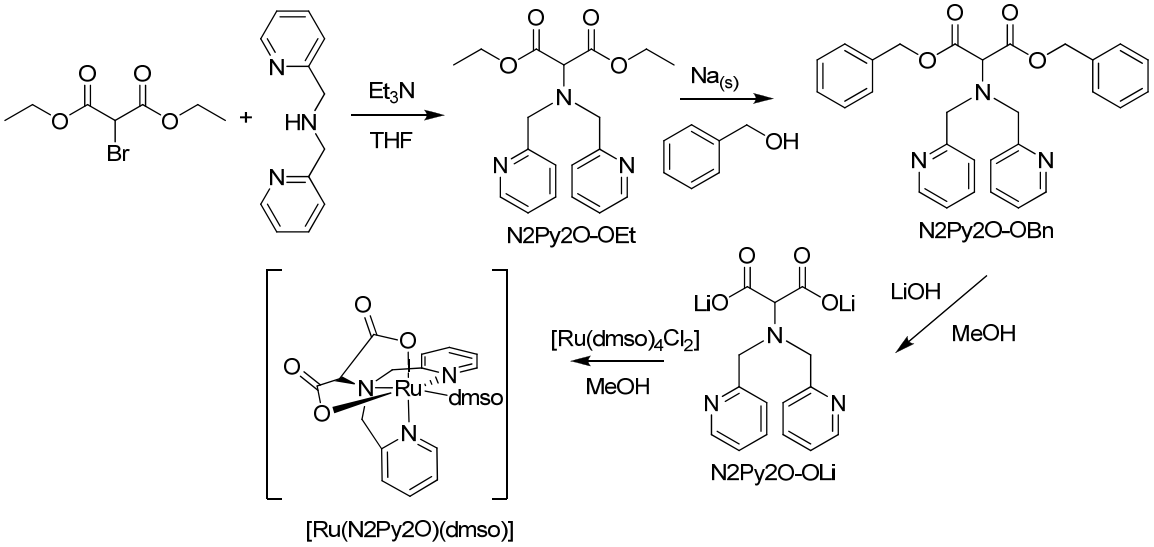

Scheme 4.4 Synthetic scheme of [Ru(N2Py2O)(dmso)].

The ligand N2Py2O-OLi was synthesized in three steps. First, N2Py2O-OEt was synthesized by reacting diethyl bromomalonate (1.02 g, 4.27 mmol) with 2,2'-dipicolylamine (1.0 g, 5.0 mmol) in 2 mL of THF and heated for 1 hour at 45° C. A precipitate formed and then triethylamine (0.5 g, 4.9 mmol) in 8 mL of THF was added and the reaction was refluxed for 30 hours. The solvent was removed to produce an orange/brown oil. Yield: 1.49g (98%). ^{1}H-NMR ($CDCl_3$, ppm) 8.41 (2H, d, J(H,H) = 2.3 Hz, H-Py), 7.56 (4H, d, J(H,H) = 4.8 Hz, H-Py), 7.04 (2H, t, J(H,H) = 1.9 Hz, H-Py), 4.26 (1H, s, CH-COOEt), 4.18 (4H, q, J(H,H) = 7.2 Hz, -CH_2-O), 4.06 (4H, s, CH_2-Py), 1.22 (6H, t, J(H,H) = 7.3 Hz, CH_3-CH_2) LCT-MS: m/z 358.1 N2Py2O-OEt.

N2Py2O-OBn was synthesized by reacting the crude N2Py2O-OEt (0.47 g, 1.32 mmol) with dried and distilled benzyl alcohol (0.75 mL, 7.25 mmol) and small pieces of sodium in a bomb flask. A vacuum was placed on the flask and the depressurized reaction was refluxed for 20 hours. The benzyl alcohol was removed *via* the Schlenk line to form a dark brown oil. A silica gel column with 100% ethyl acetate was run and fractions collected. The fractions were analyzed by TLC and combined accordingly. The solvent was removed to produce N2Py2O-OBn as a brown oil. Yield: 0.44 g (69%). ^{1}H-NMR

($CDCl_3$, ppm) 8.43 (2H, d, J(H,H) = 4.9 Hz, H-Py), 7.53 (2H, t, J(H,H) = 5.7 Hz, H-Py), 7.47 (2H, d, J(H,H) = 7.8 Hz, H-Py), 7.25 (10H, s, H-Bn), 7.07 (2H, t, J(H,H) = 3.9 Hz, H-Py), 5.14 (4H, s, CH_2-Bn), 4.09 (4H, s, CH_2-Py). LCT-MS: m/z 482.2 N2Py2O-OBn, 504.1 N2Py2O-OBn + Na^+.

The N2Py2O-OLi salt was synthesized by reacting the purified N2Py2O-OBn (1.4 g, 3.0 mmol) with lithium hydroxide (0.146 g, 6.1 mmol) in 13 mL of methanol. This solution was stirred for 1 week. A silica gel plug was run with 100% ethyl acetate to remove any contaminants from the N2Py2O-OLi. After removing the contaminants the plug was run with 100% methanol and this solution was collected. The solvent was removed in vacuo to obtain pure N2Py2O-OLi. Yield: 0.35 g (36%). ^{1}H-NMR (D_2O) 8.06 (2H, d, J(H,H) = 4.5 Hz, H-Py), 7.36 (2H, t, J(H,H) = 6.3 Hz, H-Py), 7.03 (2H, d, J(H,H) = 7.8 Hz, H-Py), 6.91 (2H, t, J(H,H) = 5.7 Hz, H-Py), 4.35 (1H, s, CH-COOLi), 3.69 (4H, s, CH_2-Py).

Finally, to produce [Ru(N2Py2O)(dmso)] similar conditions to the synthesis of [Ru(N4Py)Cl] were used. N2Py2O-OLi (0.20 g, 0.64 mmol) and [$Ru(dmso)_4Cl_2$] (0.29 g, 0.60 mmol) were combined in 35 mL of methanol and refluxed for 26 hours. The reaction was cooled and the solvent removed to produce a brown oil. The brown oil was dissolved in a small amount of hot methanol and layered with cold diethyl ether. Orange crystals were obtained as described in literature.[96] Yield: 5 mg (2%). The crystals were not further characterized.

4.6.2 Results and Discussion

4.6.2.1 [Ru(BMPA-Ac)Cl(NO)]Cl

In order to synthesize the ruthenium-nitrosyl [Ru(BMPA-Ac)Cl(NO)]Cl, the ligand KBMPA-OEt was synthesized by stirring bis[(2-pyridyl)methyl]amine, bromoacetic acid and potassium hydroxide for two days or until the reaction is complete as tested by TLC. The potassium salt was then reacted with the ruthenium-nitrosyl, $K_2[RuCl_5(NO)]$, to form [Ru(BMPA-Ac)Cl(NO)]Cl. Using MidIR, the NO vibration of this complex was found at 1890 cm^{-1}. The ruthenium nitrosyl complex was irradiated with UV-light and found to release NO when in acetonitrile. The release of NO was monitored *via* the appearance of new absorption bands at 365 and 480 nm. This change in the UV-Vis spectrum

constitutes only a minor change, which could be indicative of an efficient back reaction in acetonitrile (Figure 4.13). Further reactions in other solvents could decrease this possible back reaction. In addition, photolabilization of this complex should be attempted in water using oxy-Mb to trap the released NO.

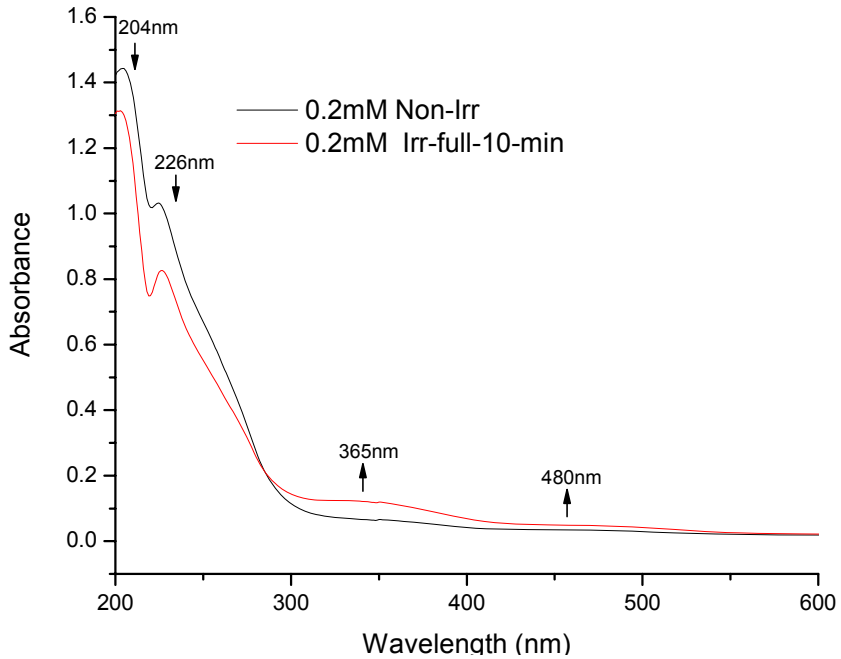

Figure 4.12 UV-Vis absorption spectra of [Ru(BMPA-Ac)Cl(NO)]Cl in CH_3CN when irradiated with UV-light.

4.6.2.2 [Ru(N4Py)(NO_2)]Cl

[Ru(N4Py)Cl]Cl was synthesized using a combination of literature procedures.[94-96] This ruthenium complex was obtained by refluxing the ruthenium(II) precursor [Ru(dmso)$_4$Cl] with N4Py in methanol for 27 hours. Pure [Ru(N4Py)Cl]Cl was crystallized from the crude oil and reacted with potassium nitrite. A black precipitate was collected in a very low yield (~2%) and found to have an NO vibration at 1840 cm^{-1}. Since the minor product could be [Ru(N4Py)(NO)]Cl_3, further analysis of the reaction with nitrite is needed. The majority of the product is likely [Ru(N4Py)(NO_2)]Cl, which, however, likely remained in solution and was not isolated.

4.6.2.3 [Ru(N2Py2O)(dmso)]

The ligand N2Py2O-OLi was synthesized through a number of steps. First, N2Py2O-OEt was obtained by the reaction of diethyl bromomalonate and 2,2' dipicolylamine with a weak base, triethylamine. Although at this stage a silica gel column could be run to purify N2Py2O-OEt, another column is needed to purify the N2Py2O-OBn from the following step, so the first column was omitted in favor of running one column only. N2Py2O-OBn was synthesized by a trans-esterification of the diethyl malonate ester with benzyl alcohol and sodium metal. The excess benzyl alcohol was distilled from the reaction mixture to yield a brown oil. The crude N2Py2O-OBn was purified by running a silica gel column with 100% ethyl acetate as the eluent. The pure N2Py2O-OBn was finally reacted with lithium hydroxide to form the anionic $N2Py2O^{2-}$ ligand. In order to purify N2Py2O-OLi, a silica gel plug was first run with ethyl acetate to remove remaining benzyl alcohol and any other impurities, then the plug was flushed with methanol to remove the purified product from the silica gel. In order to form the ruthenium complex, the Ru(II)-precursor $[Ru(dmso)_4Cl_2]$ was reacted with N2Py2O-OLi and refluxed in methanol for over 24 hours. Crystals of the product [Ru(N2Py2O)(dmso)] were formed by dissolving the crude product in a small amount of hot methanol and carefully layering cold diethyl ether on top. Gradually, orange crystals were formed in low yield. These crystal were X-ray quality crystals, however, the crystal structure of [Ru(N2Py2O)(dmso)] was determined by Yamaguchi et al.[96] The complex was not further characterized.

4.6.3 Conclusions

The synthesis of a variety of multidentate ligands was accieved in order to form other ruthenium-nitrosyl complexes. The synthesis of the ligands, N,N-bis(2-pyridylmethyl)amine acetate (BMPA-Ac), N,N-bis(2-pyridylmethyl)-N-(bis-2-pyridylmethyl)amine) (N4Py), and N, N-bis(2-pyridylmethyl)-aminomalonate (N2Py2O), was achieved to compare photolability of these ligands to the previously discussed ruthenium-nitrosyl complexes. Although the ruthenium-nitrosyl complexes were not synthesized the difference in photolability between all of the different ruthenium-nitrosyls would be interesting to observe how different ligands affect the water-solubility and photolability.

4.7 References

(1) Furchgott, R. F. *Angew. Chem., Int. Ed. Engl.* **1999**, *38*, 1870-1880.

(2) Ignarro, L. J. *Angew. Chem., Int. Ed. Engl.* **1999**, *38*, 1882-1892.

(3) Murad, F. *Angew. Chem., Int. Ed. Engl.* **1999**, *38*, 1857-1868.

(4) Fang, F. C. *Nitric Oxide and Infection*; Kluwer Academic/Plenum Publishers: New York, 1999.

(5) Kanwar, J. R.; Kanwar, R. K.; Burrow, H.; Baratchi, S. *Curr. Med. Chem.* **2009**, *16*, 2373-2394.

(6) Hirst, D.; Robson, T. *J. Pharm. Pharmacol.* **2007**, *59*, 3-13.

(7) Rose, M. J.; Mascharak, P. K. *Curr. Opin. Chem. Biol.* **2008**, *12*, 238-244.

(8) Chen, J.; Keltner, L.; Christopherson, J.; Zheng, F.; Krouse, M.; Singhal, A.; Wang, S. S. *Cancer J.* **2002**, *8*, 154-163.

(9) Ford, P. C.; Bourassa, J.; Miranda, K.; Lee, B.; Lorkovic, I.; Boggs, S.; Kudo, S.; Laverman, L. *Coord. Chem. Rev.* **1998**, *171*, 185-202.

(10) Mascharak, P. K.; Eroy-Reveles, A. A. *Future Med. Chem.* **2009**, *1*, 1497-1507.

(11) Hamblin, M. R.; Castano, A. P.; Mroz, P. *Nat. Rev. Cancer* **2006**, *6*, 535-545.

(12) Detty, M. R.; Gibson, S. L.; Wagner, S. J. *J. Med. Chem.* **2004**, *47*, 3897-3915.

(13) Ghosh, K.; Eroy-Reveles, A. A.; Avila, B.; Holman, T. R.; Olmstead, M. M.; Mascharak, P. K. *Inorg. Chem.* **2004**, *43*, 2988-2997.

(14) Hoffman-Luca, C. G.; Eroy-Reveles, A. A.; Alvarenga, J.; Mascharak, P. K. *Inorg. Chem.* **2009**, *48*, 9104-9111.

(15) Rose, M. J.; Mascharak, P. K. *Coord. Chem. Rev.* **2008**, *252*, 2093-2114.

(16) Enemark, J. H.; Feltham, R. D. *Coord. Chem. Rev.* **1974**, *13*, 339-406.

(17) Paulat, F.; Kuschel, T.; Nather, C.; Praneeth, V. K. K.; Sander, O.; Lehnert, N. *Inorg. Chem.* **2004**, *43*, 6979-6994.

(18) Praneeth, V. K. K.; Paulat, F.; Berto, T. C.; George, S. D.; Nather, C.; Sulok, C. D.; Lehnert, N. *J. Am. Chem. Soc.* **2008**, *130*, 15288-15303.

(19) Bottomley, F. *Coord. Chem. Rev.* **1978**, *26*, 7-32.

(20) Bottomley, F. *Acc. Chem. Res.* **1978**, *11*, 158-163.

(21) Averill, B. A. *Chem. Rev.* **1996**, *96*, 2951-2964.

(22) Linder, D. P.; Rodgers, K. R.; Banister, J.; Wyllie, G. R. A.; Ellison, M. K.; Scheidt, W. R. *J. Am. Chem. Soc.* **2004**, *126*, 14136-14148.

(23) Roncaroli, F.; Videla, M.; Slep, L. D.; Olabe, J. A. *Coord. Chem. Rev.* **2007**, *251*, 1903-1930.

(24) Goodrich, L. E.; Paulat, F.; Praneeth, V. K. K.; Lehnert, N. *Inorg. Chem.* **2010**, *49*, 6293-6316.

(25) Soldatova, A. V.; Ibrahim, M.; Olson, J. S.; Czernuszewicz, R. S.; Spiro, T. G. *J. Am. Chem. Soc.* **2010**, *132*, 4614-4625.

(26) Tfouni, E.; Krieger, M.; McGarvey, B. R.; Franco, D. W. *Coord. Chem. Rev.* **2003**, *236*, 57-69.

(27) Lehnert, N.; Berto, T. C.; Galinato, M. G. I.; Goodrich, L. E. *The Role of Heme-Nitrosyls in the Biosynthesis, Transport, Sensing, and Detoxificcation of Nitric Oxide (NO) in Biological Systems: Enzymes and Model Complexes; in "The Handbook of Porphyrin Science"*; World Scientific: Singapore, 2011; Vol. 14, Page 1-247 (Chapter 63).

(28) Merkle, A. C.; Fry, N. L.; Mascharak, P. K.; Lehnert, N. *Inorg. Chem.* **2011**, *50*, 11504-11506.

(29) Patra, A. K.; Afshar, R.; Olmstead, M. M.; Mascharak, P. K. *Angew. Chem., Int. Ed. Engl.* **2002**, *41*, 2512-2515.

(30) Eroy-Reveles, A. A.; Hoffman-Luca, C. G.; Mascharak, P. K. *Dalton T.* **2007**, 5268-5274.

(31) Patra, A. K.; Mascharak, P. K. *Inorg. Chem.* **2003**, *42*, 7363-7365.

(32) Rose, M. J.; Olmstead, M. M.; Mascharak, P. K. *Polyhedron* **2007**, *26*, 4713-4718.

(33) Franco, D. W.; Carlos, R. M.; Cardoso, D. R.; Castellano, E. E.; Osti, R. Z.; Camargo, A. J.; Macedo, L. G. *J. Am. Chem. Soc.* **2004**, *126*, 2546-2555.

(34) Franco, D. W.; Borges, S. D. S.; Davanzo, C. U.; Castellano, E. E.; Z-Schpector, J.; Silva, S. C. *Inorg. Chem.* **1998**, *37*, 2670-2677.

(35) Franco, D. W.; Toledo, J. C.; Neto, B. D. S. L. *Coord. Chem. Rev.* **2005**, *249*, 419-431.

(36) Franco, D. W.; Lopes, L. G. F.; Castellano, E. E.; Ferreira, A. G.; Davanzo, C. U.; Clarke, M. J. *Inorg. Chim. Acta* **2005**, *358*, 2883-2890.

(37) da Silva, R. S.; Oliveira, F. D.; Ferreira, K. Q.; Bonaventura, D.; Bendhack, L. M.; Tedesco, A. C.; Machado, S. D.; Tfouni, E. *J. Inorg. Biochem.* **2007**, *101*, 313-320.

(38) Ford, P. C.; Works, C. F.; Jocher, C. J.; Bart, G. D.; Bu, X. H. *Inorg. Chem.* **2002**, *41*, 3728-3739.

(39) Ford, P. C.; Works, C. F. *J. Am. Chem. Soc.* **2000**, *122*, 7592-7593.

(40) Mascharak, P. K.; Patra, A. K.; Olmstead, M. M. *Inorg. Chem.* **2002**, *41*, 5403-5409.

(41) Mascharak, P. K.; Halpenny, G. M.; Olmstead, M. M. *Inorg. Chem.* **2007**, *46*, 6601-6606.

(42) de Lima, R. G.; Sauaia, M. G.; Bonaventura, D.; Tedesco, A. C.; Bendhack, L. M.; da Silva, R. *Inorg. Chim. Acta* **2006**, *359*, 2543-2549.

(43) da Silva, R. S.; de Lima, R. G.; Sauaia, M. G.; Bonaventura, D.; Tedesco, A. C.; Lopez, R. F. V.; Bendhack, L. M. *Inorg. Chim. Acta* **2005**, *358*, 2643-2650.

(44) da Silva, R. S.; Sauaia, M. G.; de Lima, R. G.; Tedesco, A. C. *J. Am. Chem. Soc.* **2003**, *125*, 14718-14719.

(45) Mascharak, P. K.; Rose, M. J.; Olmstead, M. M. *J. Am. Chem. Soc.* **2007**, *129*, 5342-5343.

(46) da Silva, R. S.; Sauaia, M. G.; de Lima, R. G.; Tedesco, A. C. *Inorg. Chem.* **2005**, *44*, 9946-9951.

(47) Sizova, O. V.; Lyubimova, O. O. *Russ. J. Gen. Chem.* **2004**, *74*, 996-1000.

(48) Sizova, O. V.; Ivanova, N. V.; Sizov, V. V.; Nikol'skii, A. B. *Russ. J. Gen. Chem.* **2004**, *74*, 481-485.

(49) Sizova, O. V.; Ivanova, N. V.; Lyubimova, O. O.; Nikol'skii, A. B. *Russ. J. Gen. Chem.* **2004**, *74*, 155-163.

(50) Lever, A. B. P.; Gorelsky, S. I.; da Silva, S. C.; Franco, D. W. *Inorg. Chim. Acta* **2000**, *300*, 698-708.

(51) Ford, P. C.; Wecksler, S. R.; Hutchinson, J. *Inorg. Chem.* **2006**, *45*, 1192-1200.

(52) Tan, L. S.; Wecksler, S. R.; Mikhailovsky, A.; Korystov, D.; Buller, F.; Kannan, R.; Ford, P. C. *Inorg. Chem.* **2007**, *46*, 395-402.

(53) Mascharak, P. K.; Fry, N. L.; Heilman, B. J. *Inorg. Chem.* **2011**, *50*, 317-324.

(54) Eroy-Reveles, A. A.; Leung, Y.; Beavers, C. M.; Olmstead, M. M.; Mascharak, P. K. *J. Am. Chem. Soc.* **2008**, *130*, 4447-4458.

(55) Eroy-Reveles, A. A.; Leung, Y.; Mascharak, P. K. *J. Am. Chem. Soc.* **2006**, *128*, 7166-7167.

(56) Anderegg, G.; Wenk, F. *Helv. Chim. Acta* **1967**, *50*, 2330-2332.

(57) Gafford, B. G.; Holwerda, R. A. *Inorg. Chem.* **1989**, *28*, 60-66.

(58) James, B. R.; Ochiai, E.; Rempel, G. I. *Inorg. Nucl. Chem. Lett.* **1971**, *7*, 781-784.

(59) Kojima, T.; Amano, T.; Ishii, Y.; Ohba, M.; Okaue, Y.; Matsuda, Y. *Inorg. Chem.* **1998**, *37*, 4076-4085.

(60) Wolny, J. A.; Bjernemose, J.; Hazell, A.; McKenzie, C. J.; Mahon, M. F.; Nielsen, L. P.; Raithby, P. R.; Simonsen, O.; Toftlund, H. *Polyhedron* **2003**, *22*, 875-885.

(61) Diamantis, A. A.; Dubrawski, J. V. *Inorg. Chem.* **1981**, *20*, 1142-1150.

(62) Franco, D. W.; Zanichelli, P. G.; Miotto, A. M.; Estrela, H. F. G.; Soares, F. R.; Grassi-Kassisse, D. M.; Spadari-Bratfisch, R. C.; Castellano, E. E.; Roncaroli, F.; Parise, A. R.; Olabe, J. A.; de Brito, A. R. M. S. *J. Inorg. Biochem.* **2004**, *98*, 1921-1932.

(63) Sheldrick, G. M. *SADABS, v. 2008/1, Program for Empirical Absorption Correction of Area Detector Data* University of Gottingen: Gottingen, Germany, 2008.

(64) Sheldrick, G. M. *SHELXTL, v. 2008/3* Bruker Analytical X-ray:Maditon, WI, 2008.

(65) *Saint Plus, c. 7.53a* Bruker Analytical X-ray: Madison, WI, 2008.

(66) Perdew, J. P. *Phys. Rev. B* **1986**, *33*, 8822-8824.

(67) Becke, A. D. *J. Chem. Phys.* **1986**, *84*, 4524-4529.

(68) Frisch, M. J.; Trucks, G. W.; Schlegel, H. B.; Scuseria, G. E.; Robb, M. A.; Cheeseman, J. R.; Montgomery, J. A., Jr.; Vreven, T.; Kudin, K. N.; Burant, J. C.; Millam, J. M.; Iyengar, S. S.; Tomasi, J.; Barone, V.; Mennucci, B.; Cossi, M.; Scalmani, G.; Rega, N.; Petersson, G. A.; Nakatsuji, H.; Hada, M.; Ehara, M.; Toyota, K.; Fukuda, R.; Hasegawa, J.; Ishida, M.; Nakajima, T.; Honda, Y.; Kitao, O.; Nakai, H.; Klene, M.; Li, X.; Knox, J. E.; Hratchian, H. P.; Cross, J. B.; Adamo, C.; Jaramillo, J.; Gomperts, R.; Stratmann, R. E.; Yazyev, O.; Austin, A. J.; Cammi, R.; Pomelli, C.; Ochterski, J. W.; Ayala, P. Y.; Morokuma, K.; Voth, G. A.; Salvador, P.; Dannenberg, J. J.; Zakrzewski, V. G.; Dapprich, S.; Daniels, A. D.; Strain, M. C.; Farkas, O.; Malick, D. K.; Rabuck, A. D.; Raghavachari, K.; Foresman, J. B.; Ortiz, J. V.; Cui, Q.; Baboul, A. G.; Clifford, S.; Cioslowski, J.; Stefanov, B. B.; Liu, G.; Liashenko, A.; Piskorz, P.; Komaromi, I.; Martin, R. L.; Fox, D. J.; Keith, T.; Al-Laham, M. A.; Peng, C. Y.; Nanayakkara, A.;

Challacombe, M.; Gill, P. M. W.; Johnson, B.; Chen, W.; Wong, M. W.; Gonzalez, C.; Pople, J. A.; Gaussian, Inc.: Pittsburgh, PA, 2003.

(69) Schäfer, A.; Horn, H.; Ahlrichs, R. *J. Chem. Phys.* **1992**, *97*, 2571-2577.

(70) Schäfer, A.; Huber, C.; Ahlrichs, R. *J. Chem. Phys.* **1994**, *100*, 5829-5835.

(71) Murov, S. L. *Handbook of Photochemistry*; 299-305 ed.; M. Dekker: New York, 1973 pp. 299-305.

(72) Mascharak, P. K.; Rose, M. J.; Patra, A. K.; Alcid, E. A.; Olmstead, M. M. *Inorg. Chem.* **2007**, *46*, 2328-2338.

(73) Montalti, M.; Murov, S. L. *Handbook of Photochemistry*; 3rd ed.; CRC/Taylor & Francis: Boca Raton, 2006.

(74) Mann, K. R.; Freedman, D. A.; Janzen, D. E. *Inorg. Chem.* **2001**, *40*, 6009-6016.

(75) Datta, D.; Drew, M. G. B.; Nag, S. *Dalton T.* **2008**, 2298-2302.

(76) Ramaraj, R.; Kira, A.; Kaneko, M. *Journal of the Chemical Society-Faraday Transactions I* **1987**, *83*, 1539-1551.

(77) Bryant, G. M.; Fergusso.Je; Powell, H. K. J. *Aust. J. Chem.* **1971**, *24*, 257-273.

(78) Wallace, W. M.; Hoggard, P. E. *Inorg. Chem.* **1979**, *18*, 2934-2935.

(79) Krause, R. A.; Krause, K. *Inorg. Chem.* **1982**, *21*, 1714-1720.

(80) Poon, C. K.; Che, C. M. *J. Chem. Soc., Dalton Trans.* **1981**, 1019-1023.

(81) Poon, C. K.; Che, C. M. *J. Chem. Soc., Dalton Trans.* **1981**, 495-500.

(82) Homborg, H.; Sievertsen, S.; Weidemann, M.; Huckstadt, H. *Journal of Porphyrins and Phthalocyanines* **1997**, *1*, 379-384.

(83) Bottomley, F.; Mukaida, M. *J. Chem. Soc., Dalton Trans.* **1982**, 1933-1937.

(84) Weidemann, M.; Sievertsen, S.; Homborg, H. *Z. Anorg. Allg. Chem.* **1998**, *624*, 909-918.

(85) Kostin, G.; Borodin, A.; Emelyanov, V.; Naumov, D.; Virovets, A.; Rohmer, M. M.; Varnek, A. *J. Mol. Struct.* **2007**, *837*, 63-71.

(86) Kojima, T. *Chem. Lett.* **1996**, 121-122.

(87) Byabartta, P.; Jasimuddin, S.; Ghosh, B. K.; Sinha, C.; Slawin, A. M. Z.; Woollins, J. D. *New J. Chem.* **2002**, *26*, 1415-1424.

(88) Durig, J. R.; Mcallist.Wa; Willis, J. N.; Mercer, E. E. *Spectrochim. Acta* **1966**, *22*, 1091-1100.

(89) Tfouni, E.; Lang, D. R.; Davis, J. A.; Lopes, L. G. F.; Ferro, A. A.; Vasconcellos, L. C. G.; Franco, D. W.; Wieraszko, A.; Clarke, M. J. *Inorg. Chem.* **2000**, *39*, 2294-2300.

(90) Doyle, M. P.; Hoekstra, J. W. *J. Inorg. Biochem.* **1981**, *14*, 351-358.

(91) Bertelsen, G.; Skibsted, L. H. *Meat Science* **1987**, *19*, 243-251.

(92) Cox, D. D.; Benkovic, S. J.; Bloom, L. M.; Bradley, F. C.; Nelson, M. J.; Que, L.; Wallick, D. E. *J. Am. Chem. Soc.* **1988**, *110*, 2026-2032.

(93) Kirin, S. I.; Yennawar, H. P.; Williams, M. E. *Eur. J. Inorg. Chem.* **2007**, 3686-3694.

(94) Lubben, M.; Meetsma, A.; Wilkinson, E. C.; Feringa, B.; Que, L. *Angew. Chem. Int.Ed. Engl.* **1995**, *34*, 1512-1514.

(95) Renz, M.; Hemmert, C.; Meunier, B. *Eur. J. Org. Chem.* **1998**, 1271-1273.

(96) Yamaguchi, M.; Ichii, Y.; Kosaka, S.; Masui, D.; Yamagishi, T. *Chem. Lett.* **2002**, 434-435.

Chapter 5

Conclusion

5.1 Conclusion

The importance of NO and metal-nitrosyl complexes within biology has been the focus of many research projects within the last few decades. In particular, copper nitrite reductase (Chapter 2) and the photolabilization of M-NO complexes (Chapter 3 and 4) have been areas of research that have been studied by a number of research groups, and in particular, in this thesis.

First, the geometry and binding mode of Cu(I)-NO was analyzed computationally. It was found that the geometry of the Cu(I)-NO subunit in the CuNIR protein and model complexes has a much larger flexibility in terms of the coordination mode of NO and the Cu-N-O angle than previously anticipated from model complex studies. The side-on structure found in the protein seems to be largely due to steric interactions with Ile-257. This destabilizes the end-on structure relative to the side-on structure. The static structure used in the calculation with a "frozen" Ile-257 does not take into account the dynamics of Ile motion. Taking the effective space demand of Ile-257 into account, likely causes the observed side-on geometry in the crystal structure. Correspondingly, a small change in conformation in solution that slightly reorients Ile-257 would then allow the NO to bind end-on as observed in solution for CuNIR and the known model complexes.[1-3] This is due to the fact that intrinsically, the end-on structure is always energetically favored.

Secondly, spectroscopic and computational data were used to analyze the electronic differences between $Ttz^{t\text{-}Bu,Me}$ and the analogous $Tp^{t\text{-}Bu,Me}$ ligand when bound to copper(II). It was found that based on the EPR and computational results, Ttz^{-} is a slightly stronger σ-donor than Tp^{-} when bound to copper(II). Experimentally, $Ttz^{t\text{-}Bu,Me}$Cu(II) complexes show nitrogen superhyperfine coupling while $Tp^{t\text{-}Bu,Me}$Cu(II) has no spectral resolution of any superhyperfine splittings. DFT calculated nitrogen hyperfine

coupling constants support the idea that the coordinating nitrogen atoms are responsible for the observed superhyperfine splitting in the experimental EPR spectra. However, the calculations also predict overall similar nitrogen superhyperfine coupling constants in the analogous Ttz^- and Tp^- complexes, which disagrees with the experimental findings. This indicates that the differences between Ttz^- and Tp^- might be more subtle than one would expect based on the EPR results.

In addition to analyzing the electronic differences between Ttz^- and Tp^-, spectroscopic and computational data were used to analyze the change in geometry observed for the Ttz^- complexes in solid and solution. It was concluded that the solution structures are most likely square-pyramidal. Unfortunately, the computational EPR parameters using a square-pyramidal geometry do not accurately reflect the experimental EPR parameters and a better model is needed in order to further analyze the spectra computationally.

Next, the vibrational spectroscopic properties and electronic structures of two Mn(II)-NO complexes were analyzed to explain the photolability of NO upon excitation in the Vis-NIR region. Both complexes were found to have a Mn(I)-NO^+ type electronic structure, where the NO^+ ligand then forms two very strong π–backbonds with the formally Mn(I) center. The photolability of the NO upon excitation in the UV region was shown to be due to direct excitation of d_π_π* → π*_d_π CT states (transition within the Mn-NO π bond) that leads to population of Mn-NO antibonding orbitals (*direct mechanism*). In contrast, the unusual photolability of the Mn-nitrosyl complexes upon irradiation in the Vis-NIR region was explained by the presence of low-lying d_{xy} → π*_d_π singlet and triplet excited states. These excited states can be populated by initial excitation into d_{xy} → L(Py/Q_π*) CT transitions between Mn and the coligand, followed by intersystem crossing into the corresponding triplet states. These can then relax into the d_{xy} → π*_d_π triplet excited states, which are strongly Mn-NO antibonding in nature, and therefore, promote dissociation of the NO ligand (*indirect mechanism*). In comparison, in the analogous Ru(III) complexes with NO, the d_{xy} → π*_d_π excited states are located at higher energy, which prevents photoactivation of the NO ligand upon Vis-NIR excitation in these complexes. *The Mn-nitrosyl complexes therefore show the long sought-after potential for easy tunability of the NO photorelease properties by simple changes in the*

coligand, due to NO photodissociation *via* the indirect mechanism, which is strongly coligand dependent.

Finally, the photolability of a number or ruthenium-nitrosyl complexes was analyzed in both aqueous and organic solvents. We found that water-soluble complexes $[Ru(TPA)(Urea)(NO)]^{3+}$, $[Ru(H_2edta)(NO)]$ and $[Ru(Hedta)(NO)]$ were slightly photolabile in aqueous soltions. In addition, organic solvents such as DMF and CH_3CN were used to analyze the photolability of analogous water-insoluble ruthenium nitrosyls. The ruthenium-nitrosyl complexes photolabilized in organic solvents had higher quantum yields than the complexes in aqueous solutions. In conclusion, photolabilization of ruthenium-nitrosyl complexes in aqueous solutions seems to lower the quantum yields compared to organic solvents, which is unfavorable for the application of these complexes in PDT. Photolabilizing ruthenium-nitrosyl complexes using a myoglobin assay for detection of the released NO allows for the accurate detection of the quantum yields.

In conclusion, this thesis discusses three different aspects of metal-nitrosyl chemistry and contributes to the understanding of the geometric and electronic structures in addition to the photolability of copper-, manganese-, and ruthenium-nitrosyl complexes.

5.2 References

(1) Fujisawa, K.; Tateda, A.; Miyashita, Y.; Okamoto, K.; Paulat, F.; Praneeth, V. K. K.; Merkle, A.; Lehnert, N. *J. Am. Chem. Soc.* **2008**, *130*, 1205-1213.

(2) Periyasamy, G.; Sundararajan, M.; Hillier, I. H.; Burton, N. A.; McDouall, J. J. W. *Phys. Chem. Chem. Phys.* **2007**, *9*, 2498-2506.

(3) Sundararajan, M.; Surendran, R.; Hillier, I. H. *Chem. Phys. Lett.* **2006**, *418*, 96-99.